Live cell lithography and non-invasive mapping of neural networks

By

Anna Linnenberger

B.S., University of Denver, 2001

M.S., University of Colorado, 2010

A thesis submitted to the
Faculty of the Graduate School of the
University of Colorado in partial fulfillment
of the requirements for the degree of

Doctor of Philosophy

Department of Electrical Engineering

2014

This thesis entitled:
Live cell lithography and non-invasive mapping of neural networks
written by Anna Linnenberger
has been approved for the Department of Engineering

____

Dr. Robert McLeod

____

Dr. Juliet Gopinath

Date________________________________

The final copy of this thesis has been examined by the signators, and we find that both the content and the form meet acceptable presentation standards of scholarly work in the above mentioned discipline.

Linnenberger, Anna (Ph. D. Electrical Engineering)
Live cell lithography and non-invasive mapping of neural networks
Thesis directed by Associate Professor Robert McLeod

ABSTRACT

This research explores two applications that both require the ability to dynamically and efficiently redirect a laser to a volume of focal points in a sample. In the first application, a fabrication technique is presented to microlithographically-patterned three dimensional cellular structures in polymer hydrogels, with a particular focus on patterning C2C12 cells in linear arrangements to study the formation of muscle fibers. By exploiting the precision and control of microlithography to fabricate artificial tissues, this research aims to develop and demonstrate use of a tool that can be used to answer fundamental questions of developmental cell biology which cannot be addressed with existing randomly arranged 3D tissue scaffolds or 2D plated cells. In the second application a spatial light modulator (SLM) based microscope is presented that offers a new optical method of stimulating and monitoring interconnected cells in 3D environments. By non-invasively stimulating and imaging such 3D arrangements including artificial, *ex vivo* or *in vivo* tissue volumes, this research further aims to extend understanding of cellular interconnectivity, particularly in neural networks of brain slices. This highly interdisciplinary work was completed in collaboration with a diverse group of active international collaborators from the fields of micromanipulation, microlithography, cellular biology, and neuroscience.

The tissue engineering work presented in this thesis merges holographic optical tweezers for cell positioning with step-and-repeat 3D additive manufacturing to fabricate complex polymer microstructures of arbitrary scale containing internal cellular arrangements organized with micron-scale precision. These polymer micro-scaffolds support the cellular network and also provide channels for nutrient flow and directed cell growth. This research is the foundation of a new discipline of *live cell lithography*, which is used to enable biologists to study cell to cell signaling and cellular growth as a function of 3D cellular positioning in an environment that more realistically represents living tissue.

The second portion of the research extends the understanding of 3D cell networks using optogenetics. The project aims to develop a spatial light modulator (SLM) based microscope to enable optical monitoring and manipulation of the activity of neuronal ensembles, in vitro and *in vivo*. The outcome is a compact commercially available microscope that enables fast, 3D imaging and photoactivation of neurons. This can be used for imaging intact neural network activity, optical manipulation of neuronal firing, functional mapping of brain connectivity, investigating neurovascular coupling, and assaying neuronal activity in animal models of brain disease.

ACKNOWLEDGEMENTS

I’d like to thank several people for their help leading up to this thesis. First, I’d like to thank Prof. Bryant at the University of Colorado, and Prof. Yuste, Dr. Peterka, and Dr. Quirin at Columbia University. Dr. Bryant was critical as a collaborator on my tissue engineering project. Prof. Yuste and his team provided invaluable insight and guidance in designing and demonstrating use of the Pocketscope for Calcium imaging. I thank Prof. McLeod for his continuous encouragement and patients as an advisor. Last I would like to thank my family for their endless support.

Research reported in this publication was supported by the National Institute Of Mental Health of the National Institutes of Health under Award Number R41MH100895. The content is solely the responsibility of the authors and does not necessarily represent the official views of the National Institutes of Health

Table Of Contents

1 Introduction 1

1.1 Introduction to Tissue Engineering 1

1.2 Introduction to optogenetics 8

1.3 Thesis Overview 13

2 The Fabrication Platform for Tissue Engineering 15

2.1 Holographic optical tweezers 15

2.2 Optics for maskless projection lithography 20

2.3 Microscope platform for stereolithography 24

2.4 Conclusions 27

3 Live cell lithography in poly(ethylene glycol) dimethacrylate hydrogel scaffolds 28

3.1 Materials and methods 28

3.2 Lithographic capability of the instrument using PEGDMA monomer 32

3.3 Live-cell 3D lithography via HOT + micro-stereolithography in PEGDMA monomer 36

3.4 Conclusions 40

4 Live cell lithography in thiol-ene hydrogel scaffolds 43

4.1 Materials and methods 44

4.2 Lithographic capability of the instrument using thiol-ene monomer 45

4.3 Live-cell 3D lithography via HOT and micro-stereolithography in thiol-ene monomer 47

4.4 Conclusions 51

5 Patterning cells in a multi-material system 56

5.1 Materials and methods 56

5.2 Live-cell 3D lithography via HOT and micro-stereolithography in a multi-material thiol-ene monomer 57

5.3 Conclusions 63

6 The Pocketscope 65

6.1 The Pocketscope Optics 69

6.2 Automated Cell Body Detection 73

6.3 Arbitrary spatio-temporal targeting 78

7 Maximizing beamsteering efficiency of computer generated holograms 80

7.1 SLM Calibration 82

7.2 Conclusions 92
8 Using the Pocketscope For Calcium Imaging 94
8.1 Materials and Methods 94
8.2 Imaging Neurons in Brain Slices 95
8.3 Fluorescence signals 96
8.4 Conclusions 98
9 Future Work 100
9.1 Hydrogel coatings for medical implants 100
9.2 Living Neural Networks 105
References Cited 109

Table of Figures

Fig. 1 Brightfield micrograph of C2C12 cells seeded into a flask and incubated in differentiation media for 8 days. The cells replicate until the flask is confluent, at which point cell fusion begins. However, in a randomly seeded flask there is no control over the organization and distribution of the fused cells. 4
Fig. 2 An approach to tissue engineering demonstrated by Zorlutuna *et al.*[11]. A) Schematic representation of the SLA. B) Fabrication steps for *xyz* patterning. C) CAD model for fabricating a hydrogel with different cell/material types in the same layer. D) Stereomicroscopy image of the constructed hydrogel. A window frame was fabricated using PEGDA3400, and squares were filled with OMA-PEGMA1100. E) Fluorescence microscopy image of the encapsulated MCs (red), HNs (green), and ASCs (blue), localized at different compartments in the same layer. F) CAD model for fabricating a hydrogel with two different cell types (MCs and HNs) in the same layer, followed by a third cell type (ASCs) encapsulated in the subsequent layer. G) Fluorescence microscopy image of the ASCs (blue) in the first layer, encapsulated in PEGDA3400; H) Fluorescence microscopy image of the MCs (red) and HNs (green) in the second layer, encapsulated in OMA-PEGMA1100 (the scale bar is 1 mm). 6
Fig. 3 (top) Optical layout of the Cube, a brightfield microscope and holographic optical tweezer system 18
Fig. 4 Optical layout of the Cube modified to include the 405 nm maskless projection lithography system. Sample image contains 256 optically trapped 2 um silica beads in water. 21
Fig. 5 Diagram of traditional bottom-up and top-down stereolithography setups. (left) The bottom-up setup shown is an example of a system whereby the laser scans the surface for the curing of the photosensitive material. (right) In the example of the top-down setup, dynamic light projection technology is used to cure a complete 2D layer at once [45]. 24
Fig. 6 Side view of the micro stereolithography chamber used for additive lithography to fabricate thick 3D polymer scaffolds. The bottom of the system is a coated coverslip that prevents polymer adhesion. The top is a microscope slide with a long pass filter to prevent polymerization as a result of illumination for imaging, and a glass spacer is placed under the slide such that the first layer is near zero thickness. The spacer is coated to promote polymer adhesion. Manual actuators are used to lift the microscope slide for multi-layer patterning. The system is mounted in XY translation stages enabling step and repeat patterning. 25
Fig. 7 (a) micro-stereolithography. (b) Microscope slide with the glass spacer and a multi-layer structure. 25
Fig. 8 Brightfield image of a sample fabricated after four sequential "step and repeat" patterning steps. In each exposure, the 2 μm beads are first trapped at 1064 nm, then the surrounding liquid is locally gelled using 405 nm light controlled by the SLM. The material patterning resolution is demonstrated by the bead spacing while the stability of the traps during gelation is demonstrated by the regular grid. ... 33
Fig. 9 (a, left) DIC image of a multi-layer grid of 2 μm silica beads, where each layer contained 64 beads organized into a 6x6 bead matrix. (a, right) Rendering of the multi-layer structure showing scale of the arrangement. (b) Large scale pattern of 2 μm silica beads organized into 3x3 bead grids which was fabricated through 10 time sequential cures 35
Fig. 10 Out-diffusion of oligomers generated when patterning PEGDMA monomer make it challenging to pattern polymer voxels of a consistent diameter. (left) 2 μm silica beads are sequentially encapsulated in

polymer voxels of 30 wt% PEGDMA monomer. After a bead is encapsulated, a new bead is trapped and translated until it is sitting adjacent to the edge of the previously fabricated polymer voxel. Thus, the position of the beads marks the approximate radius of the previously cured polymer voxel. Polymer voxels from cures 1 through 5 are all approximately 4-6 μm in diameter. However, cure 6 resulted in a significantly larger polymer voxel, as can be seen by the position of bead 7. (right) curing conditions and resulting voxel radius. A pre-cure over an area of 345 μm x 345 μm, with a power of 70 mW/cm^2 for a duration of 2 seconds was used. Each patterned cure illuminated a region 6 μm x 6 μm. 36
Fig. 11 40X brightfield micrograph (single field, a&b; stiched fields, c) of live C2C12 cells encapsulated in photopolymerized PEGDMA hydrogel. (a) Six C2C12 cells arranged in a line and encapsulated in layer 1 (b) Three cells are arranged in a line that is placed below the first layer. The slight displacement of the second layer enables an out of focus view of the layer behind. (c) Step and repeat grid fabricated through a series of 9 cures. The images are mosaics of multiple images because the entire structure is larger than the field of view of the Cube. 37
Fig. 12 Scanning fluorescence confocal micrograph of patterned C2C12 cells entrapped in 10 wt% PEGDMA polymer scaffold. Using a LIVE/DEAD assay green fluorescence indicates intact cell membranes, and red indicates a compromised cell membrane. 39
Fig. 13 Live/Dead Assay of cells optically trapped and encapsulated within 10 wt.% PEGDMA modified with RGD. Assay was completed 48 hours after encapsulation, and resulted in minimal viability. (left) red fluorescence indicates a compromised cell membrane (right) green fluorescence of remaining intact cell membrane.. 40
Fig. 14 Step growth of Thiol-ene. A stoichemetric ratio of 0.8 thiols to enes is used to reduce the crosslink density. 43
Fig. 15 (top) Brightfield microphotographs of a series of 7 exposures that resulted in 10 μm voxels each of which was separated by 200 microns. The time between exposures is several seconds to allow time to translate the sample. Structures are patterned with no pre-cure, illustrating greater spatial control and reduced oligomer out-diffusion. (bottom) features are plotted with false color to enhance variations. . 46
Fig. 16 Taking the full width half maximum of a vertical slice through the polymer voxels it is seen that the diameter of the polymer voxels varies by 16% from the first cure to the last. 46
Fig. 17 Image mosaic of a polymer line fabricated through a series of 10 exposures, scale bar is 50 μm. Each exposer polymerized a region approximately 70 μm x 20 um. The inability to visualize the structures during the fabrication process due to the weak index difference between liquid monomer and solidified hydrogel made it challenging to maintaining a perfect registration between cures. 47
Fig. 18 Live/Dead Assay of C2C12 cells photo-encapsulated in thiol-ene hydrogel after 4 day of incubation (left) Cells are patterned in a vertical line, 4 cells long, in thiol-ene without RGD. (right) Cells are patterned in a vertical line, 3 cells long, in thiol-ene with RGD. 48
Fig. 19 (left) Brightfield image of a line of 4 cells that were patterned to form a line, and encapsulated in a degradable thiol-ene hydrogel with RGD. Cells were incubated in growth media with 10% horse serum. After 4 days cells began to fuse as indicated by the joining of the cytoskeletons. (right) Sample is fixed and stained with Phalloidin and DAPI. The joined cytoskeletons are shown in the green fluorescence. .. 49
Fig. 20 Cells are patterned, and incubated in differentiation media for 10 days. Cytoskeletons are stained with Phalloidin, and nuclei with DAPI. The cells show further progress toward forming multi-nucleated

cells. Development is sufficient to allow the nuclei to move within the cytoskeleton. The two cells shown at left and right above each show 8 nuclei. 50

Fig. 21 Confocal images of a range of cells fusing after being arranged into a range of shapes including: letters, parallel lines, rings, and lines of varying lengths. Cytoskeletons are stained with Phalloidin, and nuclei are stained with DAPI. 50

Fig. 22 Cells that grow around the perimeter of the hydrogel voxels readily form actin filaments are shown in the Phalloiden stain as vertical lines along the length of the cell. 51

Fig. 23 Intensity profile of one photon polymerization vs. two photon polymerization. When polymerizing with a femtosecond laser and a two photon initiator, axial confinement is significantly enhanced as the intensity of the polymerizing source falls by the fourth power of the distance from the focal point []. 53

Fig. 24 Biomimetic hydrogel platform formed from a thiol-ene click reaction by photopolymerization. (left) Schematic of biomimetic hydrogel formed from macromers of PEG tetranorbornene, MMP-sensitive peptide dithiol, which serves as the crosslinker, and RGD mono-thiol, which provides cell adhesion sites. (right) Confirmation of degradation for a MMP degradable hydrogel formed with the crosslinker, CVPLSLYSGC, which can be degraded by several MMP's including MMP 1,2,3,7 and 9 []. Degradation is confirmed by placing the hydrogel in a solution containing a high concentration of collagenase (100 U/mL collagenase type I), which led to accelerated degradation. When the crosslinker was PEG-dithiol, no degradation was observed. Data presented as mean with standard deviation as error bars (n=6). 54

Fig. 25 3D view of patterned 8 Arm PEG Norborene rectangles on coverslip. The distance from the edge of one rectangle to the edge of the next is 200 um. Each rectangle is close to 100 um long. If the hydrogel feature is over-exposed by repeatedly curing the same area, then the dimensions are larger. 58

Fig. 26 Polymer voxel submersed in PBS that is fabricated by exposing an area 128 µm x 42 µm to TWO 1 second 405 nm exposures with a power of 56 mW/cm^2 (left) brightfield image taken in the Cube (right) Using contrast enhancement with ImageJ to make the polymer feature easier to visualize.......... 58

Fig. 27 Polymer voxel submersed in PBS that is fabricated by exposing an area 128 µm x 42 µm to THREE 1 second 405 nm exposures with a power of 56 mW/cm^2 (left) brightfield image taken in the Cube (right) Using contrast enhancement with ImageJ to make the polymer feature easier to visualize.......... 59

Fig. 28 (left) Top view of cells (shown as black circles) arranged around the polymer voxels patterned in step 1 (marked with dark blue). The cells are held in place in a hydrogel with a very low crosslink density (marked as light blue circles.) (right) patterned two hydrogel sample with two cells arranged along the border of the hydrogel voxel with the higher crosslink density. 60

Fig. 29 (a) Brightfield image cells patterned along the perimeter of two hydrogel voxels with a high crosslink density that are encased in a secondary hydrogel with a low crosslink density. (b) Brightfield image of the sample after 2 days incubation in differentiation media (c) Confocal image, 40x water immersion. The cytoskeleton was stained with rhodamine phalloidin, and DAPI stained the nuclei. The first 4 cells on the left high crosslink density voxel joined the very long cell that grew along the perimeter of the hydrogel with the low crosslink density. However, the cells on the right high cross linking density voxel collapsed into an undefined ball during the 2 day incubation period. 61

Fig. 30 Brightfield image of cells arranged around a hydrogel voxel with a high crosslink density, and encased in a significantly larger hydrogel voxel with a low crosslink density. An unmarked image is shown at left, and at right key features are noted 62
Fig. 31 Brightfield image of 15 cells patterned around a polymer voxel with a high crosslink density, and encased in a secondary polymer voxel with a low crosslink density (left) just after patterning (right) after 2 days incubation. 62
Fig. 32 (left) brightfield image of arranged cells after incubation (right) confocal scan of arranged cells with Rhodamine Phalloidin staining the cytoskeleton, and DAPI staining the nuclei. 63
Fig. 33 Cells consistently grow along the perimeter of the hydrogel with the low crosslink density, shown as a series rings in the confocal image above. 63
Fig. 34 Optical layout of the Pocketscope (top) and mechanical layout (bottom). 71
Fig. 35 Cubic phase mask used to extend the depth of field of a fluorescent imaging system [91] (left) the point spread function of a conventional microscope as compared to that of an extended depth of field microscope (right) cubic phase mask. 73
Fig. 36 Pocketscope SW automated cell body detection method (a) A brightfield image of neurons in a brain slice that have been loaded for calcium imaging (b) The image of the brain slice after threshold conditions have been applied (c) Locations of local peaks that are greater than the surrounding 5x5 pixels. (d) An overlay of the image with the threshold applied, and identified cell body locations noted in red. 75
Fig. 37 Cell body detection with Image J (a) brightfield image of a brain slice loaded with calcium indicators. (b) applying threshold conditions (c) edge detection (d) overlay of detected edges with Image J, and detected cell bodies using the algorithm developed for the Pocketscope (e) 7 of 109 cell bodies that the Pocketscope software failed to note the presence of. 76
Fig. 38 The bead locations are auto-detected, and indicated with white circles. The currently selected bead from the “Soma Locations” listbox is shown in red. 77
Fig. 39 Fluorescence as a result of targeting 10 um silica beads. Not all the beads are in focus because the cubic phase mask is not in use in this example. 78
Fig. 40 Image of the Fourier plane taken when an SLM is used to apply a hologram. The hologram is designed to produce three focal points with a weighting function applied such that the intensity of two focal points should be approximately equal, and the third focal point should be 10x brighter. Ideally the 0th order would not be visible, and there would be no ghost orders. (left) the raw camera data (right) false color to highlight the locations of the desired focal points which are noted in red circles, the ghost orders which are noted with green circles, and the 0th order which is noted with a black circle. 81
Fig. 41 (top) Plot of 1st order intensity for 25 spots, shown as the software iterates up to 20 times to compute the hologram. (bottom) Plot of uniformity as a function of number of iterations. Within 10 iterations uniformity is generally 90% or greater. 82
Fig. 42 (a) Typical phase response of an SLM as the voltage applied to the pixels is varied. This with a passive coverglass drive scheme. (b) DC balancing drive scheme for a passive coverglass SLM 84
Fig. 43 (a) Typical phase response of an SLM as the voltage applied to the pixels is varied. This with an active coverglass drive scheme. (b) DC balancing drive scheme for an active coverglass SLM 84
Fig. 44 Pattern written to the SLM during calibration. The SLM is divided into 16 subsections. A checkerboard pattern is written to one section, while the rest of the SLM is held blank. A series of 256

images are loaded to the SLM during calibration of each region. One check is held at a constant value of 255, while the other check value is decremented from 255 to 0. As the series of patterns are loaded to the SLM, the intensity of the 1st order is measured. The process is repeated for each of the 16 regions of the SLM. 85

Fig. 45 Intensity of the Fourier plane when checkerboard patterns of varying phase are written to the SLM. 86

Fig. 46 Measurements of 1st order intensity vs grayscale for 16 regions of the SLM, and for the SLM as a single region. 88

Fig. 47 Scaled measurements of 1st order intensity vs. grayscale for 16 regions of the SLM, and for the SLM as a single region. Measurements are only shown for the first wave of modulation. 89

Fig. 48 Regional variability in phase shift when considering 16 regions of the SLM 90

Fig 49 (a) Ideal hologram to produce 3 focal points. (b) Modified version of the hologram where phase errors were introduced based on measurements of the regional phase response. (c) the difference between the two holograms. 91

Fig 50 (top) Fourier transform of the ideal hologram, the Fourier transform of the hologram with phase error due to assuming an invariant phase response, and the difference between the Fourier Transform of the two images. (bottom) Plot of the intensity of the desired focal points, and the unwanted ghost orders for an ideal hologram, a hologram with phase error, and the difference in intensity between the two. When a uniform phase response is assumed, the resulting phase error results in a decrease in 1st order intensity of 2.72%, 2.76%, and 2.73% at each focal point, and a 16.85x increase in the 0th order intensity. 92

Fig. 51 Brightfield image of a brain slice taken in the Pocketscope. The image is from L5 in mouse primary visual cortex, 20 µm below the top of the 400 µm slice. 95

Fig. 52 Calcium imaging with brain slices in the Pocketscope. (a) A fluorescence image of a single time slice in the 30 second recording taken while targeting 15 cells. Fluorescence activity with respect to time is plotted for 3 cells in the sample. The cells of interest are denoted with red numbers directly to the left of the cell. (b) an overlay of fluorescence with a brightfield image of the targeted cells. (c) a recording of fluorescence activity with respect to time for 3 cells in the sample. Cell 1 was highly active, having 15 bursts of action potentials in the 30 second recording. Cell 2 had one synchronous event with Cell 1. For a reference of the noise level, cell 3 exhibits no activity during the recording window. 97

Fig. 53 Calcium imaging with brain slices in the Pocketscope. (a) A fluorescence image of a single time slice in the 30 second recording taken while targeting 15 cells. Fluorescence activity with respect to time is plotted for 3 cells in the sample. The cells of interest are denoted with red numbers directly to the left of the cell. (b) Recorded fluorescence with respect to time for one cell. The reduced intensity and duration of activity indicates fewer action potentials in the bursts of activity. (c) A recording of fluorescence activity with respect to time for 2 cells in the sample, again capturing synchronous activity between two cells. 98

1 Introduction

1.1 Introduction to Tissue Engineering

Over the last 30 years, a wide range of methods have been developed for fabricating synthetic living tissues whose development is studied to answer fundamental questions of biology and to fabricate regenerative medical implants. Despite extensive research, there is not yet an ideal tool for understanding cellular dynamics, tissue growth and for fabricating functional implants. Initial research focused on 2D cell distributions, where patterning of cells was commonly accomplished though lithographic deposition of extra-cellular proteins that were used to direct cell attachment and growth on planar arrays [1,2,3]. Unfortunately, it was quickly realized that 2D structures do not accurately represent living tissue and thus are not appropriate for many biological studies or restorative medicine. As a result, a variety of methods to construct complex 3D tissue scaffolds came under study.

Approaches to fabricating 3D scaffolds are primarily derived from 3D printing [4]. In general, the technology relies on seeding the scaffold with cells after the scaffold has been fabricated [5]. This significantly eases the manufacturing process. It is not necessary to ensure biocompatibility of all materials used during manufacturing, but instead it is only necessary to ensure that the end product is biocompatible. Further, it is not necessary to maintain conditions for cell viability, such as temperature and humidity, during fabrication. Nor is it necessary to develop strategies to prevent cells waiting to be ‘printed’ from adhering to the vial they are suspended in which would result in a decreasing cell concentration with time.

While seeding with cells after fabrication eases constraints on processing, it results in several key limitations. First, it is difficult to selectively expose regions of the scaffold to specific cell types. The inability to ensure that cells only exist along desired channels makes precise patterning of multiple cell types within a single scaffold challenging. Second, seeding after fabrication can result in a non-uniform distribution of cells. This can limit the repeatability of development studies, and makes precise experiments studying cell-to-cell interaction challenging.

The problems associated with seeding cells after fabrication led to research on direct printing of cells, with the long term goal of printing organs [6]. This has been accomplished using a modified ink-jet printer. Cell suspended in solution are loaded into ink cartridges, and are directly printed onto microscope slides. Cells less that 100 µm in diameter fit through the nozzle, and the droplet size that is released from the nozzle can be controlled such that on average one cell is printed per drop. However, in order to increase the likelihood that only one cell is printed per drop, droplet sizes are kept to a minimum. As a result, very little fluid is deposited as cells are printed. The fluid rapidly evaporates after printing, leading to up to 25% loss in viability of samples. In order to combat evaporation, cells are printed on a highly hydrated gel matrix. This is sufficient for printing 2D structures, but does not readily lend itself to 3D structuring. Taking this approach forward, it would be necessary to print a single layer, coat that layer in the hydrated gel matrix to provide a platform for the next layer, and then print a second layer. Removing the sample from the system makes it challenging to retain registration between layers. Furthermore, for fundamental studies of cell to cell communication the inability to provide patterning with cellular resolution is insufficient.

Thus, a critical need in this active research field is the development of a method which can rapidly fabricate arbitrary 3D distributions of multiple cell types in an arbitrary 3D hydrogel structure. This would provide an unprecedented level of control over cellular arrangement to enable fundamental studies of growth, development, and degenerative disease. The goal of this research is to demonstrate how the precision of photolithography and holographic optical tweezers can be merged to arrange cells within a 3D volume and photopolymerize a hydrogel network around those cells. The network functions as a supporting structure for cells and can provide biomechanical and biochemical cues to promote growth in complex multi-material samples.

Organization of C2C12 myoblasts to study formation of multi-nucleated myotubes, which are muscle fibers, is an ideal problem to validate this approach to tissue engineering. If C2C12 myoblasts are seeded in a flask with differentiation media, cells will replicate until confluent and fusion will begin. Fig. 1 shows a brightfield image of C2C12 cells that were incubated for 8 days in differentiation media. Very little open space is present between cells, indicating that the sample is confluent, and multiple long cells have formed indicating cell fusion and myotube formation. However, the random initial organization of the cells leads to disorderly myotube formation. Functional muscle tissue capable of producing significant contractile forces requires alignment of myotubes which does not result from this random initial seeding.

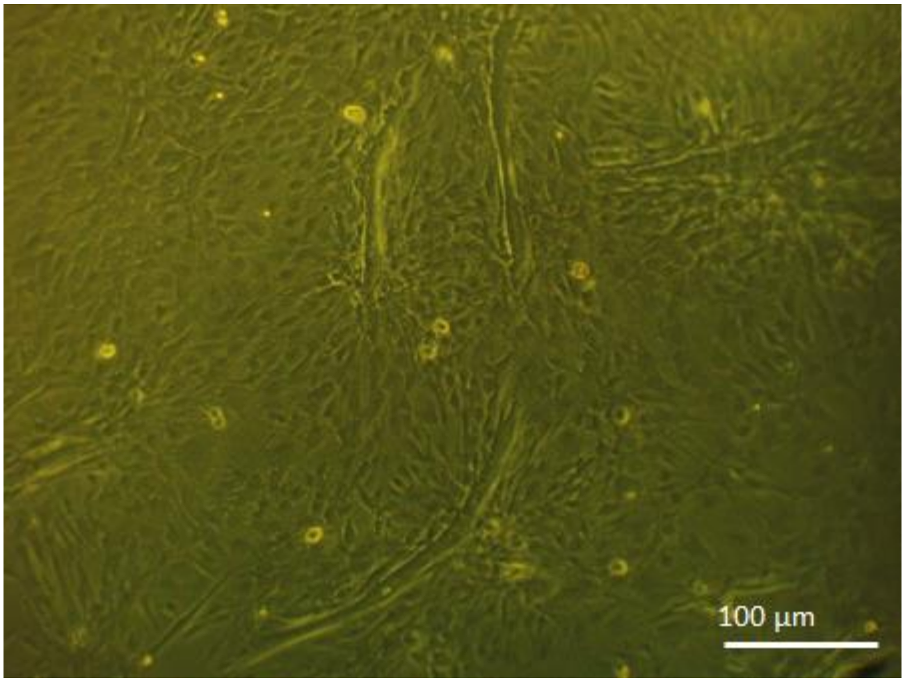

Fig. 1 Brightfield micrograph of C2C12 cells seeded into a flask and incubated in differentiation media for 8 days. The cells replicate until the flask is confluent, at which point cell fusion begins. However, in a randomly seeded flask there is no control over the organization and distribution of the fused cells.

In order to fabricate orderly arrangements of myotubes it is necessary to provide some mechanism which promotes organization of the C2C12 myoblasts prior to fusion. A variety of techniques have been demonstrated to accomplish this goal on planar arrays through use of either biochemical or biomechanical cues. One strategy, demonstrated by Bajaj *et al*. is to print fibronectin on petri dishes. Cells washed onto the petri dish preferentially adhere to the fibronectin, allowing exploration of myotube formation in a range of geometries including lines of different widths, tori of different inner diameters, and hybrid structures (linear and circular features with different arc degrees) [7]. Other approaches considered the importance of biomechanical cues provided by edges to align myoblasts. For example, Hume *et al.* used surface topography to align cells within microchannels [8], resulting in thick orderly formation of myotubes. Likewise Chan *et al.* fabricated multi-material cantilevers composed of poly (ethylene glycol) diacrylate (PEGDA) and acrylic-PEG-collagen (PC) mixtures [9]. Acrylic-PEG-collagen was incorporated into the PEGDA-based materials to enhance cell adhesion, spreading, and organization. Chan demonstrated that cells preferentially aligned to the boundary of the cantilever, and the neighboring cells align correspondingly. Fujita *et al.* found that edges are sufficient to define alignment if the total width of the cantilever is less than 400 µm wide. [10]. In summary, these studies have shown that randomly plated C2C12 myoblasts will preferentially form myotubes aligned to the boundary of the plated region. This organization propagates some distance from the edge such that aligned myotubes can be formed.

While these studies demonstrate the ability to precisely pattern myotubes formation in a plane, the technologies do not readily translate to 3D patterning to build large scale tissue scaffolds. Further, these methods do not allow for fabrication of more complex scaffolds that contain more than one cell type. Finally, alignment from the boundary of a randomly plated region does not enable precise study of myoblast signaling or the fabrication of myotybes with arbitrary geometry.

To address some of these shortcomings, Zorlutuna *et al.* combined stereolithography with encapsulation of cells in hydrogel to fabricate multi-layer tissue scaffolds with multiple cell types as shown in Fig. 2. Zorlutuna fabricated samples with spatially organized blocks of C2C12 cells, PC12 cells, and adipose-derived stem cells in a 3D hydrogel matrix with tunable mechanical and degradation properties [11]. This enabled studies of cellular interactions and of the microenvironments in complex tissues. While this significantly increased the complexity of the fabricated scaffold, the scaffolds consisted of blocks of encapsulated cells that were 3mm wide, with random organization of the cells within the blocks. This is particularly deleterious for the C2C12 cells, as the random organization over such a large area did not lead to formation of orderly muscle tissue.

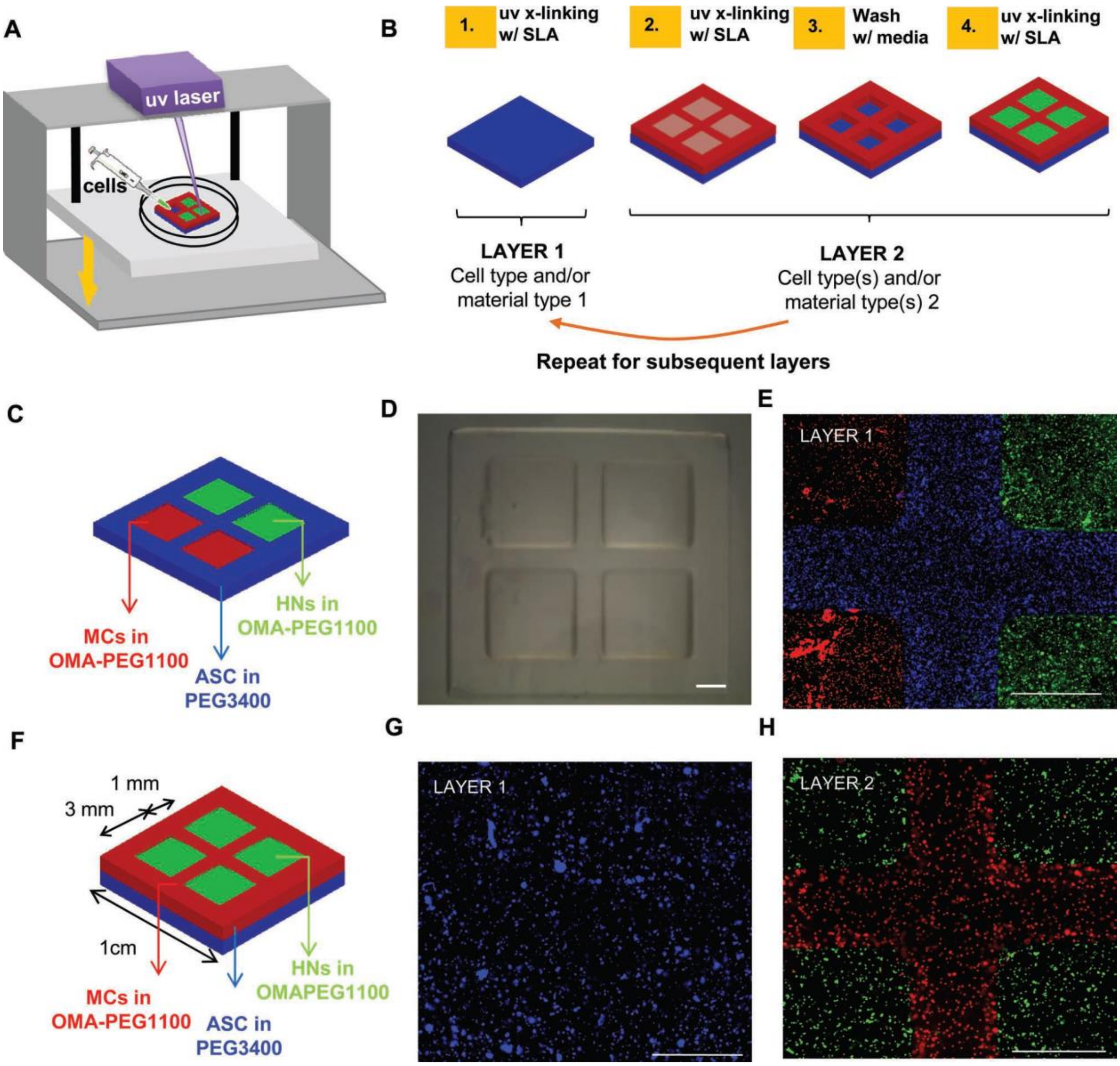
A
uv laser
cells
B
1. uv x-linking w/ SLA
2. uv x-linking w/ SLA
3. Wash w/ media
4. uv x-linking w/ SLA
LAYER 1
Cell type and/or material type 1
LAYER 2
Cell type(s) and/or material type(s) 2
Repeat for subsequent layers
C
MCs in OMA-PEG1100
ASC in PEG3400
HNs in OMA-PEG1100
D
E
LAYER 1
F
1 mm
3 mm
1cm
MCs in OMA-PEG1100
ASC in PEG3400
HNs in OMAPEG1100
G
LAYER 1
H
LAYER 2

Fig. 2 An approach to tissue engineering demonstrated by Zorlutuna *et al.*[11]. A) Schematic representation of the SLA. B) Fabrication steps for *xyz* patterning. C) CAD model for fabricating a hydrogel with different cell/material types in the same layer. D) Stereomicroscopy image of the constructed hydrogel. A window frame was fabricated using PEGDA3400, and squares were filled with OMA-PEGMA1100. E) Fluorescence microscopy image of the encapsulated MCs (red), HNs (green), and ASCs (blue), localized at different compartments in the same layer. F) CAD model for fabricating a hydrogel with two different cell types (MCs and HNs) in the same layer, followed by a third cell type (ASCs) encapsulated in the subsequent layer. G) Fluorescence microscopy image of the ASCs (blue) in the first layer, encapsulated in PEGDA3400; H) Fluorescence microscopy image of the MCs (red) and HNs (green) in the second layer, encapsulated in OMA-PEGMA1100 (the scale bar is 1 mm).

This research presented here demonstrates a method to control the number of nuclei of multi-nucleated C2C12 cells, the direction of growth of the cells, and the organization of multi-cell structures. Living cells are directly patterned and encased into hydrogel voxels using holographic optical tweezers combined with maskless projection lithography. Multilayer structures of arbitrary dimensions are realized through step-and-repeat patterning and micro-stereolithography. This is demonstrated to be a biocompatible process that removes the need to later seed the scaffold with cells [12,13]. Furthermore, this work demonstrate the ability to rinse and replace the liquid monomer during the patterning process such that more complex structures containing multiple materials can be fabricated. The approach allows for controlled studies of fundamental cellular biology and tissue engineering via millimeter scale scaffolds containing arrangements of cells positioned with micron-scale accuracy.

In the first half of this thesis, holographic optical tweezers are utilized to arrange cells into three-dimensional patterns for tissue engineering research. The enabling technology is the nematic liquid crystal spatial light modulator (NLC SLM) that is used to modulate the phase of a coherent light source to selectively generate and rapidly manipulate the 3D position of hundreds of intense optical foci within a 3D volume. Each focus is capable of trapping and manipulating the position of cells via the photon momentum. The second half of this thesis expands this capability to dynamically structure light and translates it into the field of neuroscience. All the concepts of holographic optical tweezers can be applied, but no longer as a tool to manipulate the position of objects within a 3D volume. Instead the focal points are used to probe and manipulate neural circuits in brain slices, as described next.

1.2 Introduction to optogenetics

Despite extensive research of neurological diseases including Alzheimer’s, Parkinson’s, schizophrenia, depression, post-traumatic stress disorder and autism spectrum disorders, understanding of neurological disease and treatment remains poor. There has not been a fundamentally new class of drugs for psychiatric disorders since the 1970s. It is hypothesized that this is largely because we lack the tools required to understand how neural circuits work and how drugs act on them [14]. The lack of medical breakthroughs for treatment of neurological disease represents a significant healthcare cost today and projections that are unsustainable. For example, the Alzheimer’s Association reports that in 2013 Alzheimer's will cost the nation $203 billion. This number is expected to rise to $1.2 trillion by 2050 [15]. Therefore, there is a need for better tools to understand brain function and how brain function is altered when mental illness occurs. Such tools would also allow for quantitative measures of how drugs impact brain function such that more effective and localized treatments for mental illness can be developed.

Understanding of brain function at the cellular level began in 1949 with Cole and Hodgkin [16,17] when they developed the patch clamp to measure the properties of ion channels in the cell membrane of the squid giant axon. In a traditional patch clamp experiment, the cell membrane is manually ruptured by a glass pipette approximately 1 micron in diameter. The current as a result of ions flowing through channels in the cell membrane can be measured with respect to a reference via an electrode in the glass pipette.

Over the last 65 years, the tool has come into widespread use, enabling researchers not only to measure the voltage variations during cellular activity with single cell resolution, but also allowing the ability to stimulate activity in cells. When two patch clamps are used simultaneously, the technique can be used to map neural circuits. A patch clamp is used to stimulate action potentials in one neuron and a second patch clamp is used to probe for a postsynaptic response in surrounding neurons. In this application, the sensitivity of the patch clamp is beneficial. The postsynaptic response to an action potential from a single presynaptic cell is a much smaller than an action potential. Thus, the postsynaptic event induced is not easily detectable using methods other than a patch clamp.

As useful as the patch clamp is, there are critical drawbacks. First, the technique is invasive. When attempting to probe cells deep into the tissue, the probes inevitably tear holes, damages cells, and breaks the connectivity of the networks above the desired target. Second, it is easy to accidentally kill the cell one is attempting to measure when rupturing the cell membrane. Lastly, it is time consuming to patch clamp multiple cells in brain slices, limiting the number of cells one can probe before the slice dies. These drawbacks limit the ability to use a patch clamp to understand the brain from a circuit level.

A far different approach is functional magnetic resonance imaging (fMRI). This technology measures brain activity by detecting changes in blood flow[18]. When an area of the brain is in use, oxygen rich blood flows to the region of activity. Within several seconds, oxygen is depleted. Measurements are made possible because deoxygenated blood is more magnetic than oxygenated blood. Thus, spatial and temporal changes in oxygen levels enable researchers to non-invasively measure the local magnetic resonance of the brain, which is correlated with brain activity. Voxels of measured activity typically range in size from 4-5 mm, to 1 mm. Smaller voxels contain fewer neurons on average, but incorporate less blood flow, and hence have less signal than larger voxels. Thus, a voxel typically contains a few million neurons [18]. This spatial resolution is sufficient for structural imaging for diagnosis of large scale intracranial disease such as tumors, for diagnosis of injury, and for detecting lesions. However, it is less commonly used for in understanding neurological diseases.

It is hypothesized that this is because neurological diseases exists at a different scale, potentially manifesting itself as slight differences within the firing patterns or the structures of the micro-circuitry of the brain [14]. To validate this hypothesis, there is a need for technologies that can address brain imaging at an intermediate resolution between that of two cells observed with a patch clamp and the few million cells in a single voxel of fMRI. Instead it is desirable to look neural circuits with single cell resolution, but retain the ability to simultaneously monitor and manipulate hundreds of cells within a 3D volume.

In the last decade, neuroscientists have begun to transition from patch clamps and fMRI, to a new set of optical techniques to tackle studies of emergent level of neuronal circuit activity, using light to both monitor and manipulate the activity of neuronal ensembles, *in vitro* and *in vivo*. The combination of optical methods with genetically encoded photosensitive proteins (referred to as *optogenetics*) and optochemical (caged) compounds now offers the opportunity to image the activity of many neurons through calcium imaging and optically control them through photostimulation.

In calcium imaging, cells are loaded with chemical indicators that bind with calcium during an action potential. If the cell is targeted with an excitation source during the action potential, then there is a localized fluorescence spike. In photostimulation, tissue is loaded with compounds that cleave when illuminated, stimulating receptors in neighboring cells causing an action potential. These techniques are fast, enabling researchers to monitor and manipulate cellular activity on timescales approaching 1 kHz [19] and can be used on large numbers of cells with a spatial specificity of less than 1 µm [20]. Light is less invasive than electrodes, and offers considerable flexibility and simple multisite modulation. Finally, optical techniques can have single cell resolution, while retaining the ability to target a large number of cells within a volume of the brain.

Development of chemical compounds for optogenetics is driving advancements in commercially available microscopes to address two fundamental limitations. The first is slow temporal resolution. Scanning microscopes use resonant stages, galvanometer scanners, or fast random-access serial scanning using acousto-optic deflectors to raster scan a laser through the sample to build an image pixel by pixel. This can result in scanning rates of 50kHz [21]. However, it is still difficult to achieve simultaneous multisite stimulation with this approach because it is necessary for the laser to dwell at each location to collect enough photons to generate a usable image or to modulate the activity. Attempts to circumvent this by increasing the peak excitation intensity are fundamentally limited, because the high intensity triggers photo-damage of the neurons and photo-bleaching of the fluorophores.

The second limitation is that, in commercially available microscopes, the areas in focus are two-dimensional surfaces, while neural circuits have three-dimensional structure. Depth scanning can be used to build a 3D image, but is very slow as it is typically realized by scanning the objective at rates of around 20 Hz [22]. This is insufficient to monitor neural activity in a volume, which occurs on the timescale of a single millisecond. As a result, one only images a small subset of the neurons, and therefore collects a limited picture of the total activity. For optogenetics research, there is a need for a microscope capable of dynamic and arbitrary formation of multiple foci in 3D, and 3D imaging.

In much the same way that NLC SLMs are used in holographic optical tweezers to generate hundreds of independent foci, and to reconfigure the 3D position of the foci at rates of up to 500 Hz, SLMs can be used in optogenetics to address the slow, serial addressing of scanner-based microscopes. Thus, using SLMs one can deliver light to simultaneously excite multiple 3D sites to first stimulate activity, and then to target cells in a volume to monitor the response of the neural circuit to the stimulation. Using a fast camera the activity of the neural circuit is recorded. This effectively parallelizes the process of monitoring and manipulating activity of neurons among a large population of cells.

The potential for use of NLC SLMs in optogenetics was demonstrated by Yuste *et al* with the development of a prototype SLM based microscope that allows for the simultaneous excitation of multiple neurons in brain slices [23]. In that work, Yuste simultaneously imaged and detected action potentials in dozens of neurons, with frame rates of 66 Hz. However, that SLM microscope still relied on a traditional imaging system only capable of imaging a single 2D plane at a time. The lack of 3D imaging did not take advantage of the ability for SLMs to target neurons in a 3D volume. To push SLM microscopy to its potential, one needs to build an SLM microscope that enables fast, truly 3D capabilities addressing not only 3D targeting but also 3D imaging. In addition, for its widespread use by biologists and clinicians, these microscopes must be easy to use, inexpensive, robust, and, ideally, portable. The second half of this thesis presents the design and demonstration of such a system via calcium imaging of live brain slices.

1.3 Thesis Overview

Although two very different problems are studied in this thesis, there is a common thread between the two projects: use of a NLC SLM to rapidly and dynamically control many focal points within a 3D volume of living cells. In the tissue engineering research, control of the focal points is used to selective position cells in liquid monomer. Using a secondary NLC SLM, the liquid monomer is selectively polymerized to provide a supporting structure that holds the cells in place. In the neuroscience research, control of the focal points is used to selectively monitor and manipulate activity of neural circuits in brain slices. While the two applications are quite different, the underlying requirement of efficient control of focal points within a 3D volume remains the same.

The thesis is broken into two sections, the first half aimed at tissue engineering and the second half at optogenetics. In both projects, I designed, built, characterized, and tested a custom optoelectronic instrument. Chapter 2 discusses the SLM-based holographic optical tweezer and micro-stereolithography system designed for tissue engineering. Chapter 3 demonstrates the use of the microscope for patterning poly(ethylene glycol) dimethacrylate (PEGDMA) based hydrogel scaffolds. Chapter 4 explores fabrication of thiol-ene based hydrogel scaffolds, and Chapter 5 investigates patterning cells in a multi-material system. Chapter 6 introduces optics and software of the Pocketscope, which is the SLM based epi-fluorescence microscope used for optogenetics. Chapter 7 justifies the increased need for improved beamsteering efficiency, and explores two methods to improve efficiency. Chapter 8 presents results of calcium imaging in brain slices. Chapter 9 concludes the thesis, including ideas for future work.

2 The Fabrication Platform for Tissue Engineering

The goal of this research is to design a platform that can fabricate millimeter scale three dimensional hydrogel scaffolds containing living cells positioned with micron-scale accuracy. This will lay the foundation for precise and repeatable studies of cell development and cell-to-cell communication. The purpose of this chapter is to describe the design of the optical system used for live cell lithography. Chapters 3, 4, and 5 will present experimental results of the system.

The fabrication platform merges high-speed automated holographic optical tweezers (HOT) [24] with micro-stereolithography. The commercial HOT instrument uses a 1064 nm laser structured by a NLC SLM to organize cells in a liquid mixture of cell culture medium, monomer, and photoinitiator. A 405 nm source is modulated by a second NLC SLM projected into the focal plane to locally convert the liquid into a gel via excitation of the photoinitiator and crosslink of the monomer. To create 3D structures, a small stereolithography chamber is built into the sample area to enable multi-layer fabrication. This 3D printing apparatus is held on precision *x,y* stages, enabling patterning of large lateral areas via a step-and-repeat processes.

2.1 Holographic optical tweezers

Optical trapping, originally demonstrated by Ashkin in 1986, enables manipulation of micron-sized objects using a tightly focused laser beam [25]. Early research with optical trapping aimed at rapidly manipulating the position of a single focal point within a 2D plane through use of a scanning mirror, or acousto-optic deflector (AOD). The high scanning rate, of up to 50 kHz [21], allows one to use this approach to control the position of many objects. Time-sharing a single focal point between multiple trapped objects is possible as long as the laser is returned to the same location faster than the time it takes the trapped object to diffuse away, typically on the order of tens of milliseconds [26]. However AODs and scanning mirrors do not allow the ability to manipulate objects within a 3D volume. This led to the development of holographic optical tweezing systems where a NLC SLM is used to dynamically modulate the phase of an incident laser to impart linear sums of tips, tilts, and defocus terms. This phase pattern, or hologram, is imaged onto the back aperture of a microscope objective. When Fourier transformed by the objective, a volume of tightly focused points are created in the sample, enabling 3D tweezing.

The forces in an optical trap can be broken into two components: a scattering force, and a gradient force, as illustrated in Eq. 1-4 [27]. In these equations I_0 is the intensity of the incident light, σ is the scattering cross section of the sphere, n_m is the index of refraction of the medium, c is the speed of light in vacuum, m is the ratio of the index of refraction of the particle to the index of the medium (n_p/n_m), a is the radius of the particle, λ is the wavelength of the trapping laser, and α is the polarizability of the sphere. One can think of the scattering forces as the force of photons pushing the object in the direction of light propagation. This is generally the force that dominates. However, if there is a steep intensity gradient as can be found in a focal point created with a high numerical aperture (NA) objective, then as light refracts when passing through the object it can transfer momentum that pulls the object to the waist of the focal point. This makes it is possible to manipulate the position of objects by translating the x,y and z position of focal points.

$$F_{\mathrm{scatt}} = \frac{I_0 \sigma n_m}{c}. \qquad \text{Eq. 1}$$

$$\sigma = \frac{128\pi^5 a^6}{3\lambda^4}\left(\frac{m^2 - 1}{m^2 + 2}\right)^2. \tag{Eq. 2}$$

$$F_{\text{grad}} = \frac{2\pi\alpha}{c n_m^2} \nabla I_0 \tag{Eq. 3}$$

$$\alpha = n_m^2 a^3 \left(\frac{m^2 - 1}{m^2 + 2}\right) \tag{Eq. 4}$$

Objects with a higher refractive index than the surrounding media are pulled by the gradient force to the waist of a focal point. However, objects with a lower index of refraction than the surrounding media are repelled by focal points. This necessitates the use of Laguerre Gaussian beams which are dark at the center of the beam, allowing objects with a lower refractive index to be trapped in the hole in the beam. In either case, by dynamically moving the position of the focal point, one can dynamically translate objects within the sample volume.

Optical tweezers systems are capable of generating up to 200 dynamic and independently controllable traps [28]. Although cell manipulation is the typical application, objects as small as tens of nm have been manipulated and diverse materials controlled, including dielectric spheres, metallic spheres, metallic nanoshells, carbon nanotubes, air bubbles and even water droplets in air [29-35].

The volume over which objects can be manipulated is dependent on the design of the tweezing system. The depth of the tweezing system is limited by aberrations of the high-NA objective to approximately ± 20 μm [36]. The lateral dimensions are set by the relay optics used to image the SLM to the back aperture of the objective, the dimensions of the back aperture and the numerical aperture of the objective and the maximum spatial frequency hologram that the SLM is capable of providing. For example, one can consider the lateral dimensions of the Cube (Boulder Nonlinear Systems), as this is used as the foundation for the live cell lithography system presented in this work.

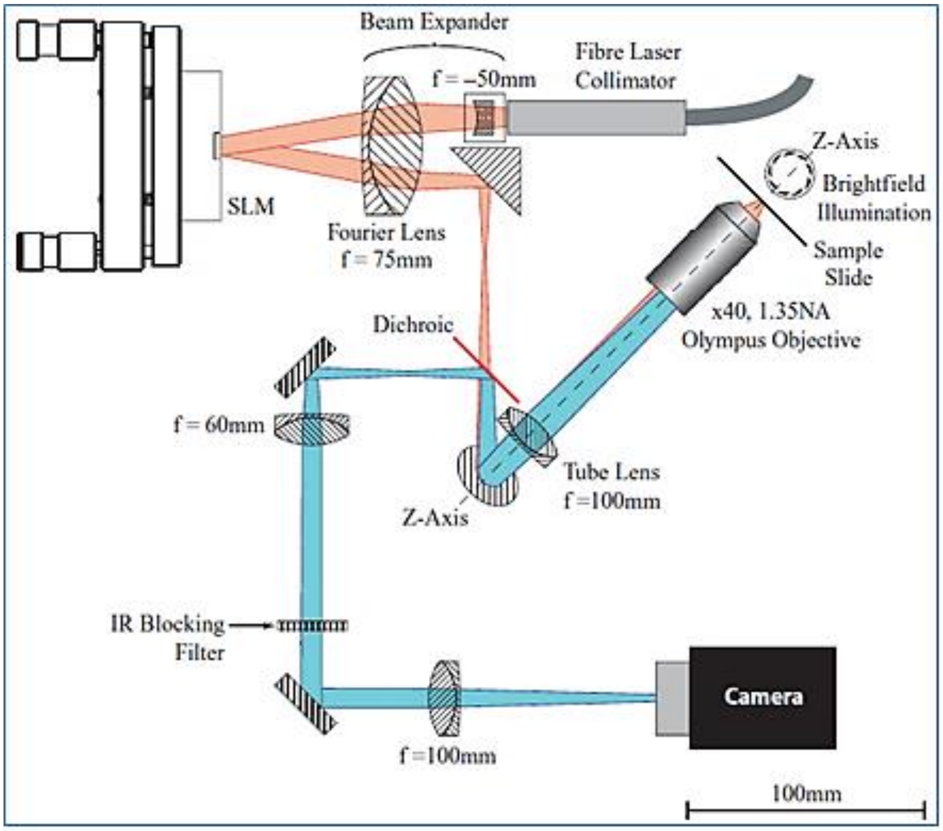

Beam Expander
f = −50mm
Fibre Laser
Collimator
Z-Axis
Brightfield
Illumination
SLM
Fourier Lens
f = 75mm
Sample
Slide
x40, 1.35NA
Olympus Objective
Dichroic
f = 60mm
Tube Lens
f =100mm
Z-Axis
IR Blocking
Filter
Camera
f =100mm
100mm

Fig. 3 (top) Optical layout of the Cube, a brightfield microscope and holographic optical tweezer system

A diagram of the Cube is shown in Fig. 3 [37]. Diffraction limited optical traps are formed using a 10W 1064 nm fiber laser (IPG Photonics, YLR-5-1064-LP) which illuminates a mirrored 512 x 512 pixel phase-only nematic liquid crystal spatial light modulator (P512-1064 SLM, Boulder Nonlinear Systems) through a Keplerian beam expander. The SLM is imaged to the back aperture of the 1.35 NA oil immersion microscope objective (Olympus UAPON 40XO340) through an image relay with a magnification of 1.33x. As a result, the 15 µm pixel pitch of the SLM is magnified to 20 µm at the objective. The maximum angle that the SLM can steer to is realized when a binary 0, π grating with period of 2 pixels is written to the SLM. Using a wavelength of 1.064 µm, the maximum angle the SLM can steer to is 1.52°. The focal length of the objective is 4.5 mm. Thus, in the Cube the maximum lateral dimension of tweezing are ±119.7 µm.

The choice to magnify the image of the SLM in the relay optics between the SLM and the objective increased the disparity between the angle that the SLM can steer to, which is ±119.7 µm, and the area that the objective can image, which is 662 µm. However, the magnification in the relay optics matches the image of the SLM to the dimensions of the back aperture of the objective, meaning that the full NA of the objective is utilized to create traps. Had the SLM be relayed with a demagnification, it would have been possible to extend the angle to which the SLM can steer over, but at the expense of an increase in the waist of the traps, thus reducing the gradient force produced by the focal points, and reducing the trap strength. Thus, a design decision was made to maximize trap strength at the expense of the limiting the field of view over which traps can be manipulated.

The maximum number of pixels available in Boulder Nonlinear Systems SLMs is 512 x 512. Via the Fourier Transform, it is possible to produce 512 x 512 focal points in a 2D plane in the sample if the 0th order is placed in the middle of the field of view. In the Cube, a design decision was made to place the 0th order outside of the field of view, thus limiting the number of positions that a trap can be placed to 256 x 256 positions. The objective used has a field of view of 662 µm, and a diffraction limited focal point has a radius is 0.47 µm. Thus, the objective is capable of generating 1403 x 1403 resolvable spots. The limitations in the number of available pixels, and the pixel pitch of the SLM results in an under-utilization of the objective by a factor of 5.5.

In the imaging arm, the intermediate image of the sample is magnified such that the sample area and the area over which the SLM can efficiently optically trap are more closely matched. Thus, the microscope images 120 µm x 90 µm of the quadrant of the sample immediately below and to the right of the 0th order of the tweezing system.

The phase patterns on the SLM are computed using the Lenses and Gratings algorithm [38,39] programmed in OpenGL and running on a graphics co-processor (nVidia Quadro FX 5600). This has been demonstrated to be capable of simultaneously trapping hundreds of objects, in addition to correcting for aberrations as a result of the SLM and optical train [37].

2.2 Optics for maskless projection lithography

With few exceptions, fabricated patterns and structures built using HOT are impermanent, with the elements of the structure diffusing away from their trapped positions as soon as the trapping light is extinguished. Castellino *et al.* successfully demonstrated the possibilities of permanent nanostructure fabrication using HOT in 2003. In this work, dielectric spheres were manipulated and then subsequently bound using various chemical schemes [40]. Ikin *et al.* successfully demonstrated a related method of binding dielectric spheres in 2008 [41]. Similarly, Agarwal *et al.*[42] demonstrated the ability of HOT to manipulate, cut, and fuse pre-treated carbon nanotubes through ablation. While each of these research efforts resulted in fabrication of permanent structures, the small micro-structures that were built were left free floating in a liquid solution.

To form permanent 3D structures that are fixed within polymer voxels, Mirsaidov *et al.* used multiple laminar fluid flows in a microfluidic network to convey E. coli to an assembly area where optical tweezers were used to organize bacteria into arrays containing 4 to 16 cells. The cells were then encapsulated in a 30 µm x 30 µm x 45 µm volume of photopolymerizable hydrogel. To extend the size of the array, a step-and-repeat method was employed [43]. However, the depth of the structures was limited by objective aberrations to 40 µm [36].

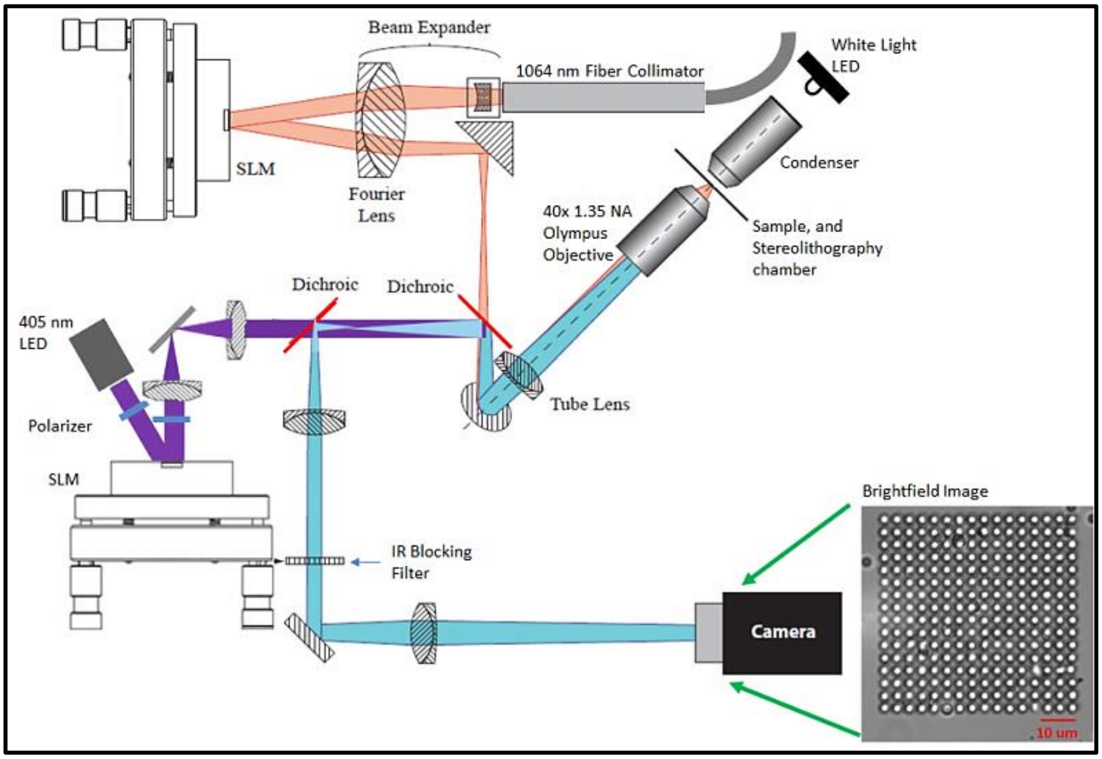
Beam Expander
1064 nm Fiber Collimator
White Light LED
SLM
Fourier Lens
Condenser
40x 1.35 NA Olympus Objective
Sample, and Stereolithography chamber
Dichroic
Dichroic
405 nm LED
Polarizer
Tube Lens
SLM
Brightfield Image
IR Blocking Filter
Camera
10 um

Fig. 4 Optical layout of the Cube modified to include the 405 nm maskless projection lithography system. Sample image contains 256 optically trapped 2 um silica beads in water.

Similarly, this thesis demonstrates fabrication of permanent structures for tissue engineering through photopolymerization. However, in this work the depth of structures is not defined to the aberration limit of the objective because photopolymerization is realized through a combination of maskless projection lithography as described in this section, and micro-stereolithography as described in the following section. A diagram of the Cube with maskless projection lithography is shown in Fig. 4.

The source used for maskless projection lithography is 410 mW, 405 nm LED (Thorlabs M405L2) which provides spatially uniform illumination with low coherence to suppress speckle noise and interference. The LED is polarized and used to illuminate a 512 x 512 pixel liquid crystal SLM (Boulder Nonlinear Systems P512-532) employed as a programmable amplitude mask. In contrast to the SLM used for optical tweezers, the linear polarization incident upon this SLM is oriented at 45 degrees relative to the liquid crystal director, resulting in a pixilated programmable polarization rotation. This polarization rotation is converted to amplitude modulation by an orthogonal analyzing polarizer. Use of crossed polarizers prevents unwanted reflections off of surfaces of the SLM from degrading the quality of the off state, resulting in a contrast ratio of 200:1 or better. A dichroic mirror (NT69-201, Edmund Optics) is used to introduce the 405 nm pattern into the imaging arm of the Cube, such that the SLM plane is in focus at the sample. The SLM is imaged to the sample with demagnification such that the SLM illuminates a region that is 345 µm x 345 µm.

Two methods are implemented in software to selectively expose and polymerize regions of the sample. The first approach uses the locations of the optical traps as center points, and selectively exposes regions that are 10 µm in diameter about the center points to the 405 nm polymerization source. Thus, each trapped object is locally encased in a 10 µm hydrogel voxel. This is a useful strategy for studying cell to cell signaling because each cell is held immobile, but the biochemical cues produced by the cells can diffuse through the hydrogel. A secondary method is implemented that is aimed at studying myotube formation. In this application cell mobility is important in order to allow myoblast fusion. Thus, the center trap in a line of traps is used to define a center point, and a rectangular ring about this center point is selectively polymerized. This provides a hydrogel structure around a line of cells, but leaves an empty region between the cells for myotube formation.

There are two critical points to note about this approach to maskless lithography. First, unlike the 1064 nm trapping pathway, possible aberrations of the 405 nm optical imaging path were not measured or corrected. Diffraction limited patterning would result in features with a radius of 0.18 µm. The cells used in this work have an average diameter of 10 µm. For the current work it is desired to fabricated structures with feature sizes comparable to a cell diameter, which is nearly a factor of 10 larger than the diffraction limit, making the effects of aberrations negligible. Second, use of a chrome mask or a digital micromirror array would result in a higher contrast ratio. However, a chrome mask would not allow for dynamic patterning to fabricate more complex scaffolds, and improved contrast ratio of a DMD was found to not be required. The contrast ratio of the NLC SLM was sufficient for preventing polymerization in regions illuminated by “off” pixels.

One challenge of this system is that the same objective is simultaneously used to: image the sample using white light illumination, create the focal points for optical tweezing at 1064 nm, and image the SLM into the sample for photopolymerization at 405 nm. Operating over a very broad wavelength range has implications on the transmission of the system, and aberrations. According to the Olympus specifications, the objective used is at least 65% transmission from 405 nm to 1064 nm. The objective likely contributes to aberrations in the tweezing system, but this is removed by super-imposing an aberration correction with the desired hologram. As previously discussed aberrations present at 405 are not concerning for fabricating 10 µm polymer features, so they are not measured or corrected.

2.3 Microscope platform for stereolithography

Large 3D scaffolds containing precisely positioned cells can be built from many individual layers through stereolithography. In traditional stereolithography, a thin monomer layer is spread onto a base plate by a blade. Using a fast scanning mirror, a single focal point is re-directed across the sample, locally photopolymerizing structures in a 2D plane. After the layer is finished, the base plate is lowered, and a fresh layer of liquid monomer is spread across the top of the part such that the next layer can be fabricated [44, 45]. An alternative, which removes the open surface and applicator blade, is to hold the thin monomer layer between the previously polymerized layer and an optical window whose inner surface has been coated to prevent adhesion of polymer [46]. In this system a scanning laser based approach can be used as described above, or a DMD can be used to project an image into the sample to selectively polymerize. Diagrams of the two approaches are shown in Fig. 5.

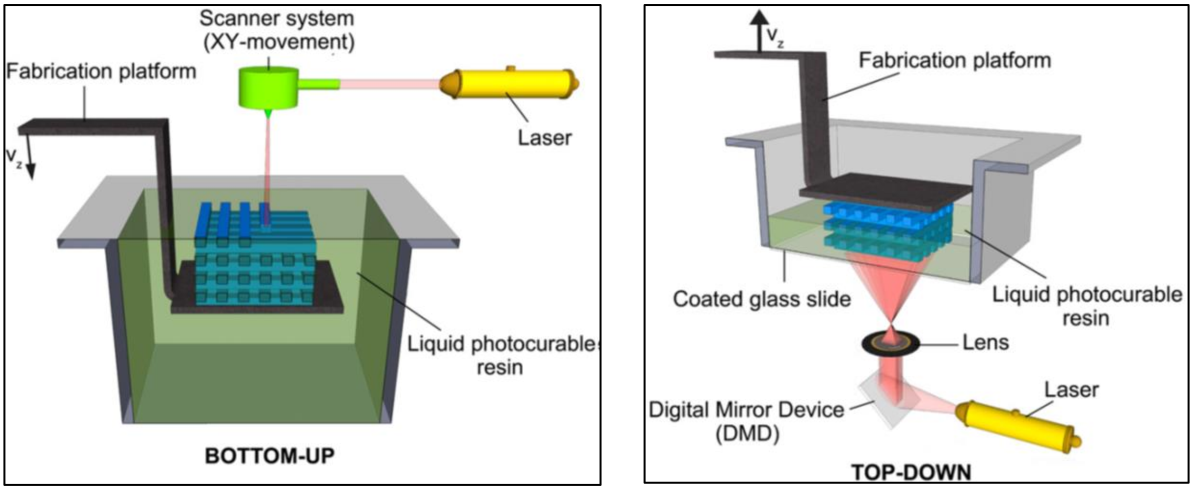
Scanner system
(XY-movement)
Fabrication platform
V_z
Laser
Liquid photocurable resin
BOTTOM-UP
V_z
Fabrication platform
Coated glass slide
Liquid photocurable resin
Lens
Laser
Digital Mirror Device (DMD)
TOP-DOWN

Fig. 5 Diagram of traditional bottom-up and top-down stereolithography setups. (left) The bottom-up setup shown is an example of a system whereby the laser scans the surface for the curing of the photosensitive material. (right) In the example of the top-down setup, dynamic light projection technology is used to cure a complete 2D layer at once [45].

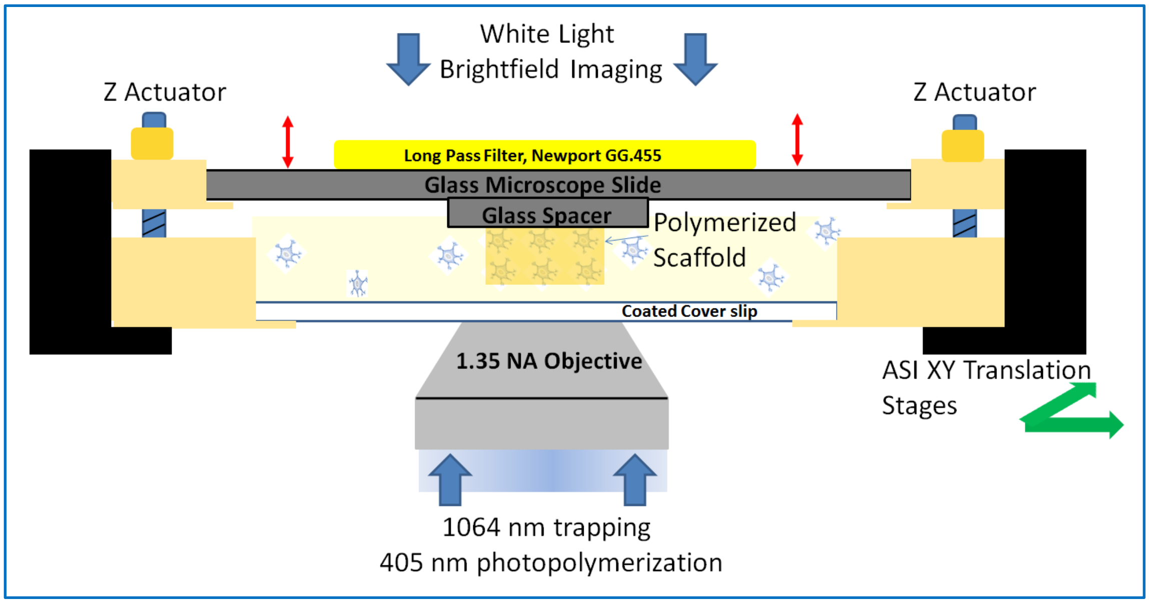
White Light
Brightfield Imaging
Z Actuator
Z Actuator
Long Pass Filter, Newport GG.455
Glass Microscope Slide
Glass Spacer
Polymerized
Scaffold
Coated Cover slip
1.35 NA Objective
ASI XY Translation
Stages
1064 nm trapping
405 nm photopolymerization

Fig. 6 Side view of the micro stereolithography chamber used for additive lithography to fabricate thick 3D polymer scaffolds. The bottom of the system is a coated coverslip that prevents polymer adhesion. The top is a microscope slide with a long pass filter to prevent polymerization as a result of illumination for imaging, and a glass spacer is placed under the slide such that the first layer is near zero thickness. The spacer is coated to promote polymer adhesion. Manual actuators are used to lift the microscope slide for multi-layer patterning. The system is mounted in XY translation stages enabling step and repeat patterning.

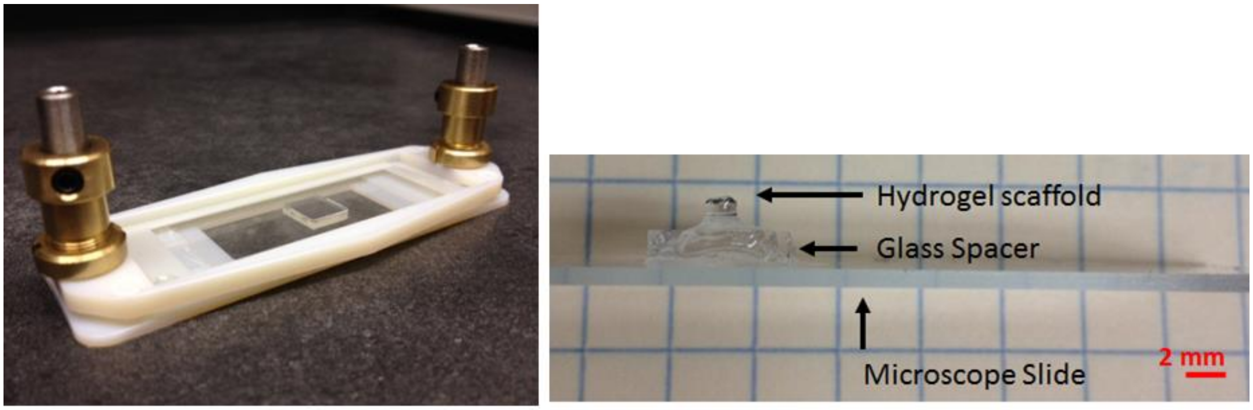
Hydrogel scaffold
Glass Spacer
Microscope Slide
2 mm

Fig. 7 (a) micro-stereolithography. (b) Microscope slide with the glass spacer and a multi-layer structure.

The micro-stereolithography system used in this research is shown in Fig. 6 and Fig. 7(a). The system is similar to the top down approach of Fig. 5, but the entire device is miniaturized sufficiently to fit into a standard microscope slide holder. To my knowledge, this is the smallest micro-stereolithography system ever built, enabling it to fit in most commercially available microscopes.

The base of the chamber is a standard coverslip, which is required for the fabrication chamber to be compatible with the high NA objective used in the tweezing and imaging systems. As shown in Fig. 6, the coverslip is held in a baseplate that is attached to the *x,y* translation stages (MS-2000-XY, ASI) of the Cube. The coverslip is coated with an adhesion preventer, the details of which are presented in Chapter 3, which is used to minimize bonding of monomer to the coverslip during repetitive polymerization of each layer.

The top of the fabrication chamber is formed by a microscope slide, a long pass filter and a glass spacer. The all-glass construction enables brightfield imaging to be illuminated from the top of the chamber. The long pass filter is used to block the shorter wavelengths of the white light source that is used for brightfield imaging (Luxeon, MR-WC100-20S) from polymerizing the sample. The filter is attached to the microscope slide with index matching oil. The glass spacer placed below the microscope slide is used to offset the position of the top of the fabrication chamber such that the first layer is near zero thickness. The spacer is treated with a polymer adhesion promoter, which is detailed in Chapter 3.

To fabricate samples, liquid monomer is injected into the well in the bottom of the chamber. This results in a thin fluid layer initially formed between the top and bottom windows. Cells or beads are suspended in the liquid monomer, and are arranged into a desired pattern using holographic optical tweezers. Once the desired pattern is defined, the liquid monomer is selective polymerized using one of two methods previously described. A step and repeat strategy can be used to extend the lateral dimensions of the scaffold. Additionally, the *z* actuators (here manual screws, although the design is compatible with miniature motorized actuators), can be used to raise both the upper window and the adhered gel layer, and the process is repeated to form a second layer.

The minimum layer thickness of fabricated samples is several microns is determined by the actuator resolution and the cell diameter. The maximum sample thickness of several cm is limited by actuator range and the sample volume of the microscope. A multi-layer sample fabricated through this additive layering procedure is shown in Fig. 7(b). Each layer is approximately 100 µm thick, but by repeatedly polymerizing layers a structure several millimeters thick is fabricated. This system can fabricate parts limited only by mechanical stage limits, in distinct contrast with prior art limited by the objective depth and lateral field of view.

2.4 Conclusions

This chapter presented the design of a l*ive cell lithography* [12] platform that merges holographic optical tweezers with micro-stereolithography to fabricate multilayered 3D structures encapsulating live cells. It provides micron-scale 3D control of both cellular distribution and gel structure to enable new forms of engineered 3D live cell tissue scaffolds. The system is designed to trap hundreds of objects with micron-scale resolution within a volume of 120 µm x 90 µm x 40 µm. The addition of maskless projection lithography enables fabrication of millimeter scale hydrogel scaffolds, containing layers that can range in depth from several microns to 100’s of microns. In the chapters to follow, the capabilities of the system are explored for patterning silica beads and C2C12 cells in Poly(ethylene glycol) dimethacrylate PEGDMA based hydrogel scaffolds, for patterning C2C12 cells in thiol-ene hydrogel scaffolds, and for patterning more complex samples consisting of two material types.

3 Live cell lithography in poly(ethylene glycol) dimethacrylate hydrogel scaffolds

The previous chapter described the design and implementation of an instrument that combines high-speed HOT at 1064 nm, brightfield imaging in the red portion of the visible spectrum and projection micro-stereolithography at 405 nm. I now discus the capability of this instrument to manipulate and encapsulate living cells in one of the most common synthetic hydrogels, Poly(ethylene glycol) dimethacrylate (PEGDMA) [47]. A number of potential challenges must be addressed to prove that the instrument is capable of meeting the goal of 3D structured cellular arrays in 3D structured hydrogel. These can be grouped into two general categories. The first challenge is to test the capabilities of the instrument including fidelity of trapped arrangements of objects, achievable polymer resolution, and capability to layer both into 3D structures. To address the first challenge, scaffolds of arranged 2 µm silica beads encapsulated in multiple depth layers and multiple lateral steps are fabricated. The second challenge is to show cell viability after patterning with holographic optical tweezers and micro-stereolithography. To address the second challenge, C2C12 myoblasts are structured in biologically relevant patterns including a multi-layer hydrogel structures with linear arrangements of viable C2C12 cells. LIVE/DEAD assays are used to measure viability of samples.

3.1 Materials and methods

Poly (ethylene glycol) diacrylate (PEGDMA), which cross-links though a free radical mediated chain growth, is a commonly used platform for encapsulation of cells [47]. It is a semi-permeable hydrogel that can be designed to biodegrade [48], has a widely tunable modulus [49], and is biocompatible. For these reasons, PEGDMA of varying concentrations are utilized to demonstrate the lithographic capabilities of the instrument.

Viscosity is one of the primary material design choices for this application. HOT favors low viscosity that linearly reduces the Stokes drag and proportionally reduces the required laser power to keep cells in the traps at fixed velocity. In Equation 5, F_{drag} is the frictional force, known as Stokes' drag, acting on the interface between the fluid and the particle (in N), μ is the dynamic viscosity (kg /m*s), r is the radius of the spherical object (in m), and v is the particle's velocity (in m/s). Thus, both trap number (in the limit of finite laser power) and allowable trapping time (in the limit of finite dose before loss of cell viability) are inversely proportional to viscosity. Conversely, micro-stereolithography favors high viscosity that, via the Einstein relation, linearly reduces the rate of diffusion of radicals and oligomer from the exposed region into the nearby dark regions. Thus, high viscosity favors small structure size and greater control of polymerization via reduced cross talk between sequential exposures.

$$F_{drag} = 6\pi \mu r v \qquad \text{Eq. 5}$$

To evaluate the effects of viscosity, two PEGDMA monomer solutions are considered. The first monomer solution consists of 49.9 wt. % phosphate buffered saline (PBS, Cellgro), 10 wt % polyethylene glycol dimethacrylate [50] (PEGDMA, Sigma), 0.1 wt. % lithium phenyl-2,4,6-trimethylbenzoylphosphinate (LAP photoinitiator) [51], and 40 wt. % cell solution. The cell solution consists of $0.5x10^6$ C2C12 cells/mL suspended in growth media. The growth media consists of high glucose Dulbecco’s Modified Eagle’s Medium containing 10% fetal bovine serum, 1% Penicillin/Streptomyocin, 0.5 µg/mL fungizone. This monomer is henceforth referred to as the 10 wt % PEGDMA monomer.

The 10 wt% PEGDMA monomer solution has viscosity very similar to that of water, significantly limiting photolithography resolution. Thus, to increase viscosity and reduce out-diffusion of oligomers, a 30 wt. % PEGDMA monomer solution is considered. It consists of 49.9 wt. % PBS, 0.1 wt. % LAP initiator, 30 wt. % PEGDMA, and 20 wt. % cell solution. The increased viscosity of the monomer has an unwanted side effect of causing cells to stay suspended instead of settling to the coverslip. This reduces the number of cells available for tweezing, necessitating an increase in cell density to 2×10^6 C2C12 cells/mL suspended in growth media. This monomer is henceforth referred to as the 30 wt. % PEGDMA monomer.

The next critical material design choice is the photoinitiator. LAP was chosen over initiators commonly used for tissue engineering such as I2959 or eosin [52,53,54] for several reasons. First, its high water solubility (up to 8.5 wt%) enables photosensitivity to be adjusted over a large range. Second, LAP exhibits low yellowing making it possible to deliver the brightfield illumination through a thick layer of polymerized scaffold without significant absorption. Third, the use of an initiator that is sensitive at 405 nm, rather than 365 nm used with the more common initiators, reduces cytotoxicity [51] of repeated exposures and enables the use of a 405 nm LED module that has much higher power than currently available 365 nm modules. This same choice also significantly relaxes the bandwidth requirements on the microscope objective which must maintain efficient transmission up to 1064 nm.

The final requirement on the initiator is that it must be insensitive to the trapping light while maintaining high sensitivity to the polymerizing wavelength. Specifically, the initiator must have almost no single- or multi-photon initiation efficiency in solution when exposed to approximately 1.47 GJ/cm^2 of 1064 nm for time spans of up to 10 minutes. This is in contrast to typical bulk dose to full cure at 405 nm of ~ 100 mW/cm^2 over time spans of seconds. This range of 10^{10} in dose sensitivity is very far beyond typical characterization equipment such as FTIR and is also unlikely to actually be possible even in ultra-pure solutions. However, the presence of rapidly diffusing O_2 that acts as a radical inhibitor will suppress initiation at a sufficiently low rate. As will be demonstrated in the work presented in this chapter, LAP and PEGDMA in solution indicated no gelation of polymer, indicating that the trapping at 1064 and polymerization at 405 nm can operate independently in this material, despite the extremely large range of power in each band.

The final design consideration is that the photolymerized gel must adhere well to the upper glass spacer but not to the lower coverslip. This instrument design consideration is coupled to the materials design through the choice of initiating species and polymerizable group. For example, oxygen inhibits radical initiation and thus an oxygen-rich layer of PDMS has been used in previous research to eliminate adhesion of radical polymerization [55]. In this work, it was found that this suppressed polymerization at the working plane of the 1.35 NA objective. Thus, two coatings are used. A methacrylate coating on the glass spacer is used to promote adhesion of the polymer voxel to the spacer, while a trimethoxy silane coating prevents adhesion of polymer to the coverslip. The coverslip coating is deposited by mixing 0.6 g IPA with 0.017 g acetic acid (A6268, Aldrich) and 0.04 g (heptadecafluoro1.1.2.2-tetra-hydrodecyl) trimethoxy silane (Gelest). The mixture is placed between two coverslips stacked together, and the coverslips are baked on a hot plate at 70 °C for 10 minutes. After baking, coverslips are detached from each other, and rinsed with isopropyl alcohol and distilled water. The microscope slide with the transparent glass spacer is similarly coated; however, 3-(triethoxysilyl)propyl methacrylate (Tokyo Chemical Industry) is used in place of trimethoxy silane such that the coating promotes adhesion of polymer to the glass spacer.

3.2 Lithographic capability of the instrument using PEGDMA monomer

To investigate, and optimize the patterning capabilities of the new instrument, I fabricate structured PEDGMA hydrogels with internal patterns of 2 µm silica beads. There are four main objectives in this section. The first is to demonstrate that photopolymerization does not create instabilities that alter the position of trapped objects. The second is to demonstrate that structures can be patterned with cellular resolution. The third is that step-and-repeat strategies can be utilized to arbitrarily extend the dimensions of structures in a 2D plane. The fourth is to demonstrate complex 3D patterning, and the extent to which registration between layers can be maintained.

Trap stability during photopolymerization is a concern. Optical traps result in forces on the scale of pN. During polymerization, local forces result from: volume shrinkage, diffusional transport of consumed species, and a rapidly increasing viscosity. When the polymerization source is focused into the sample, polymerization forces overwhelm the forces produced by optical traps, thus pulling the objects out of the traps. However, when the polymerizing source is imaged into the sample, the intensity of the polymerization source drops to an incident power 70 mW/cm^2. This enabled patterned structures to be encased in hydrogel without disruption.

Patterning resolution and trap stability during polymerization are illustrated via "step-and-repeat" structuring shown in Fig. 8 using the 10 wt.% PEGDMA monomer. In each of the four sequential exposures, 2 μm silica beads are first positioned within the liquid solution by the 1064 nm tweezing system. After the beads are arranged, they are encased in a polymer voxel.

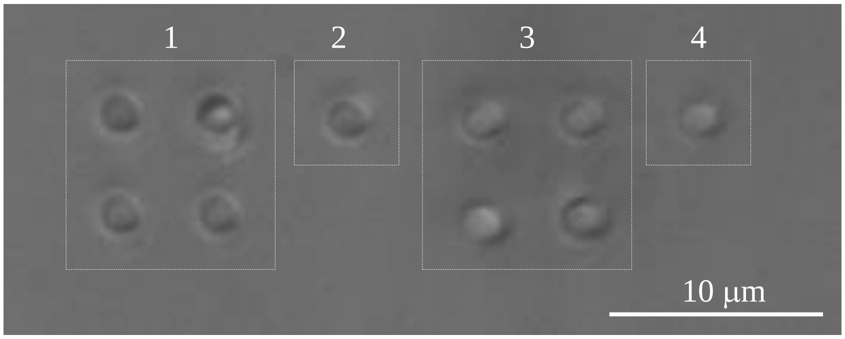

Fig. 8 Brightfield image of a sample fabricated after four sequential "step and repeat" patterning steps. In each exposure, the 2 μm beads are first trapped at 1064 nm, then the surrounding liquid is locally gelled using 405 nm light controlled by the SLM. The material patterning resolution is demonstrated by the bead spacing while the stability of the traps during gelation is demonstrated by the regular grid.

Due to the low viscosity of the 10 wt. % PEGDMA, as the liquid monomer is exposed to the curing source, oligomers form and rapidly diffuse away. In order to pattern structures with cellular resolution, it is necessary to pre-cure the hydrogel to bring the liquid monomer around the beads close to the gel point. This locally increases the viscosity of the monomer. If the pre-cure is immediately followed with a patterned exposure, then it is possible to pattern hydrogel voxels approximately 10 μm in diameter. In the pre-cure, all the 512x512 pixels on the SLM used as a programmable amplitude mask are turned on. This exposes an area of 345 μm x 345 μm around the patterned beads to the 405 nm source for 2 seconds with an intensity of 70 mW/cm^2. The pre-cure is immediately followed with a patterned exposure, illuminating a 6 μm × 6 μm square at the sample to the 405 nm source to locally solidify hydrogel around the trapped beads. This process transforms the pre-cured liquid to a gel without disturbing the trapped objects.

As shown in Fig. 8, automated stages translate the sample and the process is repeated. Although the solid hydrogel cannot be distinguished from the liquid solution in this brightfield image (or even in differential interference contrast microscopy (DIC) due to the weak index change), the localized solidification is demonstrated by the immediate immobility of the trapped beads and the continued mobility of nearby beads used in the subsequent steps.

The localized gelation demonstrated in Fig. 8 has two benefits. First, 1064 nm dose (which is toxic beyond approximately 1 GJ/cm^2 [56]) can be minimized by locally encapsulating cells as soon as they are correctly positioned. Second, the lateral size of the structure is no longer limited to the 345 µm x 345 µm area covered by the SLM but through a step-and-repeat technique can be as large as the motion range of the stages holding the sample, which is 100 mm x 100 mm in the Cube. This enables the ability to pattern the gel within an arbitrarily large single layer, and can be combined with a multi-layer printing technique to create 3D shapes of mm-dimensions.

To illustrate complex 3D structuring with the 10 wt% PEGDMA monomer, multilayer grids of silica beads encapsulated within the hydrogel are fabricated. As shown in Fig. 9(a), each layer consists of 2 µm silica beads arranged into a 6 x 6 bead grid. Spacing between each layer is 95 µm. The lateral registration between the layers is 4 µm, limited by the manual micrometers used. Fig. 9(b) demonstrates the ability to pattern large scale structures in x and y. Grids of 2 µm silica beads are arranged in 3x3 grids, and a supporting polymer voxel approximately 30 µm x 20 µm is used to solidify the arrangement. The sample is translated in x and y, for a total of 10 exposures to fabricate a large scale single sheet.

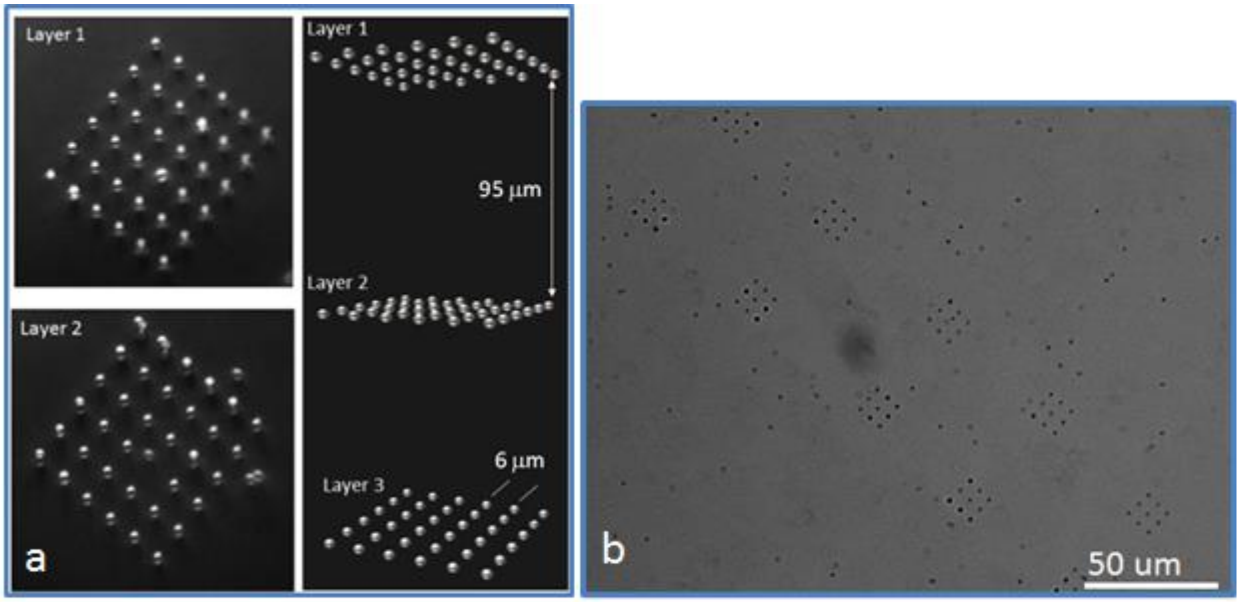

Fig. 9 (a, left) DIC image of a multi-layer grid of 2 µm silica beads, where each layer contained 64 beads organized into a 6x6 bead matrix. (a, right) Rendering of the multi-layer structure showing scale of the arrangement. (b) Large scale pattern of 2 µm silica beads organized into 3x3 bead grids which was fabricated through 10 time sequential cures

The low viscosity of the 10 wt. % PEGDMA necessitated a pre-cure to pattern voxels with cellular resolution. However, this results in a rapid accumulation of oligomers that limit the ability to maintain patterning with consistent structure resolution. To investigate the impact of higher viscosity on patterning resolution, an experiment similar to that of Fig. 8 was performed in which single beads held in traps are used as a micro-rheometer as illustrated in Fig. 10. Following the protocol developed above, a pre-cure of 2 seconds at 70 mW/cm^2 followed by a patterned exposure of varying duration and power resulted in polymer voxels approximately equal in diameter in cures 1 through 5. However, in cure 6 the oligomer concentration in the surrounding monomer was sufficiently high that the radius of the polymer voxel patterned is approximately 4 times greater than that of cures 1 through 5. Higher viscosity reduces the rate of diffusion of oligomer outflow, but still necessitates a pre-cure to pattern structures with cellular resolution. Furthermore, a 30 wt. % PEGDMA monomer is not optimal for maintaining cell viability. Use of a higher concentration of PEGDMA leads to a higher the concentration of radicals, and increases the likelihood that cells will be damaged during encapsulation [57].

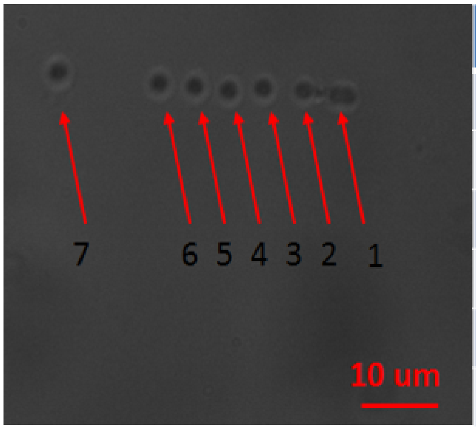

Bead	Cure	Voxel Radius
1	150 ms at 21 mW/cm^2	3 µm
2	50 ms at 3.5 mW/cm^2	3 µm
3	50 ms at 3.5 mW/cm^2	2 µm
4	50 ms at 3.5 mW/cm^2	2 µm
5	50 ms at 3.5 mW/cm^2	2 µm
6	50 ms at 3.5 mW/cm^2	8 µm

Fig. 10 Out-diffusion of oligomers generated when patterning PEGDMA monomer make it challenging to pattern polymer voxels of a consistent diameter. (left) 2 µm silica beads are sequentially encapsulated in polymer voxels of 30 wt% PEGDMA monomer. After a bead is encapsulated, a new bead is trapped and translated until it is sitting adjacent to the edge of the previously fabricated polymer voxel. Thus, the position of the beads marks the approximate radius of the previously cured polymer voxel. Polymer voxels from cures 1 through 5 are all approximately 4-6 µm in diameter. However, cure 6 resulted in a significantly larger polymer voxel, as can be seen by the position of bead 7. (right) curing conditions and resulting voxel radius. A pre-cure over an area of 345 µm x 345 µm, with a power of 70 mW/cm^2 for a duration of 2 seconds was used. Each patterned cure illuminated a region 6 µm x 6 µm.

3.3 Live-cell 3D lithography via HOT + micro-stereolithography in PEGDMA monomer

Patterning beads in PEGDMA is useful to characterize the capabilities of the system relating to hydrogel feature sizes, and to demonstrate the ability to fabricate large scale structures containing sub-structures patterned with micron control. However, the ultimate goal is to pattern hydrogel structures that contain organized sub-structures of live cells. C2C12 cells are an optimal starting point because spatial organization is critical to myotube development. The work described in this section characterizes the capabilities and limitations of patterning cells in PEGDMA.

The cells used here are C2C12 mouse myoblast (ATCC) cultured in growth medium (as above), at 37°C and in 5% CO_2. Upon reaching 70-80% confluency, cells are passaged with

0.25% trypsin, and either re-plated for continued expansion or combined with polymer solution for photoencapsulation. After encapsulation within the hydrogel scaffold, cells are assessed for viability with the LIVE/DEAD® membrane integrity assay, and imaged with a confocal laser scanning microscope (CLSM, Zeiss LSM 510, Thornwood, NY) at 40x magnification.

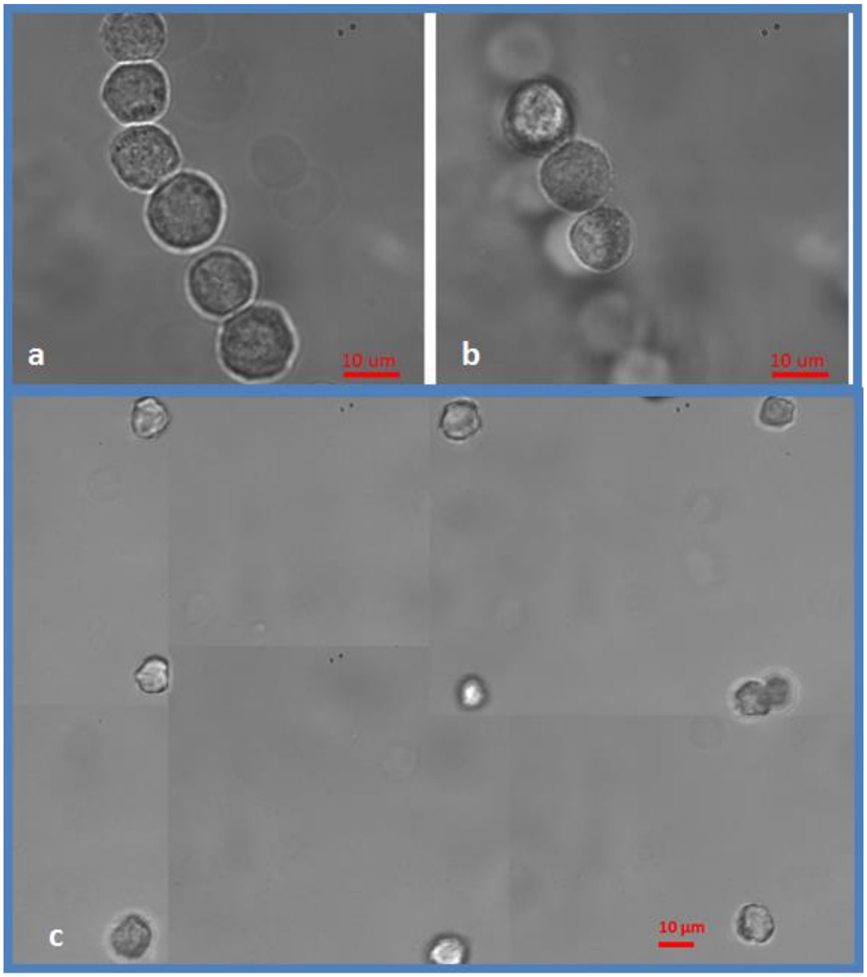

Fig. 11 40X brightfield micrograph (single field, a&b; stiched fields, c) of live C2C12 cells encapsulated in photopolymerized PEGDMA hydrogel. (a) Six C2C12 cells arranged in a line and encapsulated in layer 1 (b) Three cells are arranged in a line that is placed below the first layer. The slight displacement of the second layer enables an out of focus view of the layer behind. (c) Step and repeat grid fabricated through a series of 9 cures. The images are mosaics of multiple images because the entire structure is larger than the field of view of the Cube.

To demonstrate biologically relevant 3D cellular constructs, the system is used to fabricate multi-layer lines of cells that could be used for myotube formation, and grids of cells that could be used to study cell to cell communication. A two layer structure of linearly patterned C2C12 myoblasts is shown in Fig. 11(a) and Fig. 11(b). The first layer consists of a line of 6 cells. Layer 2 consists of a line of 3 cells, slightly shifted to the side such that the first layer can still be seen. Fig. 11 (c) show grids of cells fabricated using a step-and-repeat approach. In each grid, a single cell was trapped and encased in a polymer voxel approximately 100 µm x 90 µm in size. Fig. 11(b) highlights a challenge of the current system. It is not always possible to find cells freely floating near the patterned structure. One solution is to increase the cell concentration, but this can lead to unwanted cells becoming encased the cured polymer, which would negate the purpose of the tool. Another solution was previously demonstrated by Erickson *et al.* by creating a flow of cells through a portion of the sample. When cells are required, the sample is translated, cells are selectively removed from the flow using optical tweezers, and the cells are translated back for use in the fabricated structures [58]. Adding a flow of cells remains a topic of future research.

While availability of cells constrained the complexity of cellular constructs that could be fabricated, the primary goal of investigating cell viability after pattering samples in the live cell lithography system could still be studied. To measure viability, single layers of organized cells were placed in PBS buffer mixed with 1 µL calcein AM and 2 µL ethidium homodimer to perform a LIVE/DEAD® viability assay. Samples containing cells exposed to traps for up to 5 minutes resulting in cell death (indicated by red fluorescence in the LIVE/DEAD viability assay). Consistent with previous work [59], cells optically tweezed for 1 – 2 minutes with less than 200 mW per trap (approximately 1.47 GJ/cm^2) were viable. Fig. 12 shows linear arrangements of cells that were viable immediately after encapsulation.

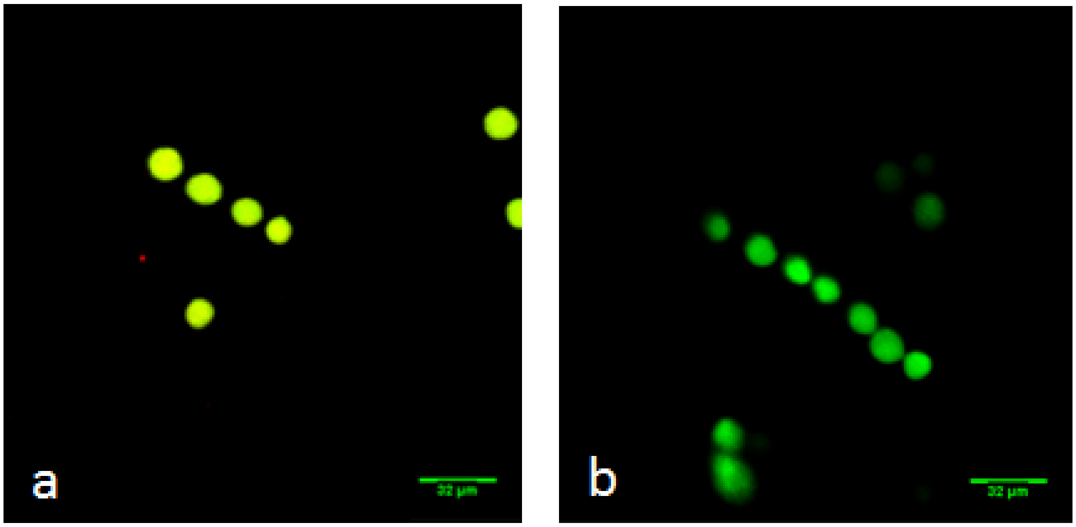

Fig. 12 Scanning fluorescence confocal micrograph of patterned C2C12 cells entrapped in 10 wt% PEGDMA polymer scaffold. Using a LIVE/DEAD assay green fluorescence indicates intact cell membranes, and red indicates a compromised cell membrane.

Showing that cells maintain viability immediately after pattering is important, but in order to complete studies of cellular development and cell-to-cell communication, it is necessary to maintain viable samples for up to several weeks. To determine if living cells held by HOT and encapsulated in photopolymerized PEGDMA hydrogel can maintain long-term viability, multiple samples are fabricated and tested over the span of multiple days. In these samples C2C12 cells are encased within polymer voxels of 10 wt. % PEGDMA.

One concern in maintaining long term viability is enhancing the ability of the cells to adhere to the hydrogel. A commonly used approach is to modify the monomer with a cell adhesion peptide such as arginine–glycine–aspartic acid (RGD). This has not only been shown to promote cellular attachment, but also to promote differentiation [60]. Thus, samples used in long term viability tests include RGD.

After encapsulation, samples are immediately incubated at 37 °C and in 5% CO_2 for multiple days. Growth media is replaced every 2 days. After incubation cells are assessed for viability with the LIVE/DEAD® membrane integrity assay, and imaged with a confocal laser scanning microscope. Fig. 13 shows one of several Live/Dead assays completed with 10 wt. % PEGDMA modified with RGD. Red fluorescence indicates a compromised cell membrane leading to cell death, and green fluorescence indicates a healthy cell membrane. As can be seen in Fig. 13, after 48 hours cells patterned in PEGDMA modified with RGD show minimal viability. This result is representative of all the samples tested. Strategies to overcome this problem are presented in the following two chapters.

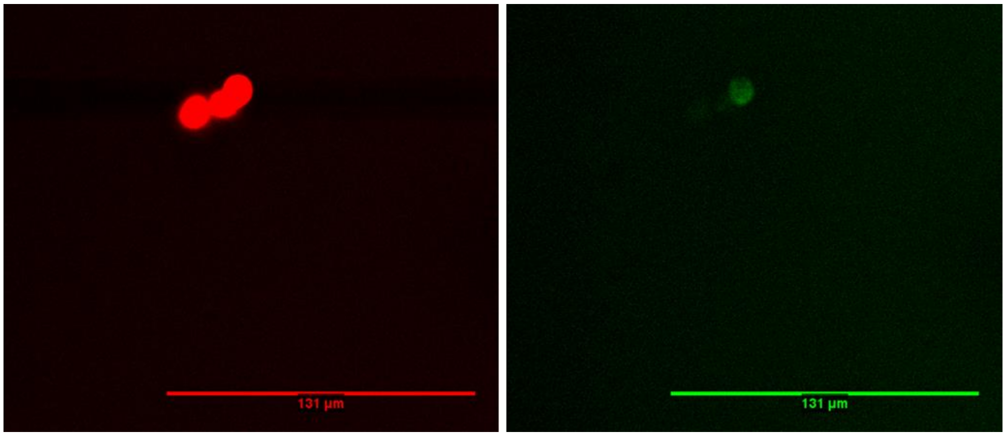

Fig. 13 Live/Dead Assay of cells optically trapped and encapsulated within 10 wt.% PEGDMA modified with RGD. Assay was completed 48 hours after encapsulation, and resulted in minimal viability. (left) red fluorescence indicates a compromised cell membrane (right) green fluorescence of remaining intact cell membrane.

3.4 Conclusions

This chapter demonstrates a new method for fabrication of complex cellular constructs with lithographically-precise cellular arrangements. Use of monomer instead of water increases the viscosity and decreases the index difference between the beads and surrounding media, leading to a decrease of trap strength. However, the tweezing system is shown to be capable of simultaneously manipulating 64 2 μm silica beads in liquid monomer. This work also shows that tweezing of objects at 1064 nm is possible without initiating polymerization of the PEGDMA monomer.

The micro-stereolithography system projects images from a 0.25 Mpixel spatial light modulator illuminated at 405 nm through the adhesion-suppressed coverslip to pattern the gel in 2-3 seconds per exposure. Precision *x,y* automated stages enable large lateral structure size, after which micrometers are used to raise the fabrication platform in *z* for patterning of subsequent layers. The gelation process is shown to preserve the location of trapped objects and patterning of features with 10 µm resolution is demonstrated. Multilayer constructs of both beads and C2C12 cells are shown with positioning accuracy of approximately 1 µm within each layer, and registration between layers to within 4 µm.

The two primary conclusions of this chapter relate to the repeatability in patterning the PEGDMA and the viability of cells in these gels. In order to pattern features with cellular resolution, it is necessary to pre-cure a large region of the sample to bring the liquid monomer close to the gel point. If this is followed with a short patterned exposure, then polymer voxels with diameters close to that of a cell can be fabricated. However, when this process is repeated, the presence of oligomers from earlier exposures influence subsequent exposures. This makes it challenging to consistently fabricate polymer structures. The much more critical limit of PEGDMA gels found was the failure to maintain cell viability over the span of multiple days. As shown in Fig. 1, in a randomly seeded flask multi-nucleated cells began to develop over the span of 8 days. In order to reach the goal of dynamically patterning multi-nucleated cells in hydrogel, the viability of the samples must be improved.

Multiple factors could be responsible for low the viability of the cells. The experiments are not executed in a sterile environment and cells are removed from the incubator for several hours during the patterning process. In an effort to minimize bacterial and mold growth, cells are rinsed in antibiotics each time they are passaged, during patterning process all surfaces are thoroughly and repeatedly cleaned with 70% Ethanol, and the growth media that the samples are incubated in after patterning contains antibiotics. After patterning growth media is replaced every one to two days. While bacteria and mold are not entirely eliminated by this process, samples are not visibly infected. This indicates that cell death is not a result of contamination.

Remaining factors influencing viability relate to the materials used to encapsulate cells. It is well know that radicals produced during polymerization readily react with oxygen, resulting in reactive oxygen species (ROS) [61]. In a PEGDMA based monomer, these reactive oxygen species can no longer contribute to chain-growth of the hydrogel, and multiple studies have found that reactive oxygen species can be associated with cell damage [62,61].

Alternatively, recent research has focused on encapsulation of cells within thiol-ene photopolymerized PEG peptide hydrogels for studies of: 3D cell biology [63,64], the controlled release of therapeutically relevant proteins [65], for directing stem cell differentiation [66], and for promoting tissue regeneration [67]. Unlike PEGDMA, reactive oxygen species produced during polymerization of thiol-ene are consumed by the PEG-dithiol, and further can propagate the step-growth of the hydrogel. It is expected that reducing the concentration of reactive oxygen species surrounding the encapsulated cells by switching to a thiol-ene based hydrogel will improve biocompatibility and viability of the samples. This expectation is validated in Chapter 4.

4 Live cell lithography in thiol-ene hydrogel scaffolds

In order to reduce reactive oxygen species that come into contact with patterned cells and to reduce the influence of oligomer outflow on patterned hydrogel feature sizes, one can consider thiol-ene hydrogels. Thiol-ene polymerization can be propagated by ROS and thus consume ROS which has been shown to improve biocompatible of the hydrogel [61]. Further, when used with LAP as a photoinitiator, thiol-ene is a highly sensitive monomer that can be used to pattern structures with cellular resolution without requiring a pre-cure, as demonstrated in the results presented in this chapter.

Thiol-ene polymerizes through step-growth instead of chain-growth of PEGDMA. The hydrogel forms an orderly matrix-like structure, as shown in Fig. 14, with a tunable modulus that can be controlled by the stoichiometric ratio of thiol-to-ene. A secondary benefit is that thiol-ene can be designed to be degradable at a tunable rate. In this work, use of a degradable hydrogel is important. It allows the cells to be supported, but over time allows the structure to diffuse away allowing cells mobility to fuse. One approach to introduce degradability is to modify the PEG Norborene to support ester links that are degradable in water. Additionally, cell adhesion peptides, such as RGD, can be readily added to the matrix to promote cellular attachment [60].

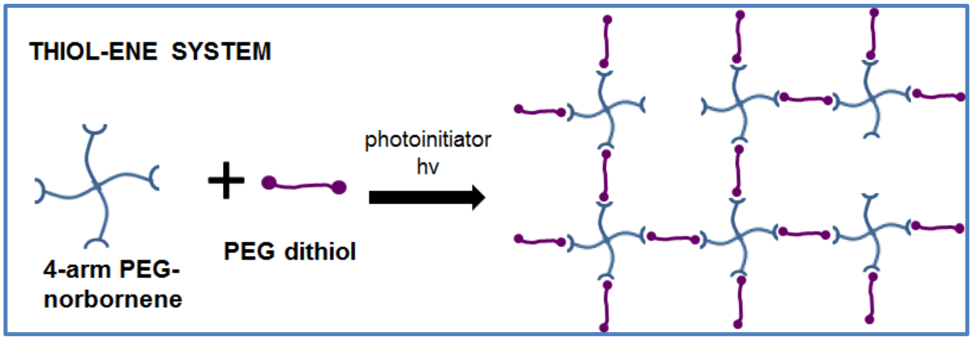

Fig. 14 Step growth of Thiol-ene. A stoichemetric ratio of 0.8 thiols to enes is used to reduce the crosslink density.

4.1 Materials and methods

To evaluate conditions required to polymerize features similar in size to that of a cell, and to understand the influence of oligomer outflow on the diameter of structures fabricated through a series of repeated exposures, initial patterning is done in the absence of cells. The monomer is comprised of 10 wt. % 4-arm PEG-norbornene [68] dissolved in PBS, 0.05 wt. % LAP photoinitiator, and 4 wt. % PEG-dithiol. This results in a stoichiometrically balanced (1 ene to 1 thiol) monomer.

To further test C2C12 viability and development, patterning was performed in both degradable and non-degradable thiol-ene hydrogels. The non-degradable thiol-ene hydrogel consists of C2C12 cells suspended, at a density of $1x10^6$ cells/mL, in a stoichiometrically balanced (1 ene to 1 thiol) monomer solution comprised of 10 wt. % 4-arm PEG-norbornene dissolved in PBS, 0.05 wt. % LAP photoinitiator, 4 wt. % PEG-dithiol, and 0.135 wt. % CRGDS. The degradable thiol-ene hydrogel consists of C2C12 cells suspended, at a density of $1x10^6$ cells/mL, in a monomer solution comprised of 10 wt. % 4-arm PEG-norbornene with an ester link dissolved in PBS, 0.05 wt. % LAP photoinitiator, 3.2 wt. % PEG-dithiol, and 0.135 wt. % CRGDS. The degradable thiol-ene has a stoichiometric ratio of 0.8 to reduce the cross-link density.

Immediately after patterning, samples are incubated for several days to a week. Fused cells are stained with AF-488 Phalloidin to visualize filamentous F-actin in the cytoskeleton, and DAPI is used to stain the nuclei. The staining procedure is as follows:

1. Fix samples in 4% Paraformaldehyde for 30 minutes.

2. Gently wash twice in phosphate buffered saline.
3. Permeablize for 3-5 minutes in 0.1 % Triton X-100 in phosphate buffered saline.
4. Gently wash twice in phosphate buffered saline.
5. Stain with fluorescent phalloidin (AF488-Phalloidin, or Rhodamine Phalloidin) diluted 1:30-1:40 in phosphate buffered saline with 1 % BSA for 35 min at room temperature. Protect from light during staining.
6. Gently wash twice with phosphate buffered saline.
7. Counterstain with DAPI diluted 1:5000 in phosphate buffered saline for 5 minutes. Protect samples from all light.
8. Wash twice with phosphate buffered saline and store in phosphate buffered saline until imaging.

4.2 Lithographic capability of the instrument using thiol-ene monomer

The first goal of this section is to determine the duration and intensity of incident illumination to match polymer features to the region of exposure. Strong agreement between exposure area and resulting features are realized when the liquid monomer is exposed to the curing source for 700 ms, with an incident power of 56 mW/cm^2. The second goal of this section is to establish the impact of oligomer outflow on the consistency of repeatedly pattering the same polymer feature. This is explored by patterning a series of separated polymer voxels, and a continuous line of polymer voxels, and measuring the variations in diameter of the features.

A series of polymer voxels just over 10 µm in diameter are shown in Fig. 15. Each polymer voxel is separated by 200 µm, and the time between exposures is a few seconds, limited by the time required to translate the stages. The area of exposure is marked in Fig. 15 with a red dashed line. As can be seen, exposures 1 and 2 do not fully form the desired polymer structures. However, as measured by the full-width-to-half-maximum size of the polymerized features, the variability in diameter of voxels 1 through 7 is only 16%, as shown in Fig. 16. Comparatively, as shown in Fig. 10, the variability in diameter of voxels in the 30 wt % PEGDMA hydrogel was 400 %. The improved consistency in patterning thiol-ene features indicates that out diffusion of oligomers is still occurring, but at a significantly reduced rate as compared to PEGDMA.

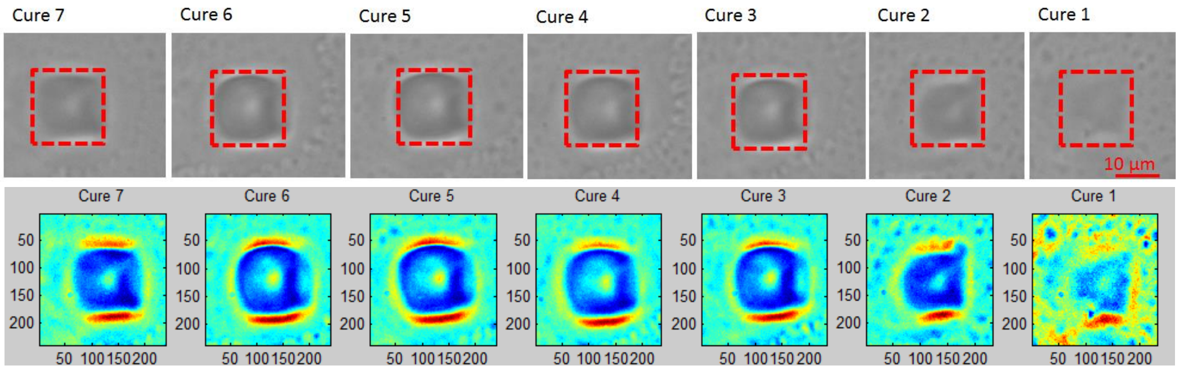

Fig. 15 (top) Brightfield microphotographs of a series of 7 exposures that resulted in 10 µm voxels each of which was separated by 200 microns. The time between exposures is several seconds to allow time to translate the sample. Structures are patterned with no pre-cure, illustrating greater spatial control and reduced oligomer out-diffusion. (bottom) features are plotted with false color to enhance variations.

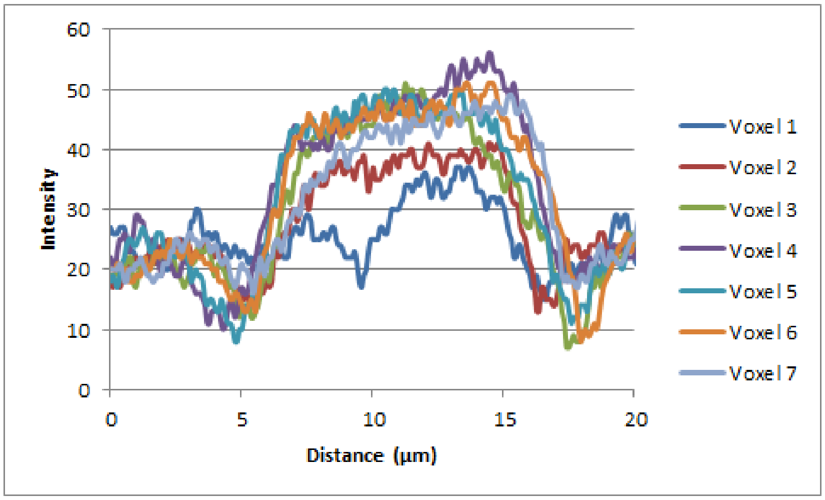

Fig. 16 Taking the full width half maximum of a vertical slice through the polymer voxels it is seen that the diameter of the polymer voxels varies by 16% from the first cure to the last.

To extend the previous results showing only isolated voxels, I next patterned a polymer line through a series of 10 exposures, as shown in Fig. 17. When polymerizing, the index difference between the liquid monomer and polymerized hydrogel is very small. The structure is not possible to visualize until it is rinsed and submersed in a secondary media with a different index of refraction. As a result of the inability to see the polymerized regions during patterning, there are slight discontinuities between each of the 10 segments of the line.

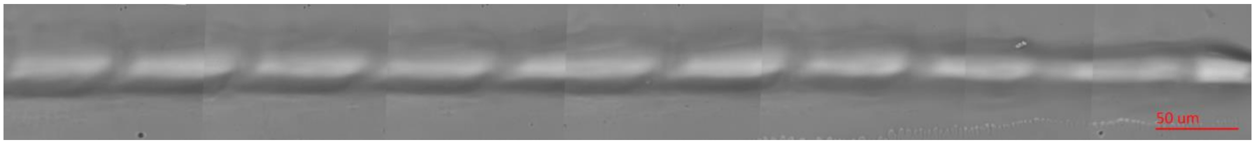

Fig. 17 Image mosaic of a polymer line fabricated through a series of 10 exposures, scale bar is 50 µm. Each exposer polymerized a region approximately 70 µm x 20 um. The inability to visualize the structures during the fabrication process due to the weak index difference between liquid monomer and solidified hydrogel made it challenging to maintaining a perfect registration between cures.

By patterning acellular thiol-ene structures, it is possible to tune the incident power of the curing source and the duration of exposure to match polymer features closely to the exposed area. If the incident power, or duration of exposure are too long, then the sample will be over-exposed, leading to a larger feature than desired. In all future work with cells, curing conditions are retained such that the curing exposures lasts 700 ms with an incident power of 56 mW/cm^2.

4.3 Live-cell 3D lithography via HOT and micro-stereolithography in thiol-ene monomer

Cells patterned in PEGDMA did not maintain long term viability. It is hypothesized that this is due to ROS present in PEGDMA, which motivated use of thiol-ene. Lack of long term viability in PEGDMA did not establish if RGD is beneficial to cell development in this research, necessitating studies of thiol-ene with and without RGD. Several representative live fluorescent images of LIVE/DEAD assays are shown in Fig. 18. Samples are fixed and stained 4 days after encapsulation. When RGD is not used, cells show greater viability than samples patterned with PEGDMA. However, samples patterned in thiol-ene without RGD show weak fluorescence, indicating a compromised cell membrane. Alternatively, when RGD is used as shown in Fig. 18 (right), the cells retain viability, and fluoresce with equal intensity as compared to the surrounding cells that were not exposed to the optical tweezer source, indicating that RGD is beneficial to maintaining viability.

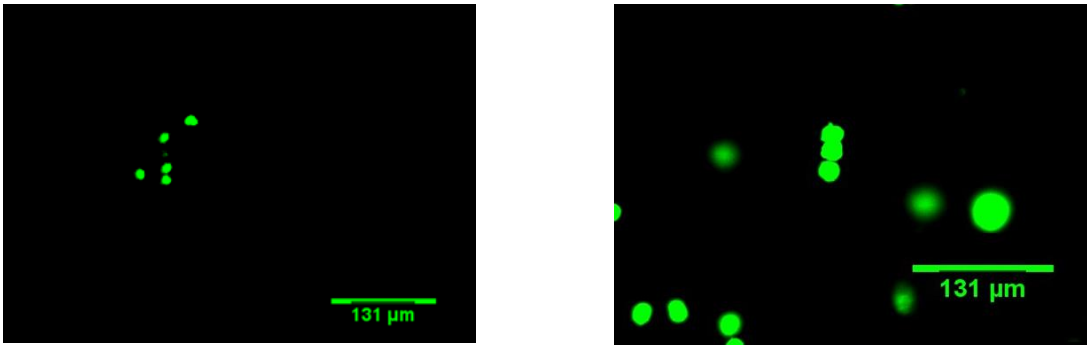

Fig. 18 Live/Dead Assay of C2C12 cells photo-encapsulated in thiol-ene hydrogel after 4 day of incubation (left) Cells are patterned in a vertical line, 4 cells long, in thiol-ene without RGD. (right) Cells are patterned in a vertical line, 3 cells long, in thiol-ene with RGD.

The previous results indicate that thiol-ene with RGD can be used for creating C2C12 constructs that will maintain viability for multiple days. This is a sufficient duration for cells to develop and fuse into multi-nucleated myotubes if incubated in differentiation media. In all results to follow, cells are incubated after patterning in differentiation media that consists of high glucose Dulbecco's Modified Eagle's Medium containing 10% horse serum, 1% Penicillin/Streptomycin, 0.5 µg/mL fungizone.

To evaluate the impact of hydrogel degradability on cell fusion, samples are fabricated in degradable and non-degradable thiol-ene. In all samples, cells are arranged into lines with holographic optical tweezers, and are encapsulated in a hydrogel voxel approximately 100 µm in diameter. Cells encapsulated in the non-degradable hydrogel are found to maintain viability, but never show signs of fusing into multi-nucleated cells. It is hypothesized that because the entire volume around the line of cells is exposed to the polymerization source, and it is likely that a thin hydrogel layer exists between the patterned cells. This layer cannot be broken down by the cells, preventing fusion. Alternatively, cells encapsulated in the degradable hydrogel were found to fuse within 4 days, as shown in Fig. 19. The brightfield image shows the cytoskeletons fusing. This is further indicated by the green fluorescence of the joined cytoskeletons shown in Fig. 19 (right). In this image, the DAPI stain is not limited to the nuclei. This problem is resolved by modifying the staining procedure to decrease the DAPI concentration from 1:1000 to 1:5000, and increasing the staining time from 1 minute to 5 minutes.

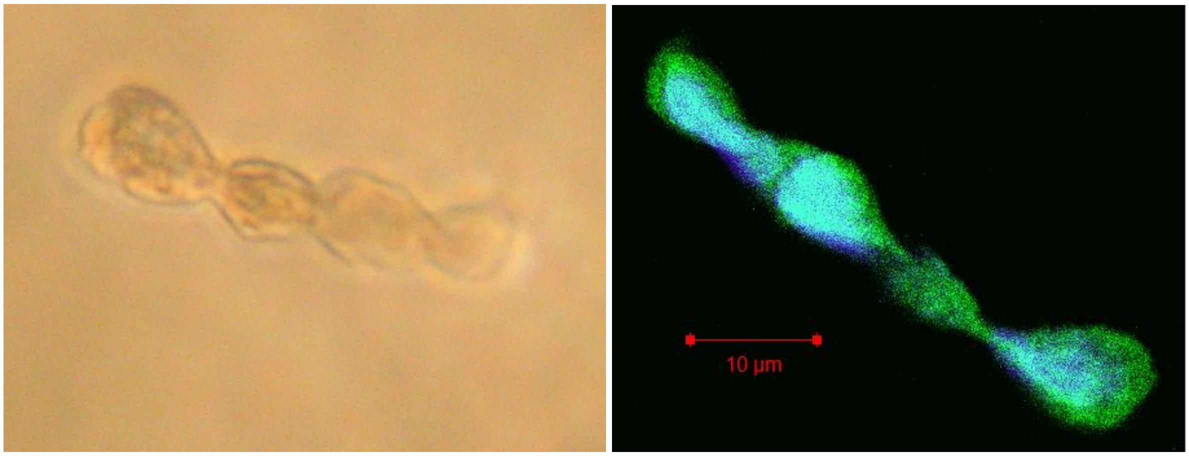

Fig. 19 (left) Brightfield image of a line of 4 cells that were patterned to form a line, and encapsulated in a degradable thiol-ene hydrogel with RGD. Cells were incubated in growth media with 10% horse serum. After 4 days cells began to fuse as indicated by the joining of the cytoskeletons. (right) Sample is fixed and stained with Phalloidin and DAPI. The joined cytoskeletons are shown in the green fluorescence.

Fig. 20 shows two sets of patterned cells, each containing 8 nuclei, which were given 10 days to incubate after patterning. The round morphology seen in Fig. 19 has transitioned into a more tube-like cell, and there is mobility in the nuclei as can be seen by the uneven distribution of nuclei along the length of the cell. To illustrate the flexibility in the pattering, Fig. 21 shows a range of patterns including: letters, parallel lines, rings, and lines of cells containing 2 to 6 nuclei, all of which were patterned in the degradable thiol-ene.

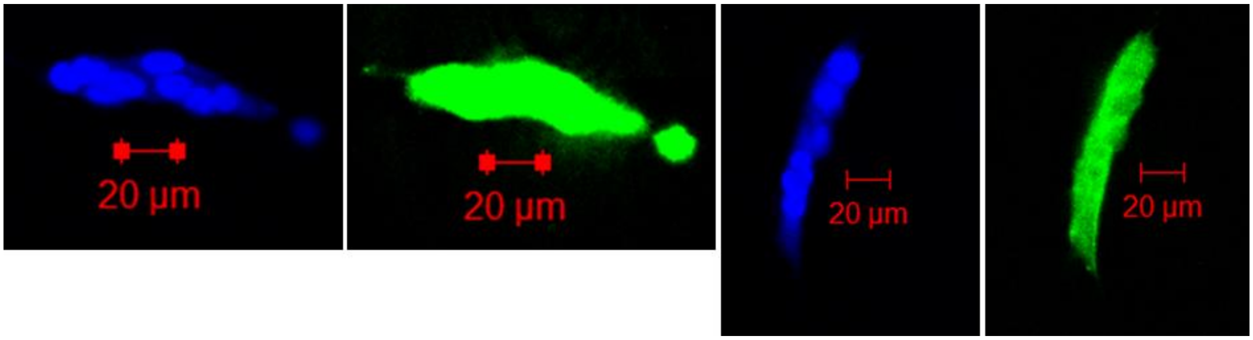

Fig. 20 Cells are patterned, and incubated in differentiation media for 10 days. Cytoskeletons are stained with Phalloidin, and nuclei with DAPI. The cells show further progress toward forming multi-nucleated cells. Development is sufficient to allow the nuclei to move within the cytoskeleton. The two cells shown at left and right above each show 8 nuclei.

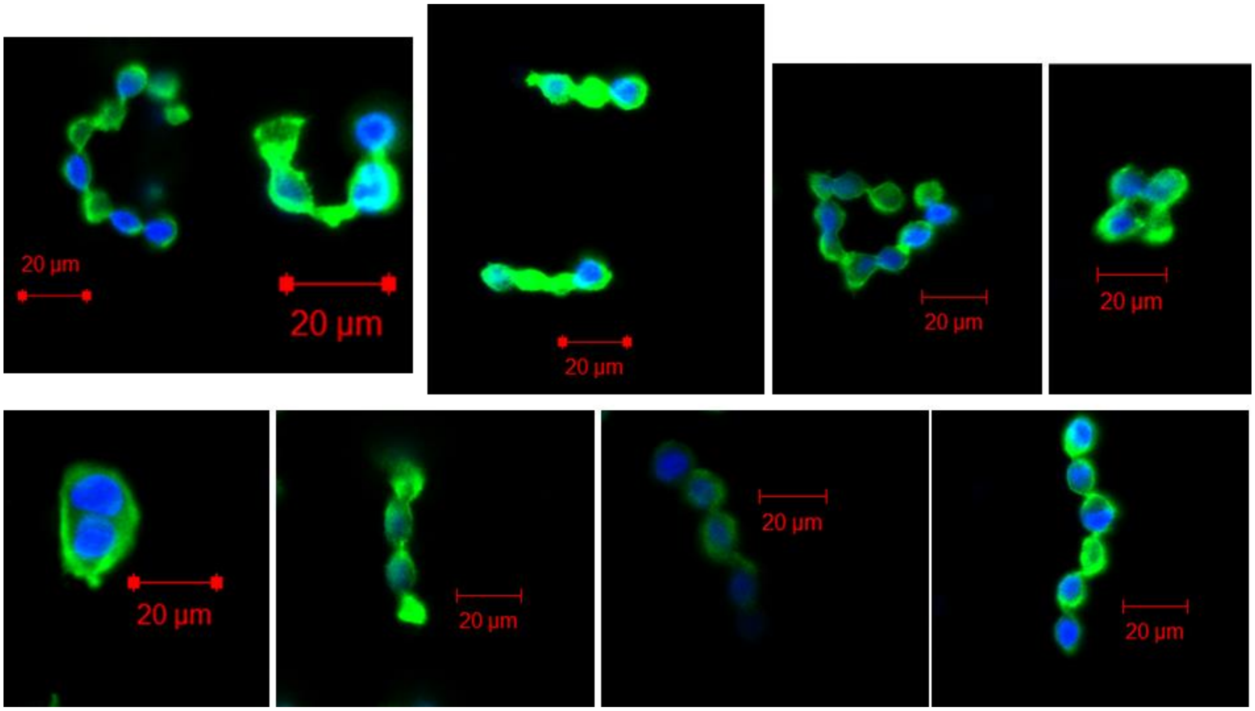

Fig. 21 Confocal images of a range of cells fusing after being arranged into a range of shapes including: letters, parallel lines, rings, and lines of varying lengths. Cytoskeletons are stained with Phalloidin, and nuclei are stained with DAPI.

In all cases, the cells are fusing; however, the ability to pattern cells that develop beyond the initial hourglass like fused structure remains inconsistent. In most cases, the cells that are encapsulated in hydrogel remain round, showing no signs of having an organized cytoskeleton containing functional myofibrils. In order to form functional myofibrils, there needs to be some organization of the actin filaments, along with other proteins inside the cells. This developmental step is critical as it affects the ability of the C2C12's cells to contract. Cells that are not encapsulated within hydrogel readily accumulate along the perimeter of the hydrogel and form actin filaments within 7 days, as shown by the notable vertical striations in Fig. 22. From this result it is hypothesized that the hydrogel is confining the cells, preventing the ability to form fully functional myotubes. Several strategies to overcome this problem are presented in the next section, and chapter to follow.

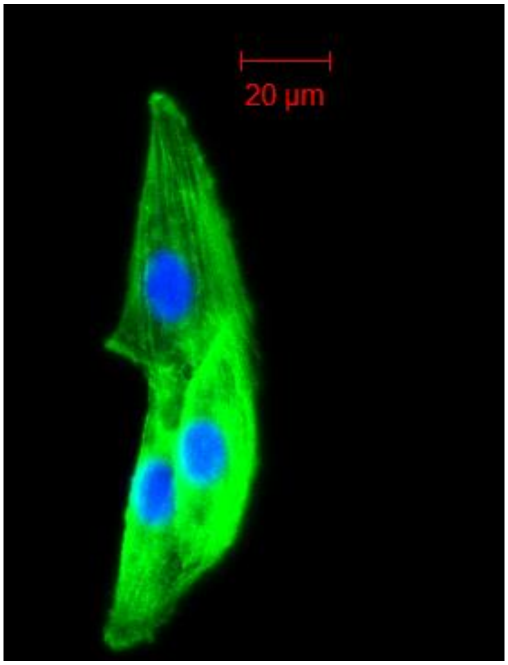

Fig. 22 Cells that grow around the perimeter of the hydrogel voxels readily form actin filaments are shown in the Phalloiden stain as vertical lines along the length of the cell.

4.4 Conclusions

This work demonstrates that thiol-ene can be used to pattern structures with cellular resolution. When LAP is used as a photoinitiator, the hydrogel rapidly polymerizes. This removes the need to pre-cure, and results in more consistent feature dimensions. For comparison, when a series of 8 structures were polymerized, feature diameters were found to vary by 16 % in thiol-ene as compared to 400 % in PEGDMA.

To assess viability, multiple LIVE/DEAD assays are completed. Cells encapsulated in thiol-ene without RGD that are incubated for 4 days showed improved viability over that of PEGDMA. Maximum viability is seen when cells are patterned in thiol-ene with RGD. Cells encapsulated in a degradable thiol-ene with RGD that are incubated in differentiation media are shown to fuse within 4 days, indicating differentiation that could lead to the formation of a multi-nucleated cell.

However, cells encapsulated in the degradable thiol-ene are clearly not forming actin filaments in the cytoskeleton. It is hypothesized that this is because the hydrogel is confining the cells, preventing the ability to differentiate into myotubes. Consistent with previous work [8,9,10] cells that grow along the perimeter of the hydrogel readily form myotubes. This supports the conclusion that edges are critical for myotube formation, and suggests that a fully 3D geometry in which lines of cells are suspended in a monomer tube surrounded entirely by gel would be optimal for 3D patterning of myotubes. However, this will require advancements to the axial confinement of polymerization. With the current system, it would be possible to pattern a hydrogel layer. The layer could lifted, and cells could be arranged in a line and a hydrogel ring could be patterned around the cells. However, liquid monomer would still exist between the cells. As a result, if one were to try to pattern a third hydrogel layer below the ring, the defocused light would have sufficient power to polymerize the liquid monomer between the cells.

Strategies have been demonstrated to improve axial confinement of one photon lithography by adding absorbers, such as Tinuvin. This limits optical penetration in fabricated layers. This has been used to pattern acellular structures that were later seeded with cells [69]. However, to my knowledge, research has not been completed to validate biocompatibility of Tinuvin for live cell lithography. This remains a topic of future research.

Alternatively, the use of a femtosecond laser in combination with a two-photon initiator would allow far superior axial confinement. This is because the probability of simultaneous excitation by two photons is proportional to the square of the light intensity, and thus excitation decays with the fourth power of distance from the focal point [70] as shown in Fig. 23. However, moving to two-photon polymerization is a significant change requiring an expensive laser. This leaves two remaining options for patterning desired structures, which are discussed to follow.

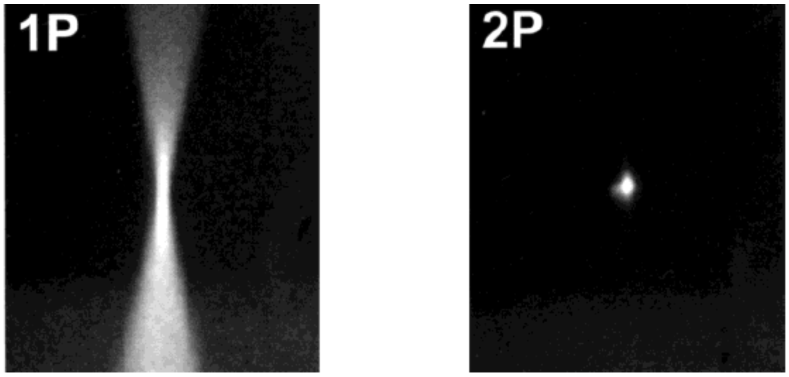

Fig. 23 Intensity profile of one photon polymerization vs. two photon polymerization. When polymerizing with a femtosecond laser and a two photon initiator, axial confinement is significantly enhanced as the intensity of the polymerizing source falls by the fourth power of the distance from the focal point [71].

The first option is to move to a 100% degradable hydrogel fabricated by crosslinking PEG macromers with matrix metalloproteinase (MMP) sensitive peptides. This type of hydrogel, shown in Fig. 24, is degradable by the cells in response to the secretion of MMP. Thus, the hydrogel selectively degrades only around the cells, allowing mobility for myotube formation while simultaneously providing 3D biomechanical cues to influence differentiation. Furthermore, it is possible to tailor the degradation rate from several days, to weeks, months or even years. The hydrogel has been used to study a variety of cell types including studies of: human dermal fibroblast migration through MMP degradable scaffolds modified with RGD [72], primary bovine chondrocytes [73], valvular interstitial cells [74], and human mesenchymal stem cells [75]. However, this approach requires extensive studies to tune the hydrogel degradation properties.

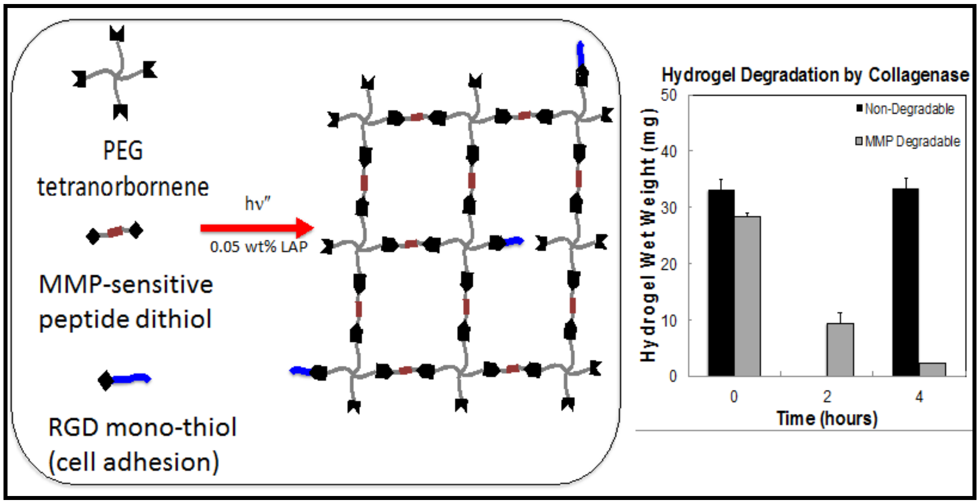

Fig. 24 Biomimetic hydrogel platform formed from a thiol-ene click reaction by photopolymerization. (left) Schematic of biomimetic hydrogel formed from macromers of PEG tetranorbornene, MMP-sensitive peptide dithiol, which serves as the crosslinker, and RGD mono-thiol, which provides cell adhesion sites. (right) Confirmation of degradation for a MMP degradable hydrogel formed with the crosslinker, CVPLSLYSGC, which can be degraded by several MMP's including MMP 1,2,3,7 and 9 [76]. Degradation is confirmed by placing the hydrogel in a solution containing a high concentration of collagenase (100 U/mL collagenase type I), which led to accelerated degradation. When the crosslinker was PEG-dithiol, no degradation was observed. Data presented as mean with standard deviation as error bars (n=6).

The second option is to pattern a more complex sample consisting of two hydrogel materials. In studies completed thus far, it is observed that cells accumulate on the exterior perimeter of the hydrogel structure encasing patterned cells, and these cells form actin filaments. To replicate this boundary, but add the control of patterning, one approach is to pattern a series of hydrogel edges, arrange the cells along the perimeter of the hydrogel using holographic optical tweezers, and then encase the organized cells in a hydrogel with a low crosslink density. It is hypothesized that this will provide the cells the required mobility to fuse and differentiate. This option is explored in the chapter to follow.

5 Patterning cells in a multi-material system

The research completed demonstrates the ability to arbitrarily pattern cells in a degradable hydrogel, and consistently results in fusion of the cells. However, encapsulated cells maintain a round morphology, and fail to form actin filaments. Cells that are not encapsulated in the hydrogel readily accumulate along the perimeter of the hydrogel, fuse, and form actin filaments. From these results, it appears that the hydrogel is constraining the cells, preventing formation of fully functional myotubes. The goal of this section is to use two hydrogels to both pattern the C2C12 cells and to guide their development into myotubes. The first hydrogel structure will give the cells a boundary to grow along that is similar to the perimeter of the hydrogel previously used to encapsulate patterned cells. The second hydrogel is used to hold the arranged cells in place, but this hydrogel has a low crosslink density. It is hypothesized that the low crosslink density hydrogel will allow the cells mobility for development, but will still enable structured patterning of cells.

5.1 Materials and methods

The work in this chapter investigates C2C12 cells placed via HOT along the perimeter of a thiol-ene hydrogel with a high crosslink density and encased in a secondary hydrogel with a low crosslink density. The thiol-ene hydrogel with the high crosslink density is comprised of 10 wt. % 8-arm PEG-norbornene with an ester link dissolved in PBS, 0.05 wt. % LAP photoinitiator, 3.2 wt. % PEG-dithiol, and 0.135 wt. % CRGDS. This monomer has a stoichiometric ratio of 0.8 of thiol-to-ene.

The thiol-ene hydrogel with a low crosslink density consists of C2C12 cells suspended, at a density of 1×10^6 cells/mL, in a monomer solution comprised of 10 wt. % 8-arm PEG-norbornene with an ester link dissolved in PBS, 0.05 wt. % LAP photoinitiator, 1.6 wt. % PEG-dithiol, and 0.135 wt. % CRGDS. This monomer has a stoichiometric ratio of 0.4 of thiol-to-ene.

To prevent samples from detaching from the coverslip, a mercaptopropyltriethoxysinale (MPTS) coating is used. Prior to use of this coating approximately 60% of samples were lost to detachment from the coverslip during the incubation period after patterning. With this coating all samples remain attached, and the coating had no visible adverse effects on C2C12 cell development. The coating materials and coating procedure is as follows:

1. Pipette 90 mL of 95% ethanol into a polypropylene cup.
2. Slowly add drops of glacial acetic acid to adjust the pH to 4.5 to 5.5.
3. Add 250 uL MPTS. Allow the solution to react for 5 mintues.
4. Submerge coverslips in the ethanol/silane solution for 2 to 3 minutes.
5. Rinse coverslips with 95% ethanol.
6. Bake slides at 80°C for 15 minutes.
7. Store slides at -20°C until use. Slides are only stable at room temperature for one to two days.

5.2 Live-cell 3D lithography via HOT and micro-stereolithography in a multi-material thiol-ene monomer

A two-step procedure is used to pattern the samples. First, a series of 10 hydrogel voxels are patterned on a coated coverslip. Each polymer voxel is patterned by exposing an area of 43 µm x 128 µm to 405 nm illumination. Each exposure is one second in duration with a power of 56 mW/cm^2. The exposures are repeated either two or three times. Two exposures results in polymer voxels slightly larger in scale than the area illuminated. Three exposures results in features much larger than the area exposed. The voxels are separated by 200 um, as shown in Fig. 25.

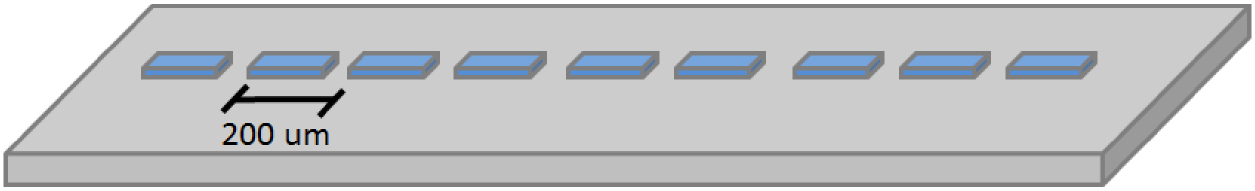

Fig. 25 3D view of patterned 8 Arm PEG Norborene rectangles on coverslip. The distance from the edge of one rectangle to the edge of the next is 200 um. Each rectangle is close to 100 um long. If the hydrogel feature is over-exposed by repeatedly curing the same area, then the dimensions are larger.

Currently, the fabrication system only supports brightfield imaging, and the index difference between the patterned voxels and the surrounding liquid monomer is very low, making the patterned voxels difficult to find when arranging cells. For example, polymer voxels shown in Fig. 26 and Fig. 27 are patterned, rinsed twice with PBS and re-submerged in PBS to prevent drying. Images of the voxels that are taken from the Cube are shown at left, and are shown at right as they appear after post processing using ImageJ to enhance contrast. As shown, the polymer voxels are very difficult to see. Overexposing to make much larger structures makes finding the voxels to pattern the cells easier.

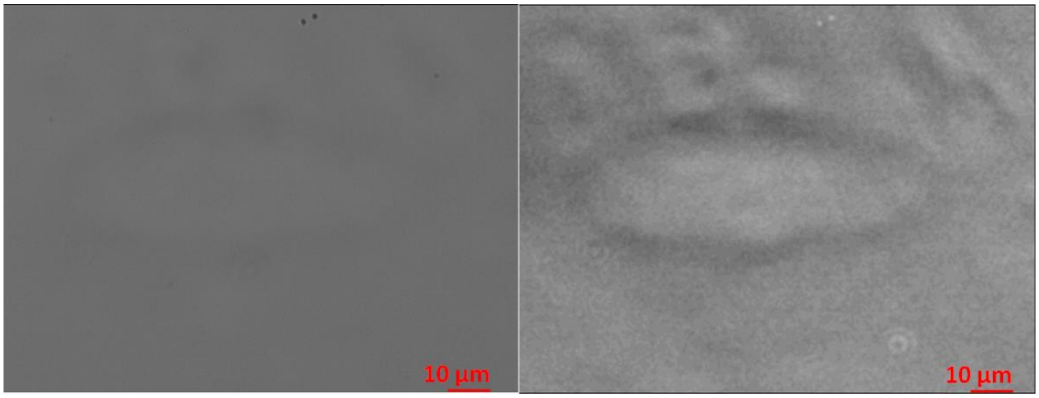

Fig. 26 Polymer voxel submersed in PBS that is fabricated by exposing an area 128 µm x 42 µm to TWO 1 second 405 nm exposures with a power of 56 mW/cm^2 (left) brightfield image taken in the Cube (right) Using contrast enhancement with ImageJ to make the polymer feature easier to visualize

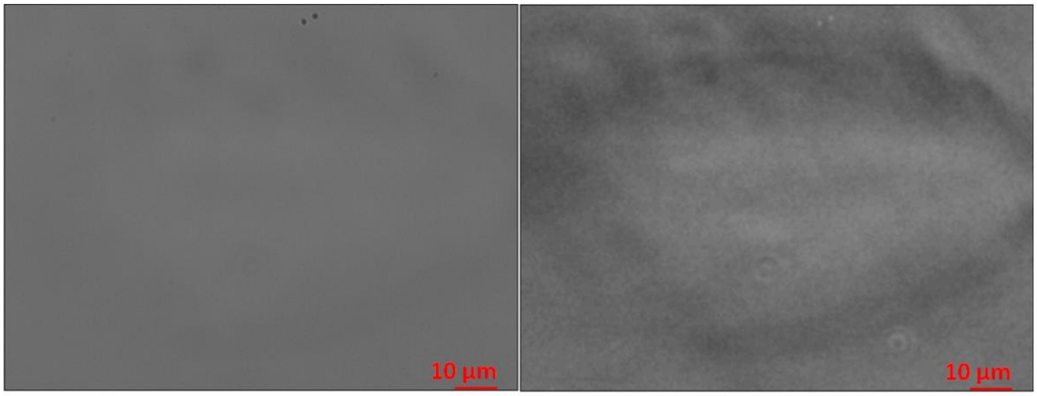

Fig. 27 Polymer voxel submersed in PBS that is fabricated by exposing an area 128 µm x 42 µm to THREE 1 second 405 nm exposures with a power of 56 mW/cm^2 (left) brightfield image taken in the Cube (right) Using contrast enhancement with ImageJ to make the polymer feature easier to visualize

When patterning samples with cells, the polymer voxels patterned in the first step are rinsed twice with PBS without removing the coverslip from the Cube to ensure that the sample remains aligned with the imaging optics. Then, the secondary monomer solution that contains cells is then deposited on the sample. Optical tweezers are used to arrange cells around the polymer voxels with the high crosslink density. After arranging cells, the pattern is held in place by exposing an area of 343 µm x 343 µm to two 405 nm exposures each 1 second in duration with a power of 56 mW/cm^2. This over-exposes the monomer, readily polymerizing a large hydrogel voxel with a low crosslink density to hold the cells in place. A diagram of step 2, and an image of the resulting patterned structures are shown in Fig. 28.

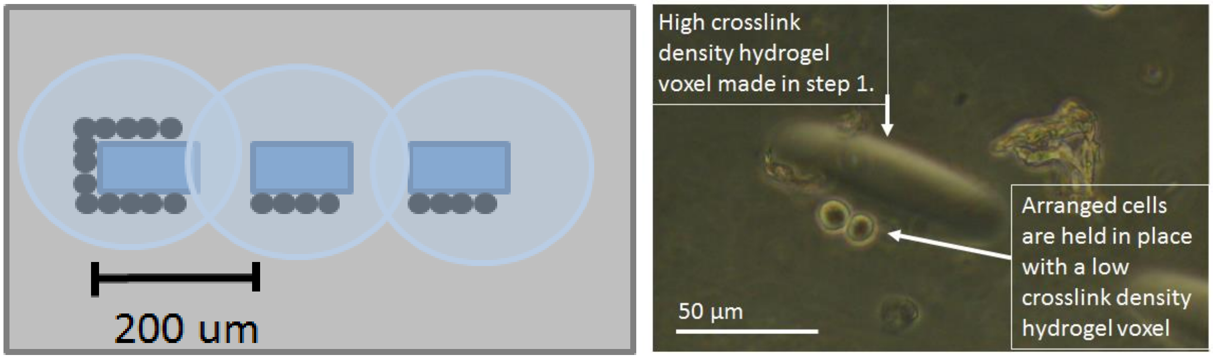
200 um
High crosslink density hydrogel voxel made in step 1.
Arranged cells are held in place with a low crosslink density hydrogel voxel
50 µm

Fig. 28 (left) Top view of cells (shown as black circles) arranged around the polymer voxels patterned in step 1 (marked with dark blue). The cells are held in place in a hydrogel with a very low crosslink density (marked as light blue circles.) (right) patterned two hydrogel sample with two cells arranged along the border of the hydrogel voxel with the higher crosslink density.

In Fig. 29, a brightfield image of a sample is shown just after patterning, and after incubating at 37 °C and in 5% CO_2 in differentiation media for 2 days. Two polymer voxels are shown with a series of 10 cells pattered around the voxel at left, and 8 cells patterned along the bottom of the voxel at right. After incubation, a large multi-nucleated cell fused along the perimeter of the hydrogel voxel with the low crosslink density, as shown along the top portion of Fig. 29(right). The cells patterned into a line along the left hydrogel voxel with the high crosslink density broke into two parts. The top 4 cells of this line grew into the cell along the perimeter of the hydrogel voxel with the low crosslink, as shown in the confocal image of Fig. 29. The remaining cells maintained a generally round morphology, only showing initial signs of fusing.

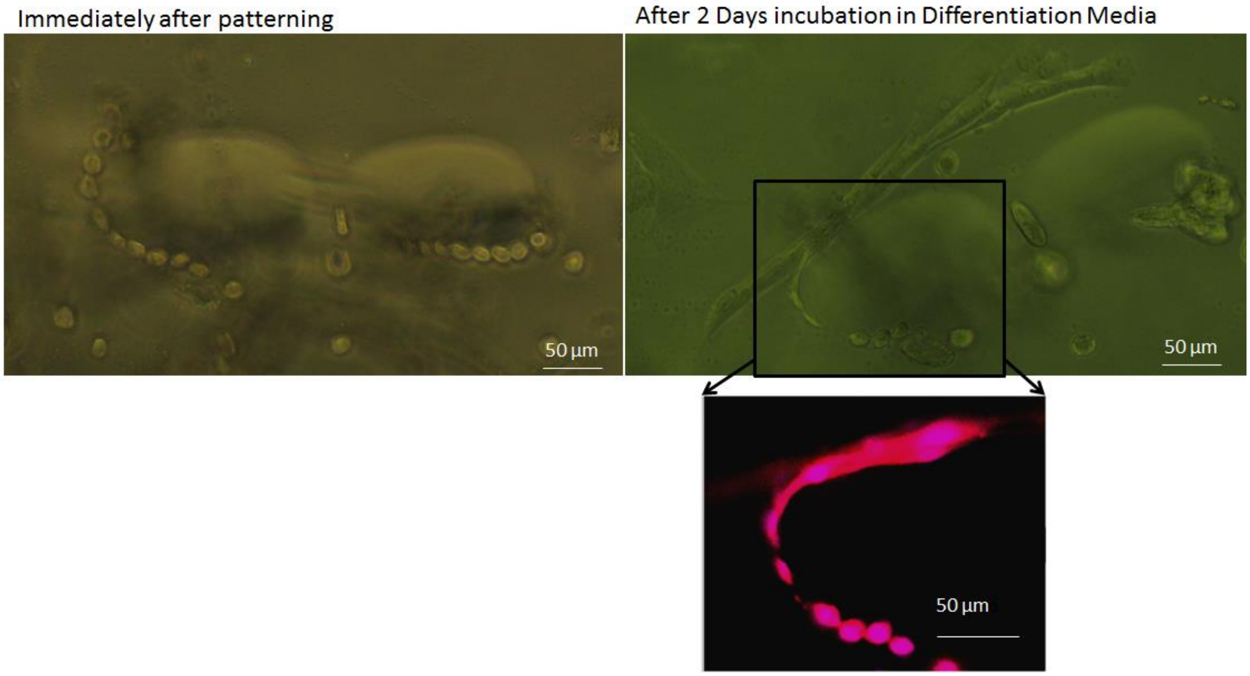
Immediately after patterning

After 2 Days incubation in Differentiation Media

Fig. 29 (a) Brightfield image cells patterned along the perimeter of two hydrogel voxels with a high crosslink density that are encased in a secondary hydrogel with a low crosslink density. (b) Brightfield image of the sample after 2 days incubation in differentiation media (c) Confocal image, 40x water immersion. The cytoskeleton was stained with rhodamine phalloidin, and DAPI stained the nuclei. The first 4 cells on the left high crosslink density voxel joined the very long cell that grew along the perimeter of the hydrogel with the low crosslink density. However, the cells on the right high cross linking density voxel collapsed into an undefined ball during the 2 day incubation period.

A sample with 15 cells arranged around the high crosslink hydrogel voxel is shown in Fig. 30. A brightfield image taken immediately after patterning is shown without markings at left, and with markings along the perimeter of the high crosslink hydrogel, and low crosslink hydrogel at right. In Fig. 31 the brightfield images of the sample can be seen before and after incubation. A large cell grew around the perimeter of the hydrogel with the low crosslink density, indicating that in the span of 2 days cell fusion is occurring. Within the hydrogel with the low crosslink density the cells along the top right of the hydrogel voxel with the high crosslink density are fusing, but remaining cells are not. In the confocal image of Fig. 32, it is apparent that more cells have multiple nuclei, but as a result of replicating as opposed to fusing. The consistent growth of large cells around the perimeter of the hydrogel is shown in Fig. 33.

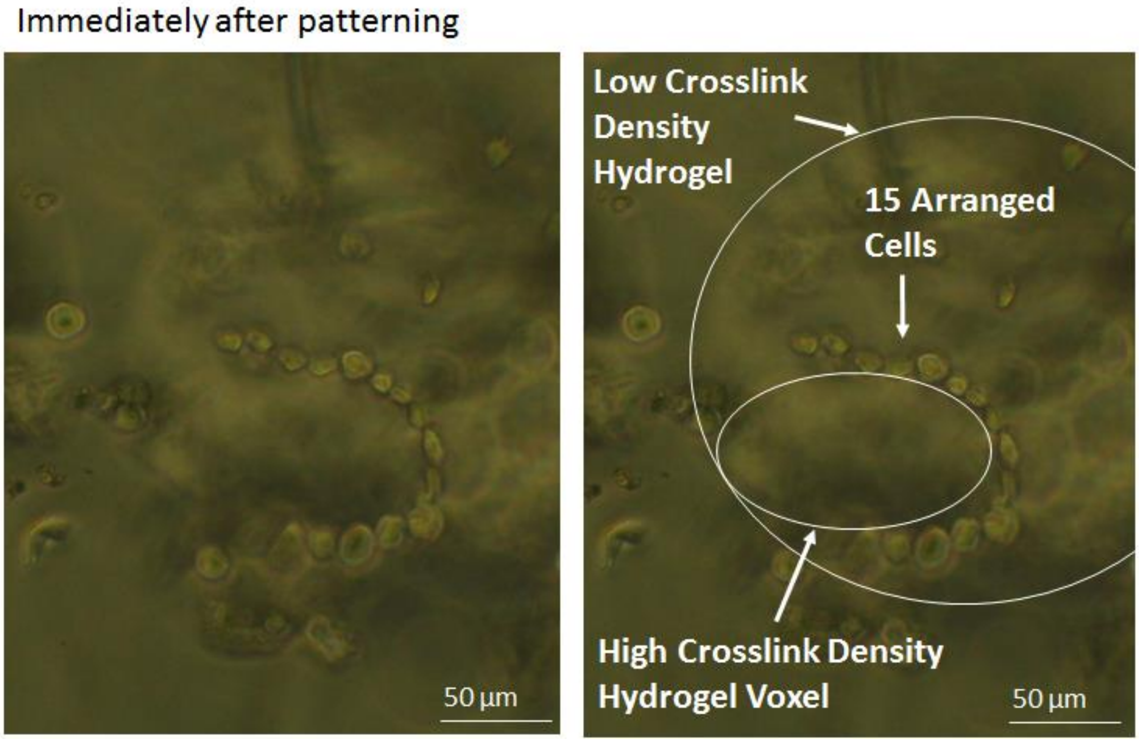
Immediately after patterning
Low Crosslink Density Hydrogel
15 Arranged Cells
High Crosslink Density Hydrogel Voxel
50 µm
50 µm

Fig. 30 Brightfield image of cells arranged around a hydrogel voxel with a high crosslink density, and encased in a significantly larger hydrogel voxel with a low crosslink density. An unmarked image is shown at left, and at right key features are noted

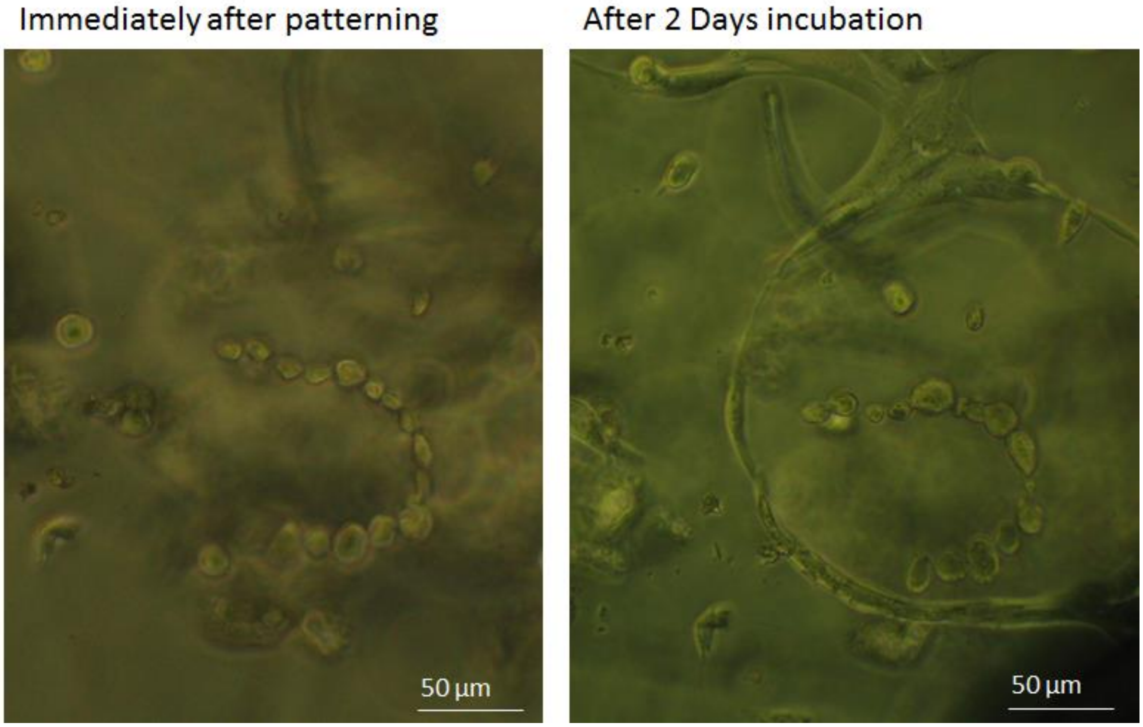
Immediately after patterning
After 2 Days incubation
50 µm
50 µm

Fig. 31 Brightfield image of 15 cells patterned around a polymer voxel with a high crosslink density, and encased in a secondary polymer voxel with a low crosslink density (left) just after patterning (right) after 2 days incubation.

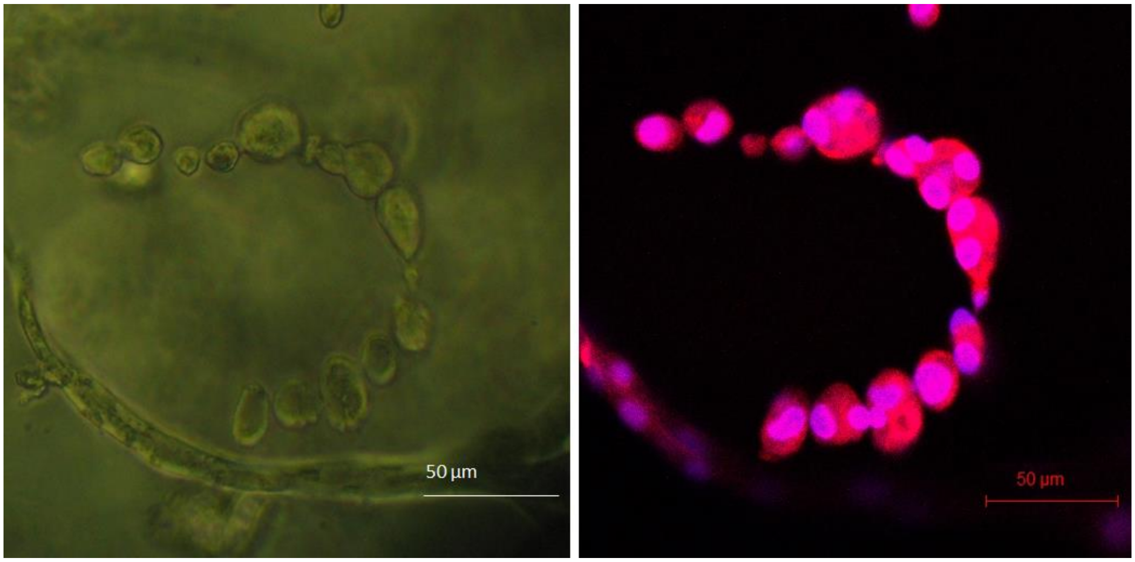

Fig. 32 (left) brightfield image of arranged cells after incubation (right) confocal scan of arranged cells with Rhodamine Phalloidin staining the cytoskeleton, and DAPI staining the nuclei.

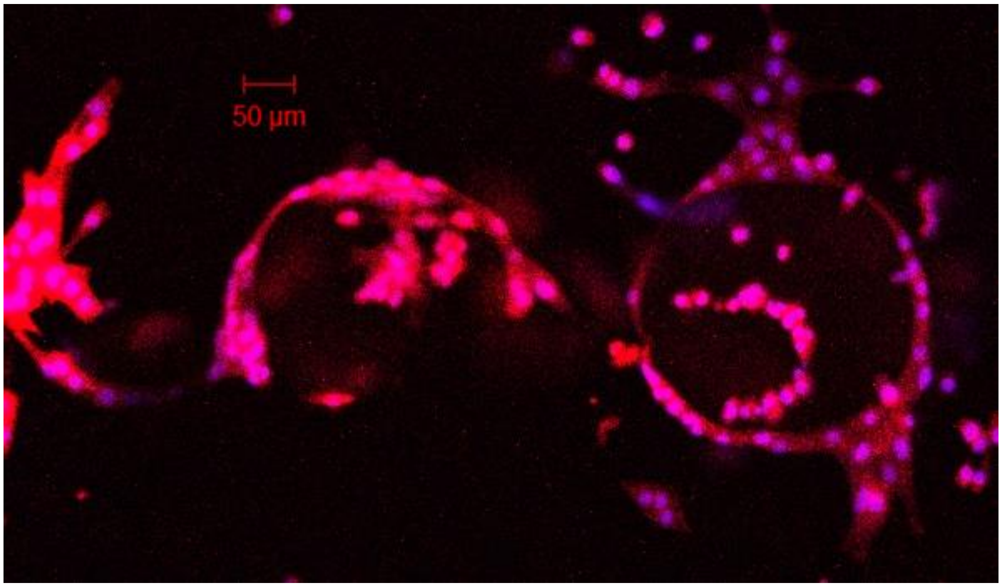

Fig. 33 Cells consistently grow along the perimeter of the hydrogel with the low crosslink density, shown as a series rings in the confocal image above.

5.3 Conclusions

This chapter explored the possibility of using the perimeter of a hydrogel with a high crosslink density to guide myotube formation, while using a hydrogel with a low crosslink density to support cells. It was hypothesized that the low crosslink density hydrogel would be sufficiently strong to hold the cell in place after patterning, but weak enough to allow the cells mobility to fuse. It was found that even a very low cross linking density hydrogel did not provide sufficient mobility to allow for consistent formation of multi-nucleated cells. It is hypothesized that degradation of the hydrogel was not sufficiently fast and localized around the cells to allow mobility for fusion. A topic of future research will be investigations of cell fusion in MMP degradable thiol-ene hydrogel. This hydrogel is selectively degraded by the cells, allowing strength to support the cells, but an absence of hydrogel immediately surrounding the cells such that fusion and myotube formation can occur.

6 The Pocketscope

Optogenetics is an emerging technology that combines genetics with optical methods to monitor and manipulate the activity of specific populations of 10's to 100 neurons at a time [77,78]. The approach has the potential to improve accuracy in mapping function to neural circuits of the brain, and mental illness to circuits that have been compromised. This is shown by research that has led to an improved understanding of epilepsy [79], depression [80], drug addiction [81], and Parkinson's disease [82]. The potential of optogenetics to improve understanding of neurological diseases, and reduce projected healthcare costs has led to multiple large-scale national and international efforts including: the Brain Initiative, the Brain Activity Map (BAM) and the Human Brain Project.

Optogenetics relies on two complimentary techniques: Calcium imaging to monitor neural activity and photostimulation to manipulate neural activity. Calcium imaging is made possible through calcium indicators, which are fluorescent molecules that can be introduced into tissue such that fluorescence microscopy can be used to track action potentials. When an action potential occurs, there is a rapid uptake of calcium into the cell body, allowing calcium ions in the soma to interact with calcium indicators present within the cell body. This interaction alters the characteristics of the bound calcium ions, changing their fluorescence properties making the action potential an optically detectable event.

There are two types of calcium indicators: chemical indicators such as Fura-2, and genetically encoded indicators such as GCaMP. Chemical indicators are typically bound to chelator groups, enabling the indicator to readily permeate the cell membrane, thus loading the sample. Fura-2 is excited at 350 nm and 380 nm and the ratio of emissions at the two excitation wavelengths is directly correlated to the amount of intracellular calcium. Thus, using this ratio it is possible to cancel variables, such as dye concentration and cell thickness, allowing Fura-2 to be used simultaneously as an indicator of cellular activity as well as a quantitative measure of intracellular calcium levels.

As an alternative to chemical indicators, genetically encoded indicators can also be used for calcium imaging. The benefits of genetically encoded indicators is that they do not require loading, and offer greater stability for chronic imaging. Genes encoding proteins are transfected to cell lines, or transgenic animals expressing the dye can be created. This indicator operates through a conformation change that leads to emitted fluorescence when GCaMP binds with calcium ions.

Photostimulation is a complimentary capability to calcium imaging, allowing the ability to either cause or silence action potentials. For example, RuBi-glutamate cleaves when illuminated, stimulating glutamate receptors in a neuron, causing an action potential. Alternatively, when Halorhodopsin is illuminated it leads to an influx of chloride ions in a cell body, leading to hyperpolarization of the cell which inhibits action potentials. A wide range of opsins for photostimulation having varying properties relating to the response time, sensitivity, excitation, and emission wavelengths [83] have been developed and are available through the Deisseroth lab.

Multiple approaches to instrumentation for optogenetics are emerging including: optical fibers, and microscopes that include either digital micromirror arrays (DMD), or nematic liquid crystal based spatial light modulators (NLC SLM). Several research projects have demonstrated optical fiber-based illumination for stimulating neural circuits [80, 84]. The benefits of optical fibers are that they can be implanted and left deep within the brain for chronic experiments with photostimulation over the span of up to a year [85]. The flexibility of the fiber allows the animal full mobility, enabling studies in complex environments such as water and mazes. However, optical fibers only allow photostimulation in broad regions of the brain, meaning that the ability to study circuits with single cell resolution is lost. For this reason optical fibers are commonly used to isolate a region of interest within the brain, and that region is then further analyzed with single cell resolution, using alternative techniques.

To improve spatial resolution to the single cell level, approaches using DMDs and NLC SLMs are being explored. Both approaches require the mouse head to be held fixed under a microscope. The mouse has less mobility than fiber based approaches, but is typically able to run on a ball, and can be presented with a computer-generated scene to provide visual stimuli. The skull is either removed or thinned such that the region of interest can be viewed. A coverslip is sealed over the hole in the skull, resulting in a chronically implanted window enabling long-term studies of neural circuits [86]. When a DMD is used, the array is imaged to a two-dimensional plane in the sample, allowing selective illumination of regions of the brain for calcium imaging and/or photostimulation. This approach allows for high speed targeting of cells at rates of 23 kHz – 32 kHz [87]. However, because light is utilized in the image plane as opposed to the Fourier plane, this approach does not provide a means to monitor and manipulate neural circuits within a three dimensional volume, and light is used inefficiently when targeting a low density of cells.

Alternatively, NLC SLMs can be operated in the Fourier plane, selectively redirecting incident illumination within a three dimensional volume in the focal plane of an objective lens. If one is attempting to illuminate a sparse volume of focal points, this approach maintains efficient use of light. However, NLC SLMs have a demonstrated maximum response time of 500 Hz [88], which is not ideal for mapping neural activity when action potentials can occur within a single millisecond. Further, 100% diffraction efficiency and uniformity of the diffracted spot intensity is challenging. To maximize the dimensions of the addressed volume, it is desirable to align the system such that the 0th order is in the center of the field of view. If a significant amount of light is lost into the 0th order, and the 0th order is not entirely blocked, then this light can damage cells, or influence measurements of activity. The compounds used for photostimulation and calcium imaging are designed to be highly sensitive, capable of responding to as little as 8 mW/mm^2 [89]. This enables low incident power to manipulate and monitor activity, decreasing the likelihood of damaging the sample. However, this means that even if a small fraction of light is present in ghost orders, or the 0th order, it is potentially sufficient to influence a measurement.

The chapters to follow present the design, implementation and demonstration of an inexpensive one photon microscope, referred to as the “Pocketscope” incorporating an NLC SLM that enables calcium imaging and photostimulation to map neural circuits in brain slices. Algorithms were created to minimize losses to the 0th order and ghost orders. The SLM has switching speeds of up to 500 Hz, enabling temporal sequence through targeting patterns to study the response of a surrounding network to stimulation of a series of neurons. The tool can be used to study wide range of samples, from single dendritic spines to larger three dimensional populations of neurons, and allows study of complex neural activity such as the integration of inputs arriving on multiple dendritic branches, which is by its nature a three dimensional problem

This work is a collaborative effort with Rafael Yuste at Columbia University, making the division of tasks important to note. I was solely responsible for all work completed at BNS on the STTR. This chapter describes the opto-mechanical system and software. I designed the optoelectronic system and wrote the control software, while Columbia provided guidance on the optogentic application. Chapter 7 motivates the need for improved beamsteering efficiency and describes two approaches I implemented. Finally, I took the tool to Columbia where we tested it for fast 3D calcium imaging of neurons in brain slices. The materials and methods used to prepare brain slices are documented in Chapter 8. This procedure was developed by Prof. Yuste at Columbia University. All animal handling and experimentation was performed according to NIH and local IACUUC guidelines. I did not directly handle brain slices, but once the brain slice was placed in the system I worked with Prof. Yuste's group to gather the results presented in Chapter 8.

6.1 The Pocketscope Optics

The optical layout of the Pocketscope is shown in Fig. 34. Below the sample a white light LED and fold mirror are used for brightfield imaging. This enables the software to auto-detect the positions of objects to target within a field of view of 470 µm x 635 µm in a maximum of 10 planes separated by 10 µm. After the locations of cell bodies have been detected, the software automatically computes a hologram such that when the SLM (Boulder Nonlinear Systems, PDMHS512-532) is illuminated by the 488 nm laser the system can be used for targeted calcium imaging and photostimulation.

An optical relay is used to image the SLM to the back aperture of the microscope objective (Olympus, LUMPLFLN40X/W), and is also used to de-magnify the image of the SLM by 60%. Underfilling the objective with the image of the SLM effectively reduces the pixel pitch, enabling the SLM to generate targeted excitation points with a field of view that spans 440 µm x 440 µm. However, the demagnification reduces the NA of the excitation, expanding the radius of the waist of a diffraction limited 1st order spot from 0.366 µm to 0.915 µm. Likewise this increases the axial extent of the depth of focus from 0.915 µm to 5.71 µm. This is an acceptable tradeoff for targeting cell bodies which typically have a diameter of approximately 10-20 µm, but could be limiting for studies of smaller features such as dendritic trees or dendritic spines.

As shown in Fig. 34, a dichroic can be placed between the fold mirror, and the fluorescent filter cube such that single focal point or wide field photostimulation can be used in conjunction with calcium imaging. This enables the ability to perturb activity of neural circuits by inducing or silencing activity. Calcium imaging can then be used to monitor the response of the circuit to the perturbation.

The sample is imaged to the camera (Dalsa, Genie M10240) by relaying the intermediate plane to the camera. The imaging system de-magnifies the image of the sample by 66%, such that a 470 um x 630 um area within the sample is imaged onto the 3.5 mm x 4.7 mm active area of the camera. The Fourier plane in the relay system enables extended depth of field imaging, as will be discussed to follow.

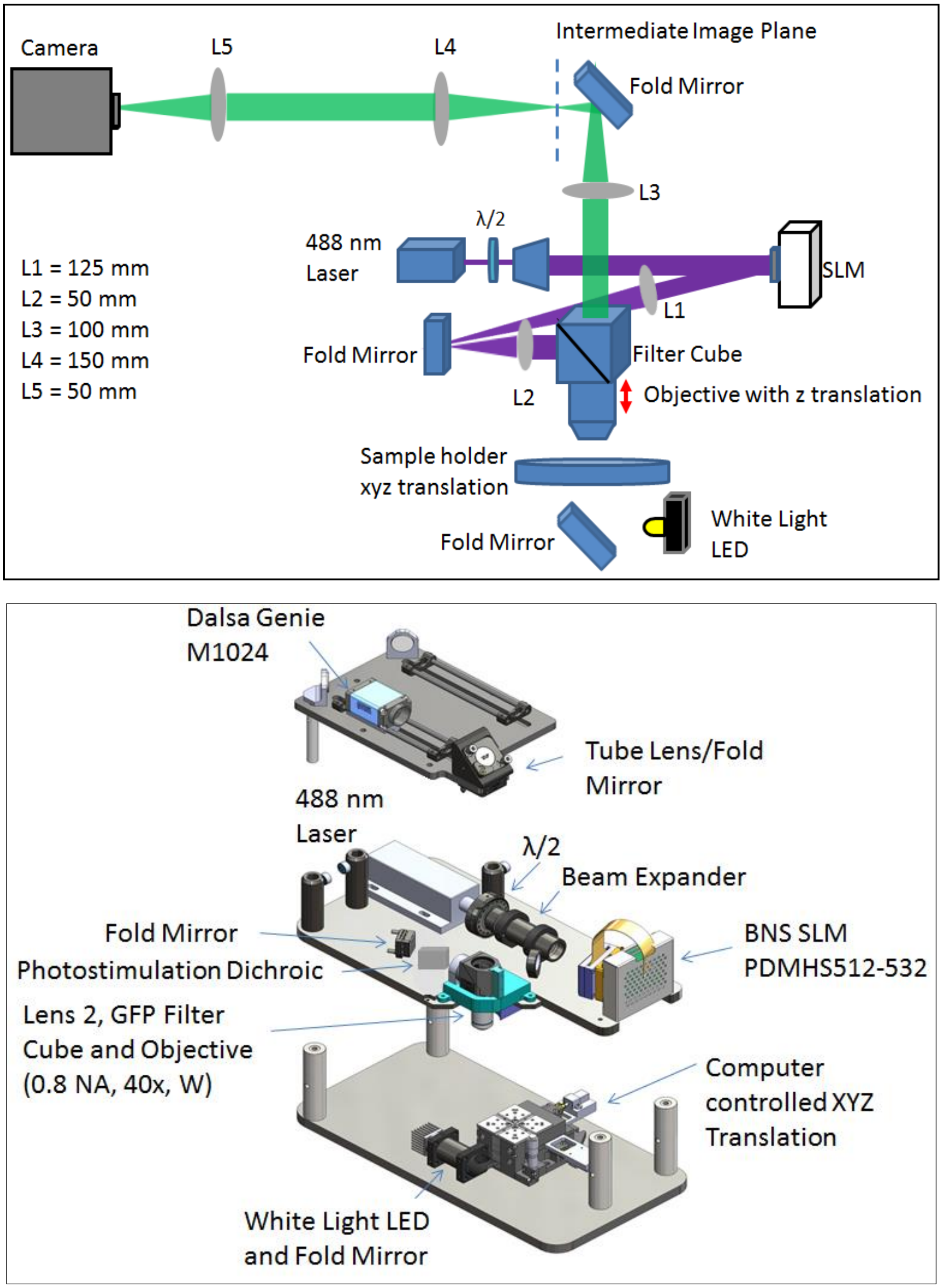
Camera
L5
L4
Intermediate Image Plane
Fold Mirror
L3
λ/2
488 nm
Laser
SLM
L1 = 125 mm
L2 = 50 mm
L3 = 100 mm
L4 = 150 mm
L5 = 50 mm
L1
Fold Mirror
Filter Cube
L2
Objective with z translation
Sample holder
xyz translation
White Light
LED
Fold Mirror
Dalsa Genie
M1024
Tube Lens/Fold
Mirror
488 nm
Laser
λ/2
Beam Expander
Fold Mirror
Photostimulation Dichroic
BNS SLM
PDMHS512-532
Lens 2, GFP Filter
Cube and Objective
(0.8 NA, 40x, W)
Computer
controlled XYZ
Translation
White Light LED
and Fold Mirror

Fig. 34 Optical layout of the Pocketscope (top) and mechanical layout (bottom).

In order to image neural activity within a 3D volume the system is designed to support two imaging modalities. In the "traditional" modality, the objective is mounted on a piezo-driven translation stage (Edmund Optics, 85-008). The stage can translate across a maximum range of

100 µm, with a step response time of 20 ms. As the objective translates it is possible to add defocus to the SLM such that the plane of excitation and imaging do not need to be co-aligned. Further, the SLM can be used to correct for aberrations caused by targeting neurons deep within scattering tissue.

The “modern” modality, as an alternative to 3D imaging through time sequentially scanning of 2D planes, is to make use of extended depth of field imaging through wavefront coding. This concept was first demonstrated in 1995 by Dowski et al. [90] who added a cubic phase mask to the imaging arm of a microscope. If the mask is placed in the pupil plane of the image, it introduces a strong aberration that overwhelms other aberrations present in the image, including defocus. This can be used to modify the point spread function of fluorescent sources within the sample such that the axial variance of the transverse profile of the PSF is slowed, as shown in Fig. 35. By post processing the images through a deconvolution routine, the aberration can be removed, leaving a projection of the volume onto a single plane., The depth of field has been demonstrated to increase by a factor of up to 10x [91], however, the extent over which the depth of field can be extended is dependent on the NA of the imaging system. The Pocketscope is designed to be compatible with extended depth of field imaging, but demonstration remains a topic for future research.

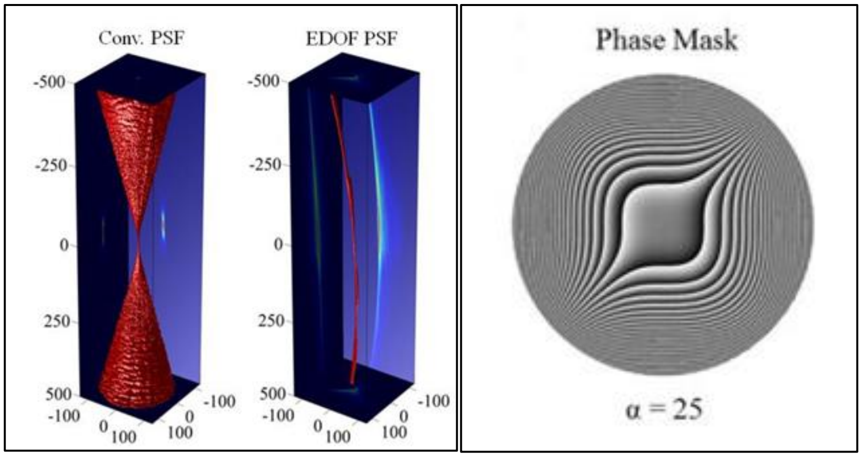

Fig. 35 Cubic phase mask used to extend the depth of field of a fluorescent imaging system [Error! Bookmark not defined.**] (left) the point spread function of a conventional microscope as compared to that of an extended depth of field microscope (right) cubic phase mask.**

6.2 Automated Cell Body Detection

A range of techniques have been demonstrated for identifying the locations of cell bodies, using approaches of segmentation and edge detection [92]. In this work, cell bodies are detected through a correlation routine which offers simplicity and high speed detection with an accuracy of 94 %. An example of automated cell body detection is illustrated in Fig. 36. The brightfield image of a brain slice loaded with calcium indicators is shown Fig. 36a. The image is analyzed in a raster fashion, first applying a threshold condition to ignore pixel values below a minimum peak value, as shown in Fig. 36b. The algorithm then searches for pixel peaks that are greater than the surrounding 5x5 pixel values. For this example 147 peaks were found. Each peak is then correlated with a Gaussian peak that is 7 pixels in diameter. If the correlation is sufficiently high, then the location is noted as a cell body. To determine an appropriate minimum peak value for a fluorescing object, pixel values are dynamically reported as the mouse is translated across the camera output.

For comparison of this approach and others, cell bodies are detected using threshold conditions and edge detection algorithms built into ImageJ, as shown in Fig. 37. The same brightfield image of a brain slice loaded with calcium indicators is used in this example. In Fig. 37b, threshold conditions are applied using Image J, using the same lower bound from the previous example. In Fig. 37c, the Image J edge detection technique is utilized to identify the location of cell bodies. In Fig. 37d an overlay is shown of cell body locations detected with the Pocketscope, and with ImageJ. In Fig. 37e cell bodies that were detected by Image J, but were not detected by the Pocketscope software are noted. From this example, 7 of 109 cell bodies present were not detected with the Pocketscope algorithm. The reason is that a peak within these cells that is greater than the surrounding 5x5 pixels. To improve auto-detection, better methods to identify peaks must be utilized. Although the Pocketscope algorithm results in a decrease in automated cell detection accuracy of 6%, the Pocketscope algorithm offers speed and simplicity of implementation.

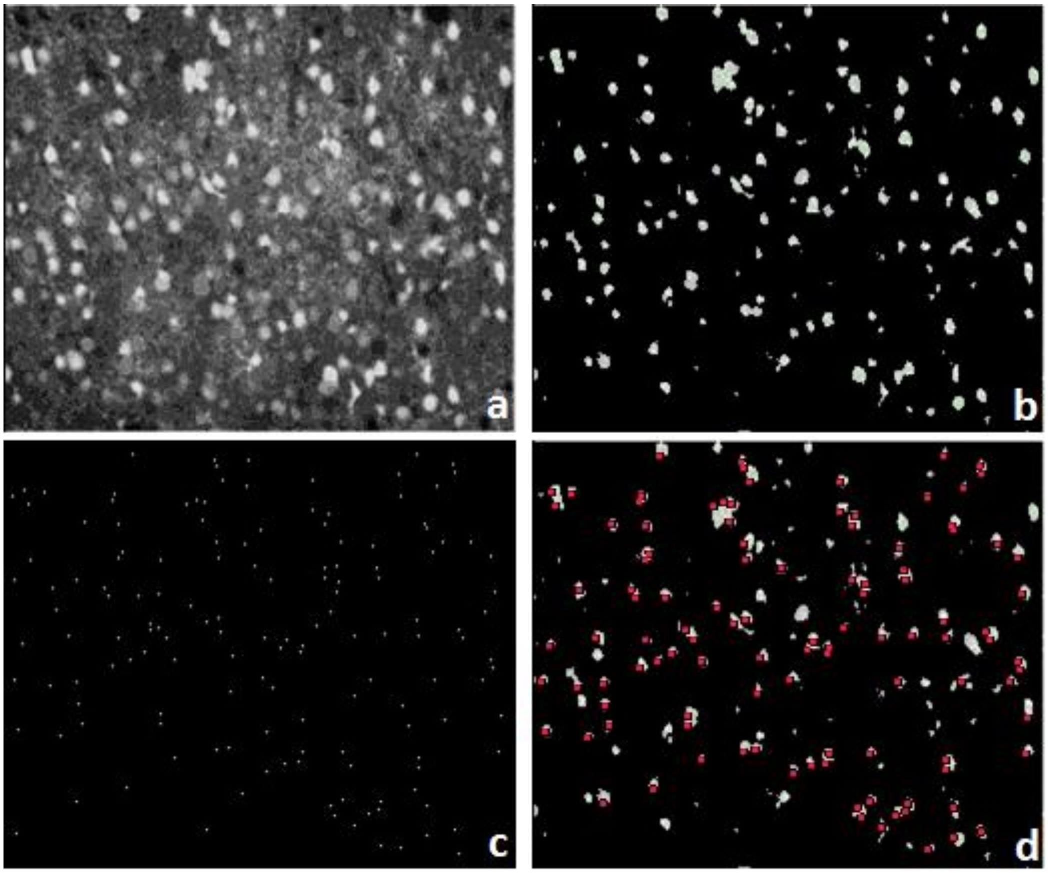

Fig. 36 Pocketscope SW automated cell body detection method (a) A brightfield image of neurons in a brain slice that have been loaded for calcium imaging (b) The image of the brain slice after threshold conditions have been applied (c) Locations of local peaks that are greater than the surrounding 5x5 pixels. (d) An overlay of the image with the threshold applied, and identified cell body locations noted in red.

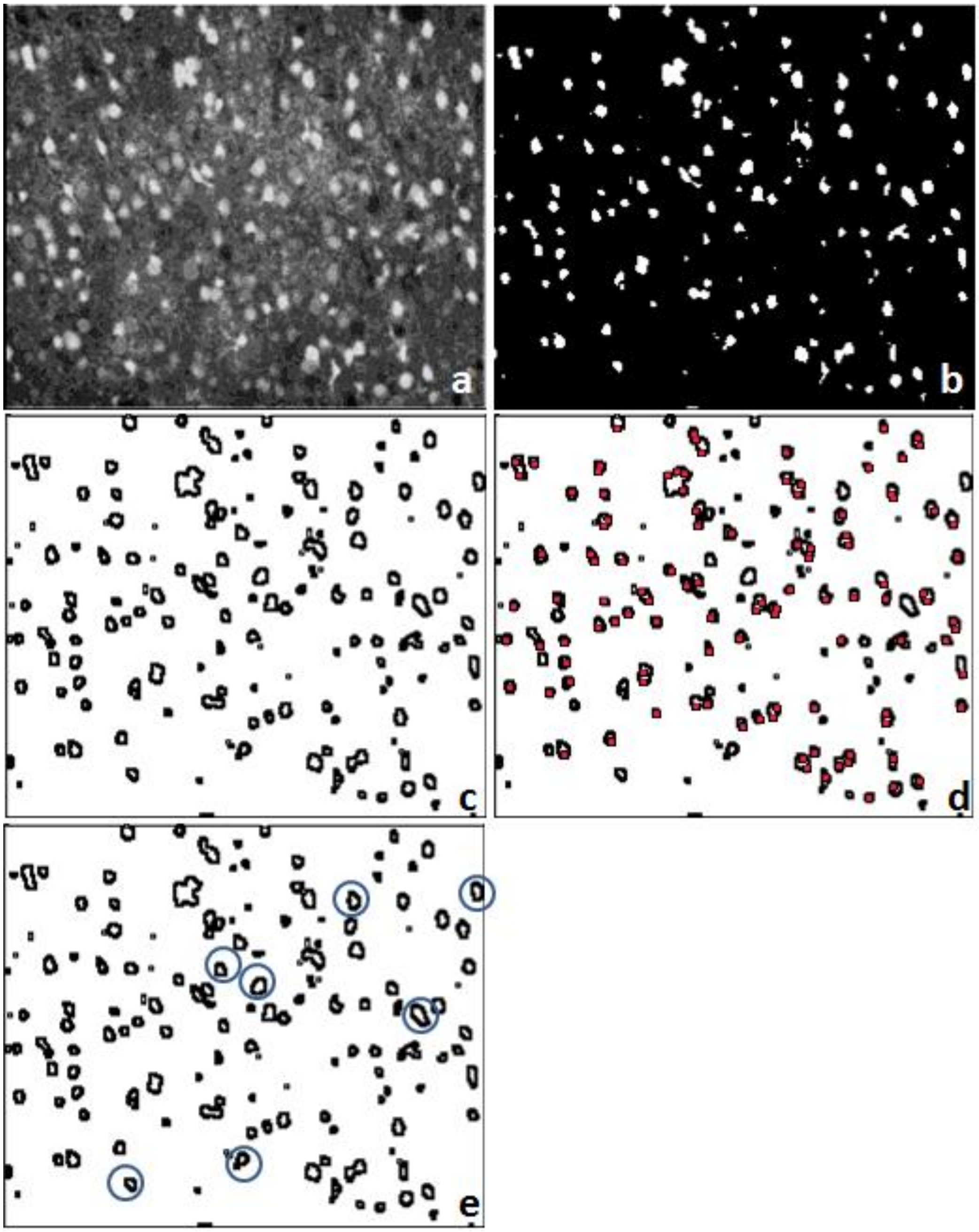

Fig. 37 Cell body detection with Image J (a) brightfield image of a brain slice loaded with calcium indicators. (b) applying threshold conditions (c) edge detection (d) overlay of detected edges with Image J, and detected cell bodies using the algorithm developed for the Pocketscope (e) 7 of 109 cell bodies that the Pocketscope software failed to note the presence of.

After the cell locations are identified, the positions of detected cells are denoted with white circles that are superimposed with the camera output, as shown in Fig. 38. One cell is denoted with a red circle that corresponds to the currently selected location in the “Soma Locations” listbox. This enables targeted locations to be shifted in x, y, z; and the intensity of a given target to be adjusted with respect to the other targeted cells. Holograms to target the cell bodies are automatically computed making use of the graphics processing unit for sub-millisecond computations as will be presented in the chapter to follow. An example of fluorescence as a result of targeting 43 10 µm fluorescent beads suspended in glue is shown in Fig. 39. Some beads are slightly out of focus due to the limited depth of field of the 2D imaging system used in this example.

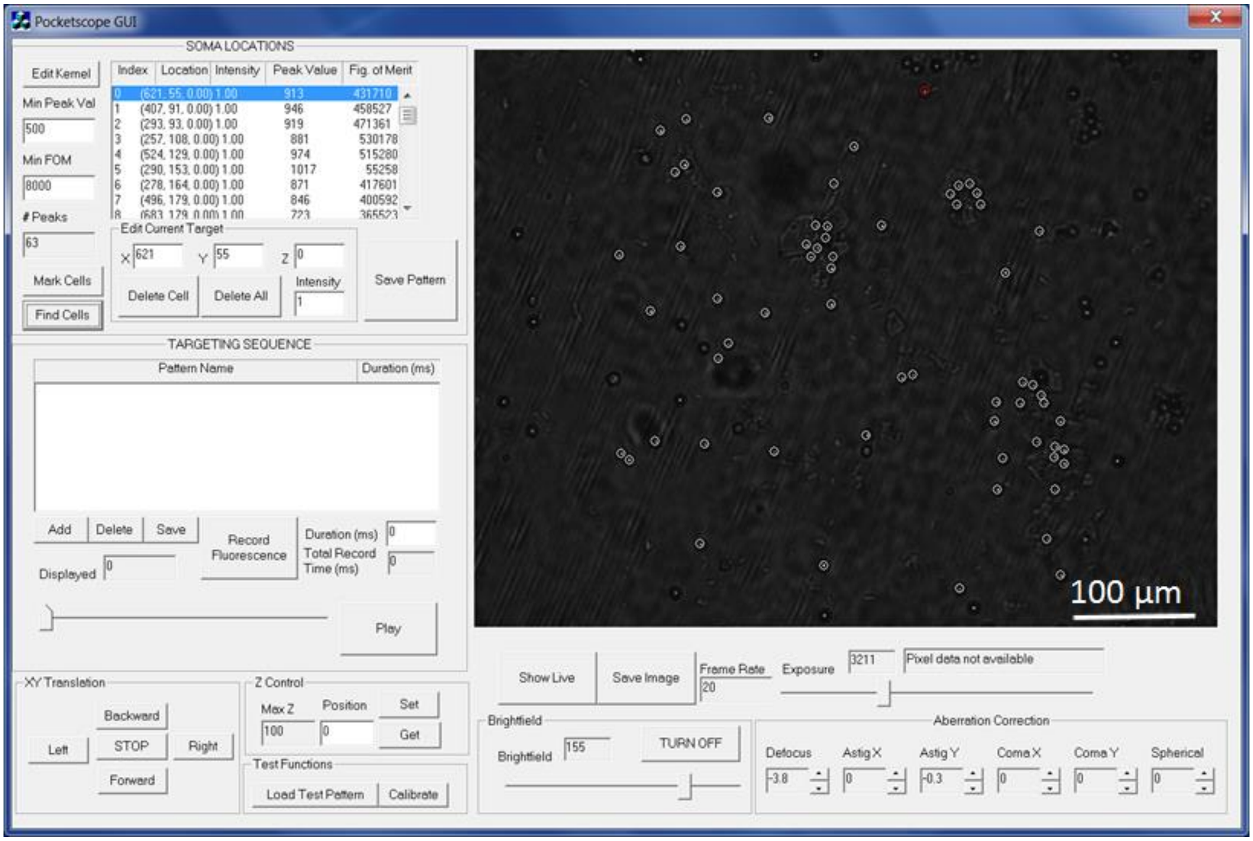
Pocketscope GUI
SOMA LOCATIONS
Edit Kernel
Mark Cells
Find Cells
Edit Current Target
Delete Cell
Delete All
Save Pattern
TARGETING SEQUENCE
Add
Delete
Save
Record Fluorescence
Play
XY Translation
Backward
Left
STOP
Right
Forward
Z Control
Set
Get
Test Functions
Load Test Pattern
Calibrate
100 µm
Show Live
Save Image
Brightfield
TURN OFF
Aberration Correction

Index	Location	Intensity	Peak Value	Fig. of Merit
0	(621, 55, 0.00)	1.00	913	431710
1	(407, 91, 0.00)	1.00	946	458527
2	(293, 93, 0.00)	1.00	919	471361
3	(257, 108, 0.00)	1.00	881	530178
4	(524, 129, 0.00)	1.00	974	515280
5	(290, 153, 0.00)	1.00	1017	55258
6	(278, 164, 0.00)	1.00	871	417601
7	(496, 179, 0.00)	1.00	846	400592
8	(683, 179, 0.00)	1.00	723	365523

Min Peak Val 500
Min FOM 8000
Peaks 63
X 621 Y 55 Z 0
Intensity 1

Pattern Name	Duration (ms)

Duration (ms) 0
Total Record Time (ms) 0
Displayed 0
Max Z 100
Position 0
Frame Rate 20
Exposure 3211
Pixel data not available
Brightfield 155
Defocus -3.8
Astig X 0
Astig Y -0.3
Coma X 0
Coma Y 0
Spherical 0

Fig. 38 The bead locations are auto-detected, and indicated with white circles. The currently selected bead from the “Soma Locations” listbox is shown in red.

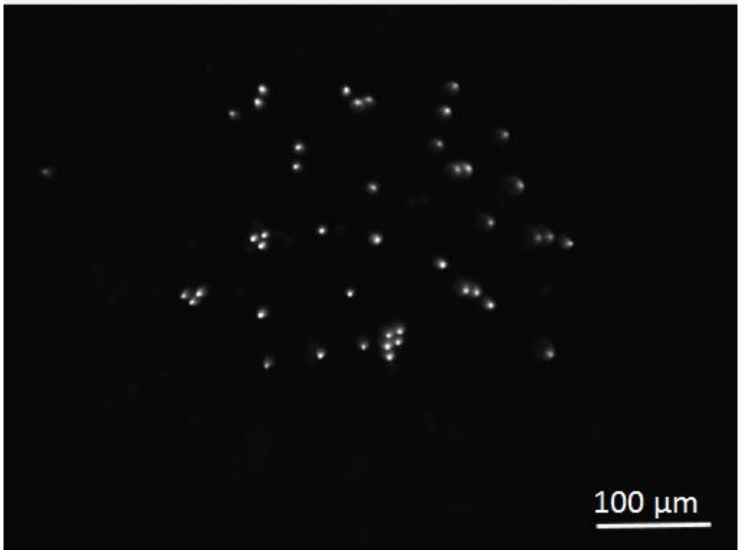

Fig. 39 Fluorescence as a result of targeting 10 um silica beads. Not all the beads are in focus because the cubic phase mask is not in use in this example.

Use of the software requires the ability to map coordinates on the screen to targeted locations within the sample. This is calibrated using the affine transformation. A series of three holograms are loaded to the SLM steering a single spot to a position within the field of view. By manually selecting the locations of the focal points the affine transformation is utilized to map the location of mouse clicks to locations of targeted excitation on the SLM.

6.3 Arbitrary spatio-temporal targeting

After a series of target patterns have been generated, arbitrary spatio-temporal targeting can be defined by loading a sequence of target patterns, that can be displayed on the SLM in increments of the camera frame rate. After the desired targeting sequence is defined, the software will initiate the loop, and will store the camera data in a pre-allocated buffer that is capable of storing up to 5 minutes of data. After the fluorescence signals have been recorded all the data corresponding to the test is saved including: the target x,y,z locations and intensity settings for each focal point of each hologram used in the sequence, the holograms used, the raw images from the recording for later processing if desired, and intensity measurements from each targeted locations as a function of time.

7 Maximizing beamsteering efficiency of computer generated holograms

SLMs are potentially powerful tools for optogenetics research, enabling the user to selectively and efficiently redirect incident illumination to focal points within a 3D volume. However, when applied to neuroscience, it is critical to maintain precise control over the redirection of light. If significant light is lost to the 0th order, or if light is lost to ghost orders as shown in Fig. 40, then this could damage the sample, or influence measurements of the neural network one is trying to probe and manipulate. Because the compounds used for photostimulation and calcium imaging are designed to be highly sensitive, capable of responding to intensities as little as 8 mW/mm^2 [89], even small variations in ghost orders and the 0th order can influence a measurement. Additionally, if there is significant variation in the intensity of 1st order focal points across the field of view, then cells with activity could fail to fluoresce in calcium imaging experiments and focal points could fail to stimulate action potentials uniformly along neural circuit. This could lead to incorrect conclusions about interconnectivity of neurons. For these reasons, the precision required for the redirection of light within a 3D volume is far more demanding for optogenetics than for holographic optical tweezers where a ghost trap is unlikely to significantly interfere with the ability to execute an experiment. Thus, for optogenetics, much more attention must be paid to the efficiency of beamsteering, and to the methods used to compute holograms.

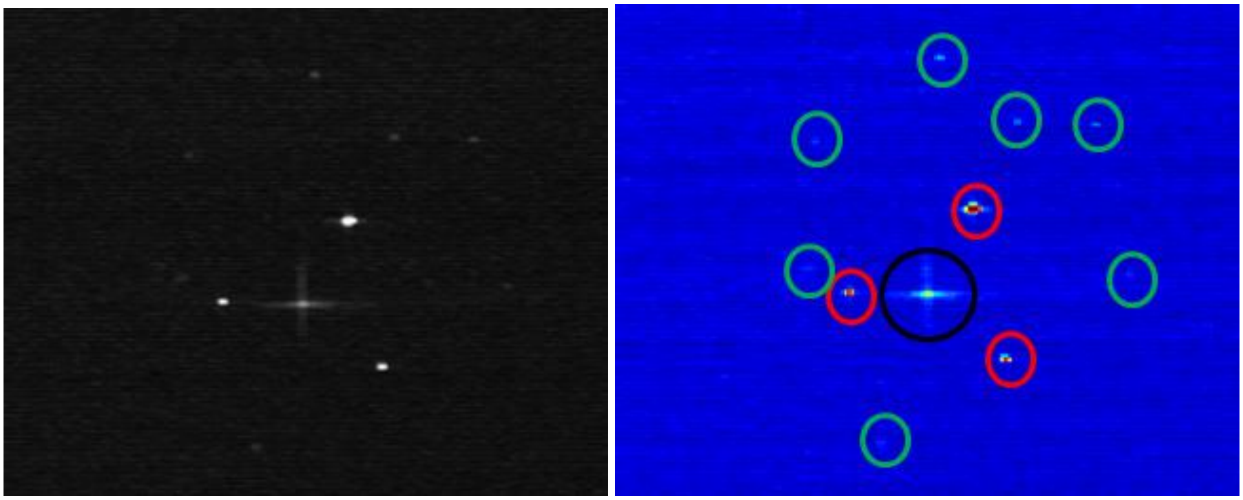

Fig. 40 Image of the Fourier plane taken when an SLM is used to apply a hologram. The hologram is designed to produce three focal points with a weighting function applied such that the intensity of two focal points should be approximately equal, and the third focal point should be 10x brighter. Ideally the 0th order would not be visible, and there would be no ghost orders. (left) the raw camera data (right) false color to highlight the locations of the desired focal points which are noted in red circles, the ghost orders which are noted with green circles, and the 0th order which is noted with a black circle.

In the work presented in this chapter, two methods are developed to maximize beamsteering efficiency. First, the algorithm used to compute holograms in the first half of this thesis, Lenses and Gratings, is replaced with a 3D Weighted Gerchberg Saxton (WGS) [93]. The WGS sacrifices speed and computational ease in favor of improving first order uniformity. Second, intensive calibration efforts are utilized to accurately and regionally map the phase response of the SLM to voltage. In this chapter, the effects of assuming a regionally invariant phase response across the active area of the SLM are quantified. This is a common assumption that is shown here to degrade beamsteering efficiency.

The 3D Weighted Gerchberg Saxton is an iterative technique that is shown here to converge to 90% uniformity within 10 iterations. An example distribution of spot intensities for a 512 x 512 pixel hologram producing 25 spots is shown in Fig. 41(top), and a corresponding plot of uniformity as a function of number of iterations, as defined by Di Leonardo [93] is shown in Fig. 41(bottom). In collaboration with Martin Persson at Gothenburg University, Martin and I implemented the algorithm on the graphics processing unit to minimize computation time. The result is that a 512 x 512 pixel hologram can be computed in less than 1 ms per iteration. The core of the software is available as freeware [94].

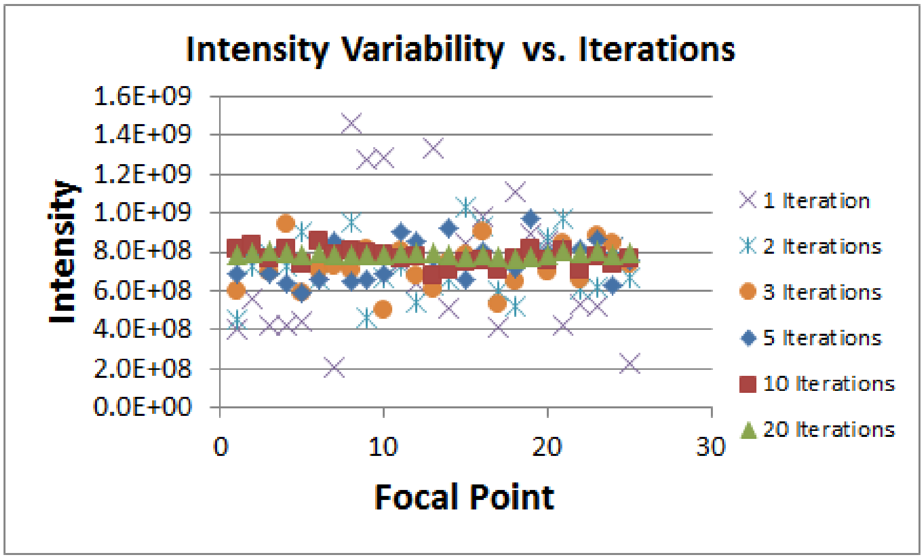

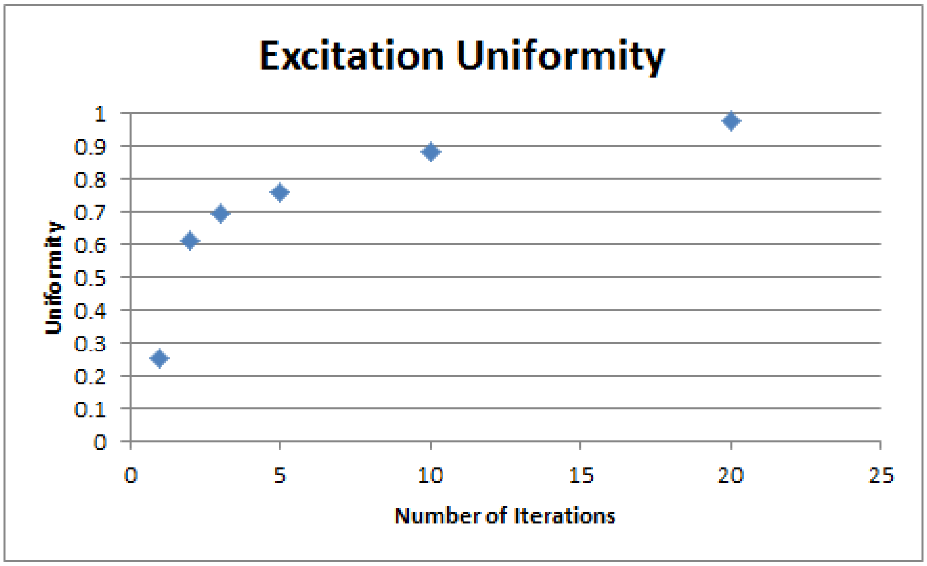

Fig. 41 (top) Plot of 1st order intensity for 25 spots, shown as the software iterates up to 20 times to compute the hologram. (bottom) Plot of uniformity as a function of number of iterations. Within 10 iterations uniformity is generally 90% or greater.

7.1 SLM Calibration

Ideally, SLMs would provide a spatially uniform phase response to uniformly applied input voltage, thus eliminating the need for regional calibrations. However, backplane topography from the polishing process, non-uniformities in deposition of mirrors, and variations in uniformity in the liquid crystal layer introduced during the build process all lead to a spatially varying phase response. Furthermore, the drive scheme used to DC balance the liquid crystal can greatly impact the uniformity.

In Fig. 42a and Fig. 43a, plots are shown of typical phase response curves of an SLM as a function of input grayscale value. The two plots differ depending on the DC balancing drive scheme. DC balancing is required because Nematic LC contains impurities. The impurities begin to drift when a DC voltage is applied across the LC and can form a space charge layer. Because these impurities have a charge, a back EMF will result when the space charge layer is formed. This back EMF will cause the switching characteristics of the liquid crystal to change. Thus, to keep the impurities from drifting it is necessary to toggle the voltage applied to the pixel with time.

The preferred drive scheme is shown in Fig. 42. In this case, the coverglass of the SLM is held at a constant voltage of 2.5 volts (or gray level of 127 given 8 bit drive electronics) as is shown in red. The voltage applied to the pixel toggles at a rate of 1 kHz between the programmed value *A* (*A*=63 on blue trace or *A*=21 on green trace) and the inverse value *A′* = (255-A). As a result, the field across the LC material at any given moment is the difference between the cover glass voltage and the pixel voltage. As a result, using a passive cover glass drive scheme, the maximum electric field across the LC layer is 2.5 V. Because Nematic LC responds to the amplitude of the drive signal and not the sign there is a symmetric phase response about grayscale 128.

If the 2.5 V field is found to be limiting, then the coverglass can be actively driven with a square wave as is shown in Fig. 43. The voltage at the pixel is still toggled with time at the same rate, but depending on the value written to the pixel, the pixel voltage is either in-phase or out-of-phase with the coverglass. As a result, the full 5 V field is available and the phase response is no longer symmetric. The problem with this drive scheme is that it takes time to update the voltage on all the pixels of the backplane, but the voltage update of the coverglass, which is essentially a single pixel, is fast. This time difference introduces a voltage skew across the SLM. The timing is implemented such that the coverglass voltage is updated at the same time as the pixels in the middle of the SLM are loaded, thus distributing the skew.

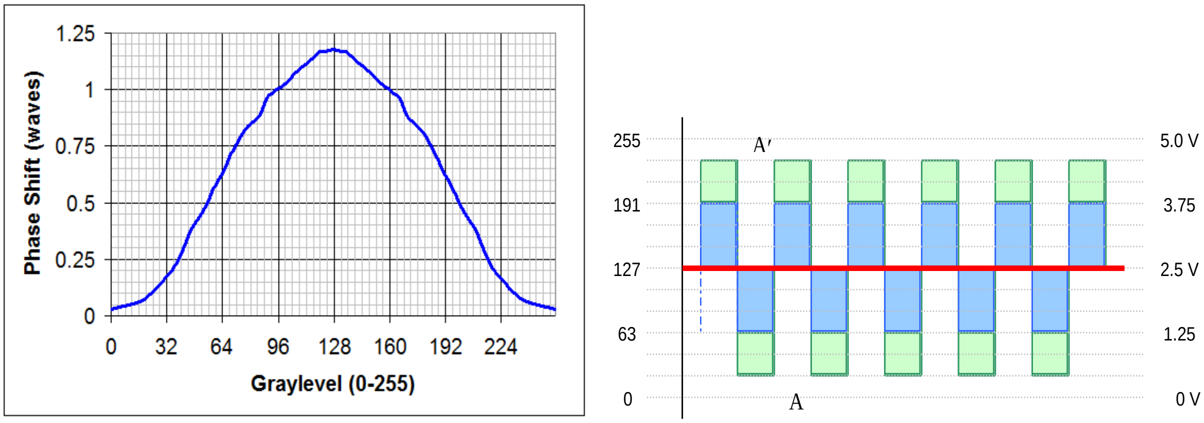

Fig. 42 (a) Typical phase response of an SLM as the voltage applied to the pixels is varied. This with a passive coverglass drive scheme. (b) DC balancing drive scheme for a passive coverglass SLM

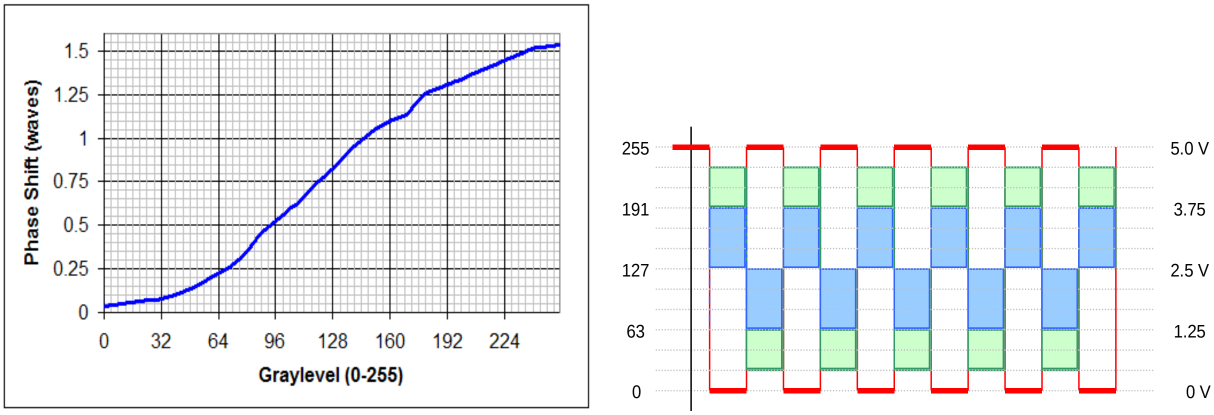

Fig. 43 (a) Typical phase response of an SLM as the voltage applied to the pixels is varied. This with an active coverglass drive scheme. (b) DC balancing drive scheme for an active coverglass SLM

In order to calibrate the nonlinear optical response of the LC to voltage, a diffractive method is developed here. The SLM is divided into 16 regions, as shown in Fig. 44. In one region, a checkerboard pattern with a period of 4 pixels is applied to the SLM, while the remaining regions are held at a constant voltage. Use of a high frequency checkerboard pattern enables the calibration to take into account the extra voltage required to overcome inter-pixel cross talk, whose effects are more noticeable when high frequency patterns such as holograms are considered. In the calibration routine the voltage applied to the pixels that are white is held constant at 5 V, and the pixels that are varied experience a time dependent voltage that decrements from 5 V down to 0 V. By monitoring the intensity of the first order in the Fourier plane while varying the voltage applied to the pixels (and thus the phase shift between the pixels) a mapping of input grayscale to output phase shift can be established.

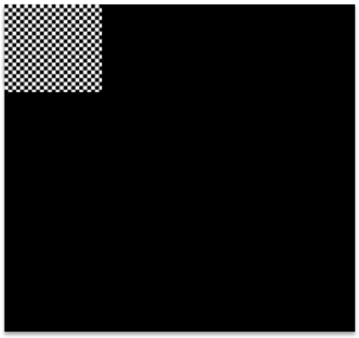

Fig. 44 Pattern written to the SLM during calibration. The SLM is divided into 16 subsections. A checkerboard pattern is written to one section, while the rest of the SLM is held blank. A series of 256 images are loaded to the SLM during calibration of each region. One check is held at a constant value of 255, while the other check value is decremented from 255 to 0. As the series of patterns are loaded to the SLM, the intensity of the 1st order is measured. The process is repeated for each of the 16 regions of the SLM.

Fig. 45 shows a simulation of the intensity pattern in the Fourier plane when writing a series of checkerboard patterns to the SLM. This is used to generate a look up table (LUT) that remaps input 0 – 255 to an output grayscale data set that results in a linear 0 – 2π phase shift, and to quantify the phase error and expected impact on beamsteering efficiency when a uniform phase response is assumed.

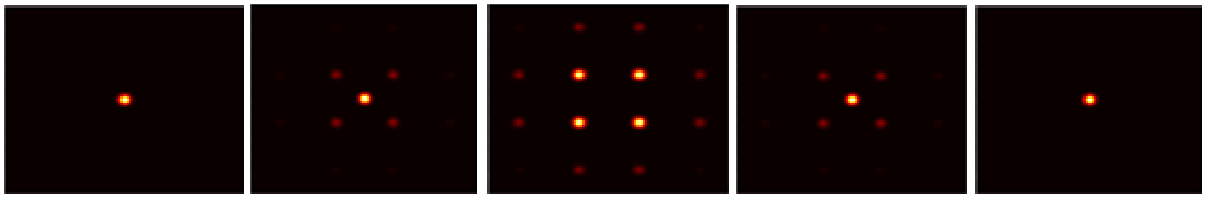

Phase = 0, 0 Phase = 0, π/2 Phase = 0, π Phase = 0, 3π/2 Phase = 0, 2π

Fig. 45 Intensity of the Fourier plane when checkerboard patterns of varying phase are written to the SLM.

The raw intensity measurements of the 1st order are shown in Fig. 46 for an SLM designed to be used with an active coverglass drive scheme, and a passive coverglass drive scheme. In the two figures corresponding to the two drive schemes there are 17 traces. The first 16 traces correspond to the intensity of the 1st order when testing each of the 16 sub-sections of the SLM. The 17th trace corresponds to the intensity of the 1st order when a checkerboard pattern is written to the entire SLM. The intensity of this trace is notably higher than that of the subsections. Because more light is re-directed to the first order when the entire SLM is analyzed as a single region, the detector saturates, necessitating a decrease in the detector gain. Due to the difference in gain between regional and global calibrations, one should not draw conclusions about the intensity of the subsections as compared to the entire SLM. However, the shapes can be compared, which provides information about the regional phase response of the SLM, and the extent to which regions vary from the global response.

In order to convert the 1st order measurements to phase, the raw measurements must be scaled to range from 0 to 1, as shown in Fig. 47. Equations 6 and 7 can be used to map scaled intensity measurements to phase. In order to compensate for noise in the measurements, particularly near the 0, π, and 2π points, the raw phase data is fit to a 5th order polynomial using the GNU Scientific Library. From this the curve fit, a regional look up table can generated such that input 0 to 255 results in a linear increase in phase delay from 0 to 2π. The process is repeated for each of the 16 regions in the SLM, and for the entire SLM as a single region. The phase curves can be used to define error bars of the maximum error across each of the 16 regions for each graylevel if a global calibration is used as opposed to a regional LUT. This is shown in Fig. 48.

$$Phase = 2 * \mathrm{asin}(\sqrt{Intensity}) \qquad \text{(Phase} < \pi\text{, measuring 1}^{\text{st}}\text{ order)} \qquad \text{Eq. 6}$$

$$Phase = 2 * [\pi - \mathrm{asin}(\sqrt{Intensity}] \qquad \text{(Phase} > \pi\text{, measuring 1}^{\text{st}}\text{ order)} \qquad \text{Eq. 7}$$

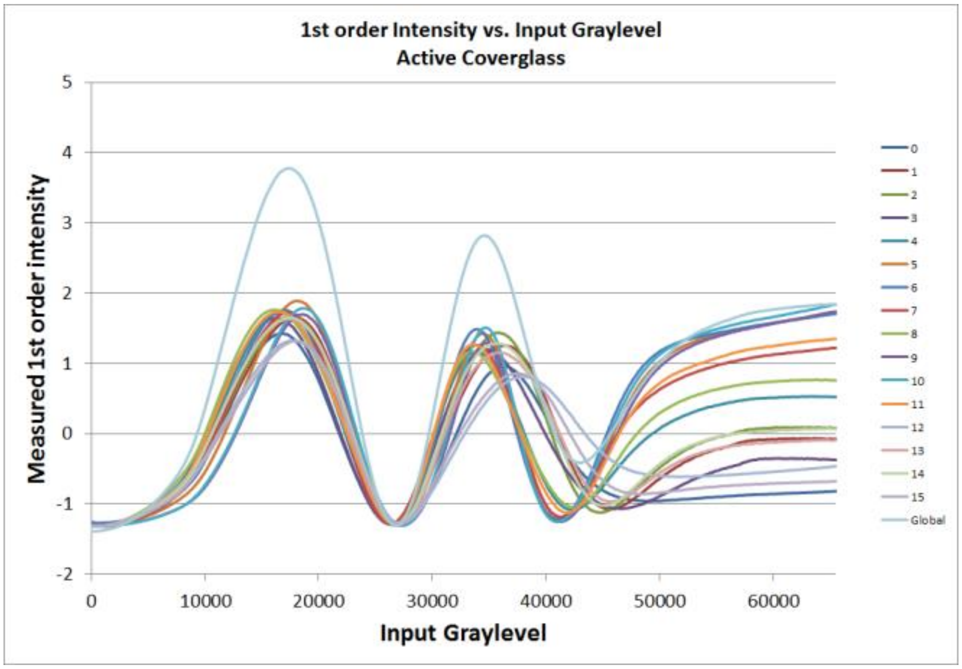

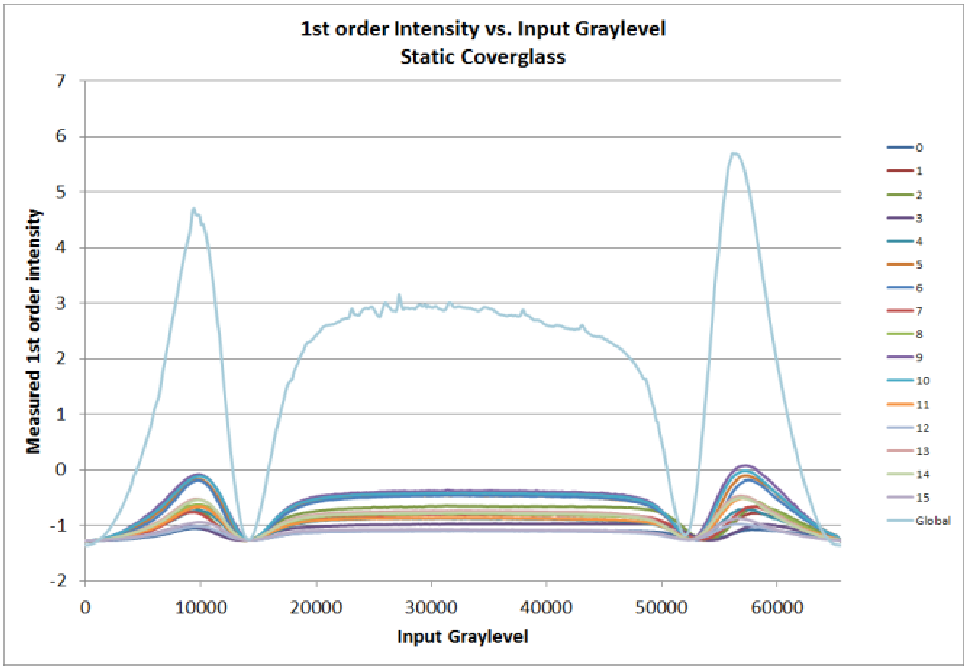

Fig. 46 Measurements of 1st order intensity vs grayscale for 16 regions of the SLM, and for the SLM as a single region.

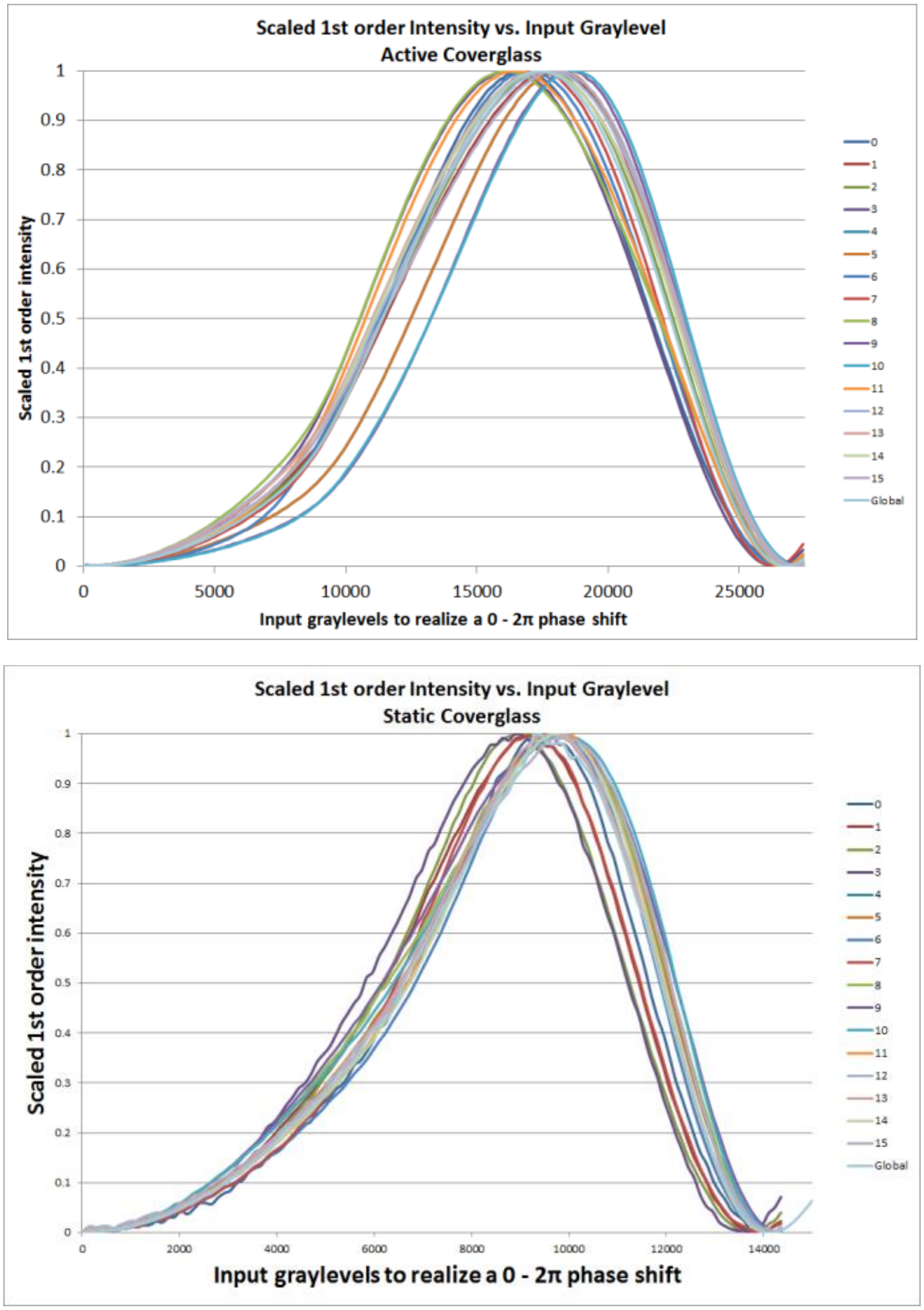

Fig. 47 Scaled measurements of 1st order intensity vs. grayscale for 16 regions of the SLM, and for the SLM as a single region. Measurements are only shown for the first wave of modulation.

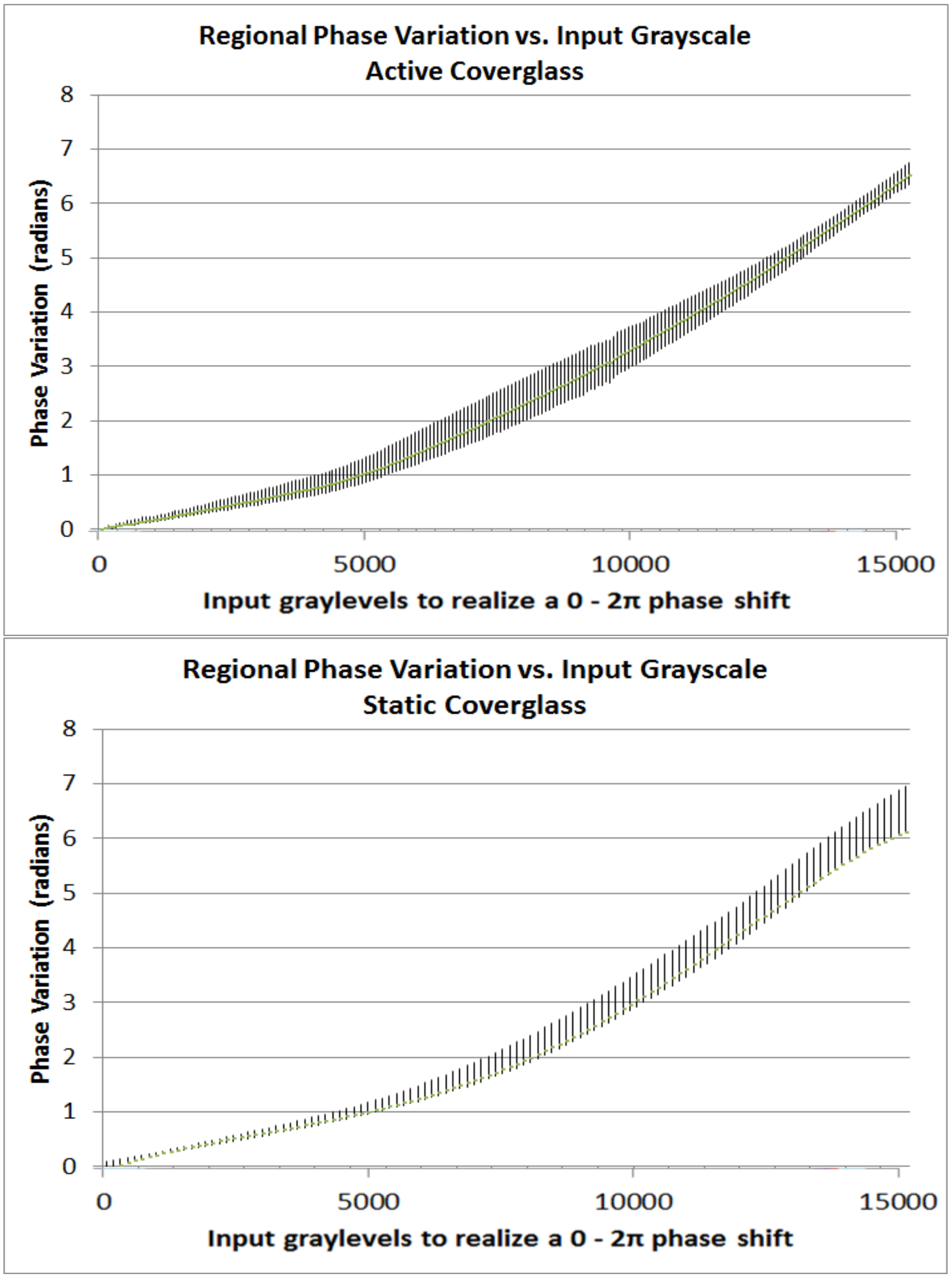

Fig. 48 Regional variability in phase shift when considering 16 regions of the SLM

If it is assumed that the phase response is uniform, then this leads to a regionally dependent phase error causing a reduced intensity of desired 1st order focal points, and increase the intensity of the 0th order. To quantify this effect, and isolate the effect from other possible sources of error that can lead to inefficient beamsteering, a simulation is utilized. First, an ideal hologram that is used to produce 3 focal points is computed. A secondary hologram is computed that is identical to the first hologram, but includes regional phase errors that are introduced when a uniform phase response is assumed. The phase error presented here is based on measurements of Fig. 48 (right). The result of adding phase error shifts the regional tilt of the hologram, and the location of 2π wraps as shown in Fig 49. By assuming a Gaussian incident wavefront, and Fourier transforming the two holograms, it is possible to quantify the change in 0th and 1st order intensity. For this example of a hologram that is designed to produce 3 focal points, the phase error leads to a decrease in 1st order intensity of 2.72%, 2.76%, and 2.73% at each focal point, and a 16.85x increase in the 0th order intensity.

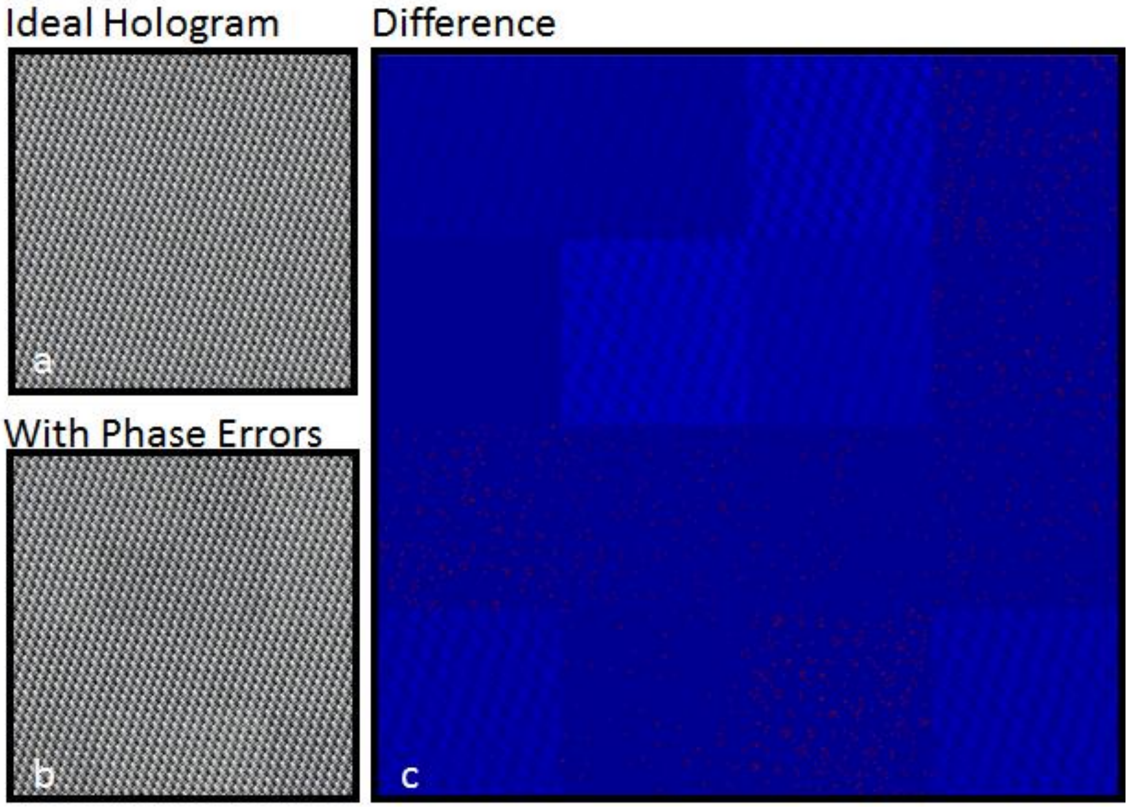

Fig 49 (a) Ideal hologram to produce 3 focal points. (b) Modified version of the hologram where phase errors were introduced based on measurements of the regional phase response. (c) the difference between the two holograms.

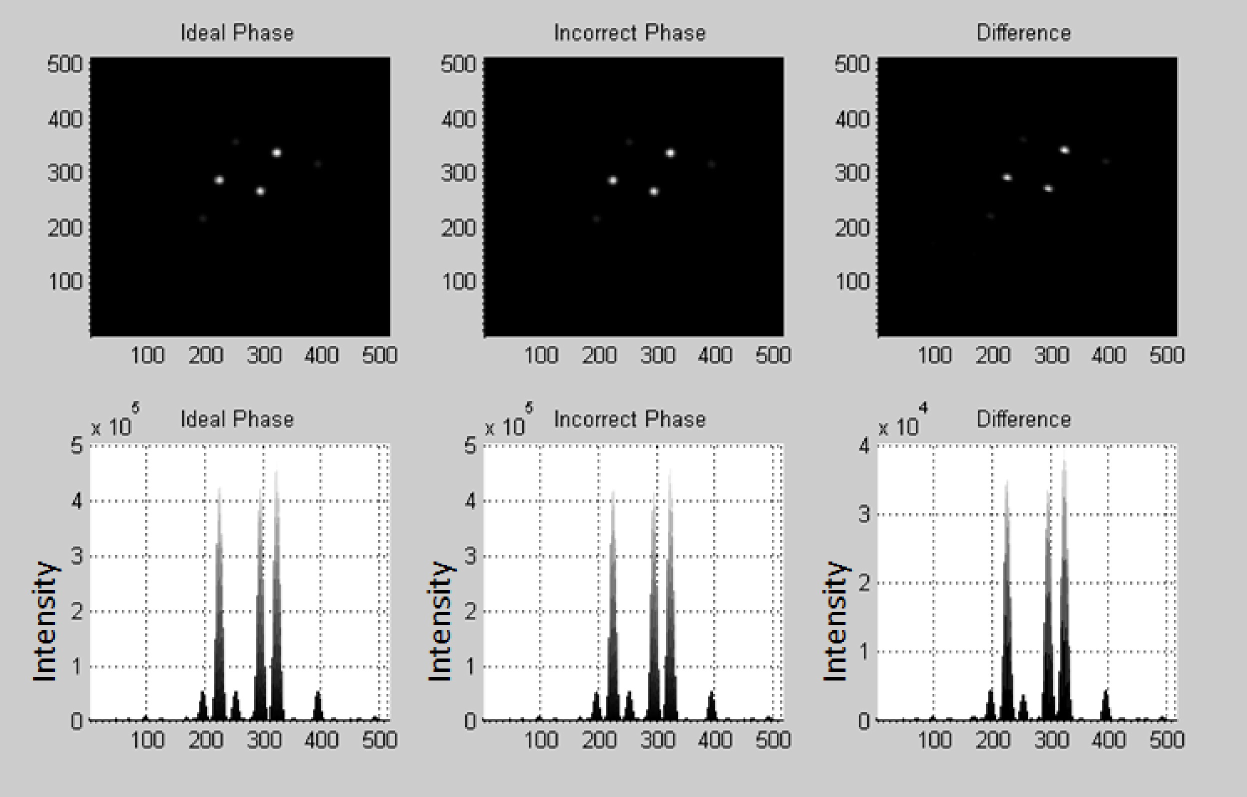

Fig 50 (top) Fourier transform of the ideal hologram, the Fourier transform of the hologram with phase error due to assuming an invariant phase response, and the difference between the Fourier Transform of the two images. (bottom) Plot of the intensity of the desired focal points, and the unwanted ghost orders for an ideal hologram, a hologram with phase error, and the difference in intensity between the two. When a uniform phase response is assumed, the resulting phase error results in a decrease in 1st order intensity of 2.72%, 2.76%, and 2.73% at each focal point, and a 16.85x increase in the 0th order intensity.

7.2 Conclusions

In order to harness the potential for SLMs to selectively and efficiently redirect incident illumination to focal points within a 3D volume for optogenetics research, it is critical to maintain precise control over the phase of wavefronts. In this work, the phase response of the SLM is found to be regionally variable. If the phase response is assumed to be invariant, then the resulting phase error for the SLM tested will vary up to 0.15 waves. This error used in combination with this example hologram resulted in a reduction in 1st order beamsteering efficiency 2.72%, 2.76%, and 2.73% at each focal point, and a 16.85x increase in the 0th order intensity. When considering highly sensitive calcium indicators and opsins for photostimulation, this error could be sufficient to alter measurements of activity in neural circuits.

8 Using the Pocketscope For Calcium Imaging

8.1 Materials and Methods

The preparation procedure, as documented in this section, was supplied by Prof. Yuste at Columbia University. All animal handling and experimentation were performed according to NIH and local IACUUC guidelines. We prepared 400 um thick coronal neocortical slices in mouse primary visual cortex from postnatal day 14 C57/BL6 (GeneTex , GTX85913) with a vibratome (Leica VT1200) in ice-cold oxygenated modified artificial cerebro-spinal fluid (ACSF Tocris Bioscience, 3525/25ML) that included 1 mM $CaCl_2$ and 3 mM $MgSO_4$, in which NaCl was replaced by an equimolar concentration of sucrose (in mM): 27 $NaHCO_3$, 1.5 NaH_2 PO_4, 222 sucrose, 2.6 KCl. We then placed the slices in oxygenated standard ACSF at 37 °C for 30 min. For AM dye loading, we deposited the slices onto the bottom of a small Petri dish (35mm in diameter) filled with 2 ml of ACSF, ventilated with 95% O_2 /5% CO_2 and placed in a slide warmer at 37 °C (Fisher Scientific). The dye solution is prepared by adding 48 µl DMSO and 2 ul Pluronic F-127 (10% solution in DMSO, P-6866, Molecular Probes) into a tube of 50 µg Oregon green 488 BAPTA-1 AM (O-6807, special package, Molecular Probes). Thus, the dye solution finally contains 0.1% (1 mM) AM-ester dye and 0.4% Pluronic F-127 in DMSO. A small amount of the dye solution is first pipetted directly over the slice so that the slice is initially exposed to a high concentration of the AM dye, and the remainder ejected into the petri dish. The loading is terminated by transferring the slices into fresh ACSF. The slices are maintained at room temperature for at least 30 min before imaging. During imaging, the slices are kept in an oxygenated bath of normal ACSF.

8.2 Imaging Neurons in Brain Slices

In the design of the imaging system presented in Chapter 6, a 635 µm x 470 µm region of the sample is imaged to a 1024 x 768 pixel camera. This results in each pixel imaging 0.6 µm of the sample, which is sufficient for imaging a low concentration of 10 µm fluorescent beads suspended in glue, as it is a highly transparent sample. However, for imaging neurons in brain slices that are highly scattering, it is challenging to identify the locations of cell bodies with an average of 16x16 pixels per cell. Thus, for work with brains slices, the image relay system is modified such that the field of view is 160 µm x 210 µm . An example brightfield image of a brain slice is shown in Fig. 51. This is an image of layer 5 in mouse primary visual cortex, imaging a plane approximately 20 µm into the sample. Imaging neurons one cell layer into the thickness of the sample increases scattering, making it more challenging to see cell bodies. However, cells at the top surface of the slice exhibit low viability.

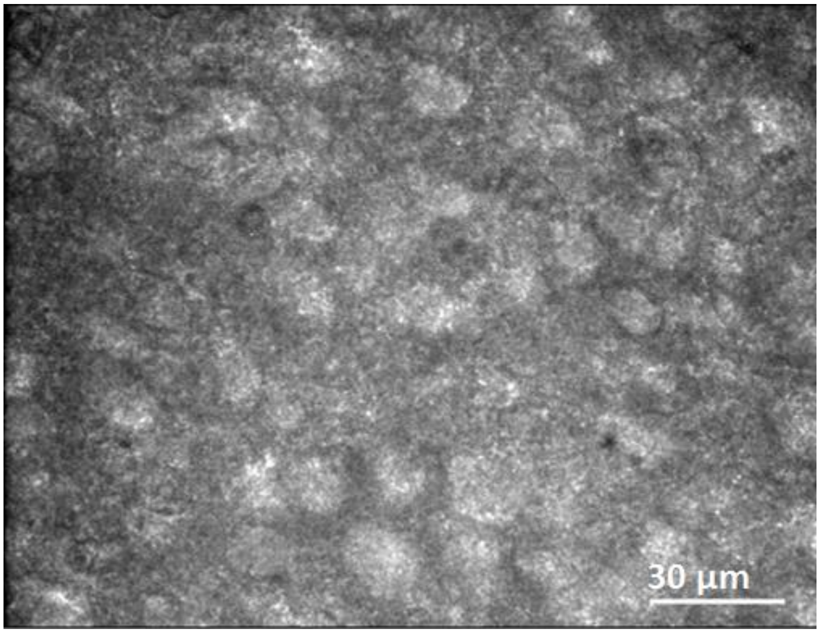

Fig. 51 Brightfield image of a brain slice taken in the Pocketscope. The image is from L5 in mouse primary visual cortex, 20 µm below the top of the 400 µm slice.

8.3 Fluorescence signals

A series of 10 calcium imaging experiments were run over the span of an hour. In each experiment 15 to 25 cells were targeted, and fluorescent activity was recorded at a rate of 20 fps for a duration of 30 seconds. Typical results are shown in Fig. 52 and Fig. 53. In the plots showing fluorescent spikes with a high intensity and long duration, the cell experienced a burst of activity containing many action potentials. Synchronous events between multiple cells are shown in the two figures. This does not necessarily mean that the cells are interconnected; however, it is an indicator that the cells warrant further investigation. Fluorescent spikes with a low intensity, and short duration were also recorded. This indicates that fewer action potentials occurred during the bursts.

Given fluorescence traces from imaged neurons, it is desirable to make statements about the number of action potentials that occurred during the fluorescence spike. A number of algorithms have been developed to accomplish this based on thresholding [95] template matching [96], linear deconvolution [97, 98], and fast non-negatively constrained optimization methods [99]. Most of these approaches either explicitly or implicitly assume a model relating bursts of action potentials to the fluorescence observations. For example, one can assume that a spike train is convolved with a filter, such as an exponential [100]. It is desirable to validate the model used in the instrument through simultaneous use of a patch clamp and calcium imaging. For this project, combining the two technologies remains a topic of future research.

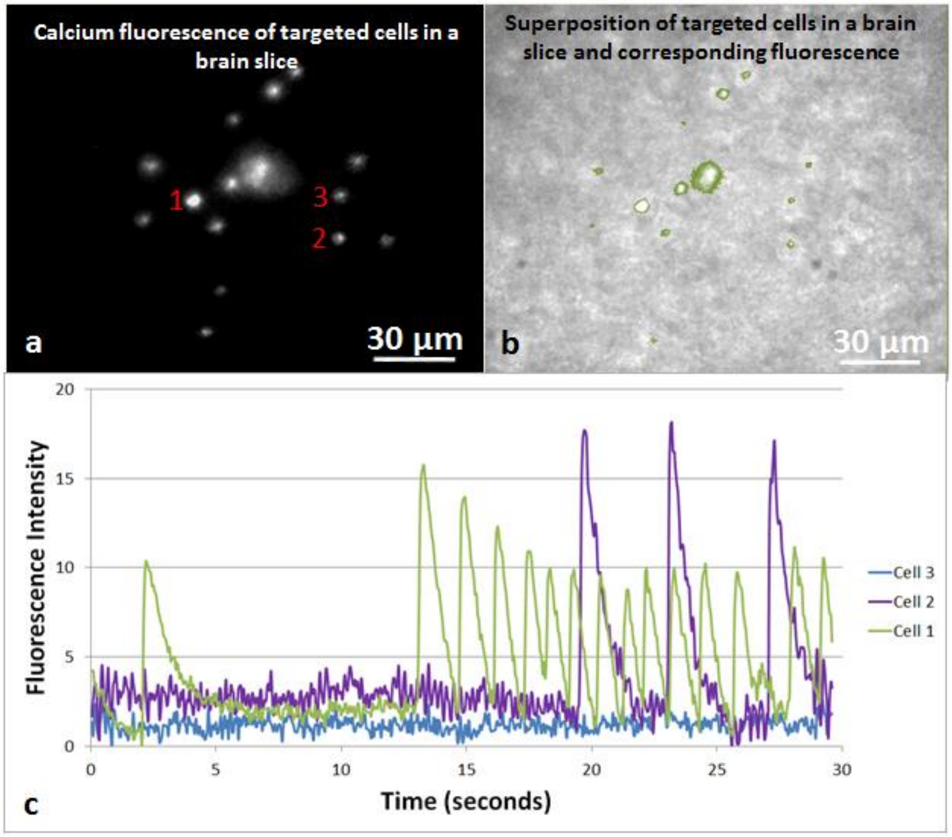

Fig. 52 Calcium imaging with brain slices in the Pocketscope. (a) A fluorescence image of a single time slice in the 30 second recording taken while targeting 15 cells. Fluorescence activity with respect to time is plotted for 3 cells in the sample. The cells of interest are denoted with red numbers directly to the left of the cell. (b) an overlay of fluorescence with a brightfield image of the targeted cells. (c) a recording of fluorescence activity with respect to time for 3 cells in the sample. Cell 1 was highly active, having 15 bursts of action potentials in the 30 second recording. Cell 2 had one synchronous event with Cell 1. For a reference of the noise level, cell 3 exhibits no activity during the recording window.

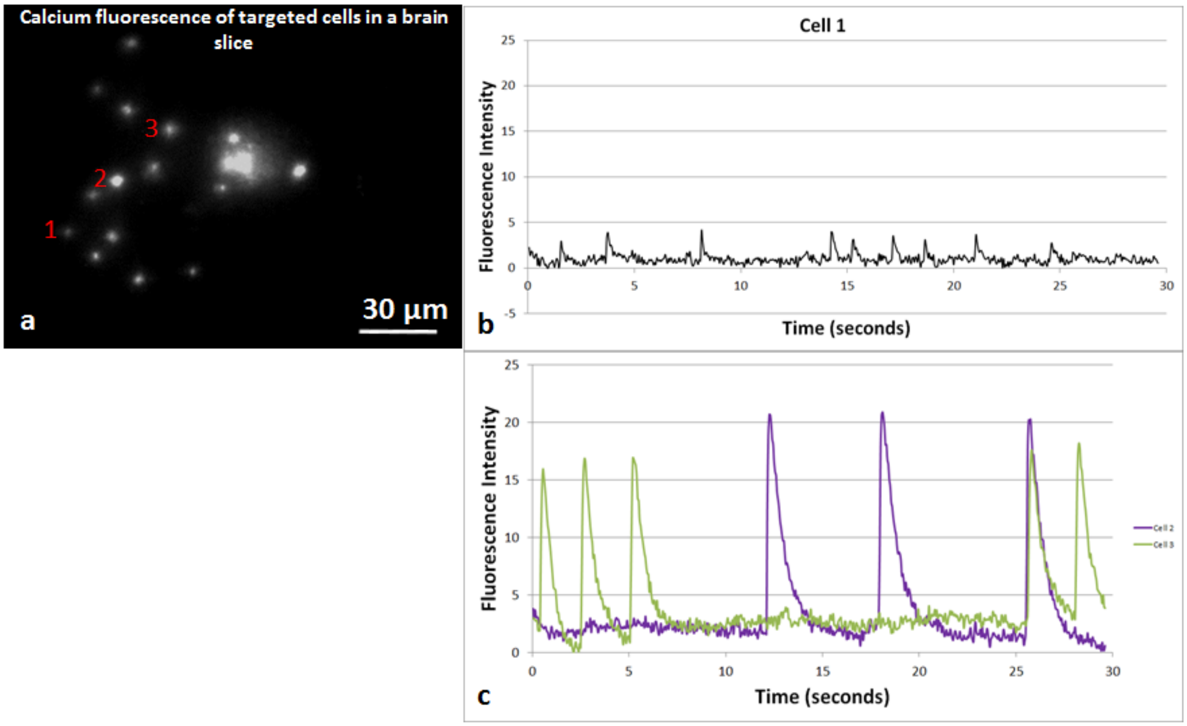

Fig. 53 Calcium imaging with brain slices in the Pocketscope. (a) A fluorescence image of a single time slice in the 30 second recording taken while targeting 15 cells. Fluorescence activity with respect to time is plotted for 3 cells in the sample. The cells of interest are denoted with red numbers directly to the left of the cell. (b) Recorded fluorescence with respect to time for one cell. The reduced intensity and duration of activity indicates fewer action potentials in the bursts of activity. (c) A recording of fluorescence activity with respect to time for 2 cells in the sample, again capturing synchronous activity between two cells.

8.4 Conclusions

This work demonstrates use of an epi-fluorescence NLC SLM based microscope that is capable of targeting light within a 3D volume for experiments with calcium imaging and photostimulation. The microscope is compatible with extended depth of field imaging techniques, enabling the tool to map interconnectivity of neural circuits in brain slices, which is by nature a 3D problem. Use of the tool was demonstrated for calcium imaging of populations of 15 to 25 cells. The tool was sufficiently sensitive to record synchronous activity between multiple cells, and activity containing large and small bursts of action potentials. The tool is capable of creating arbitrary spatio-temporal excitation patterns, enabling more complex studies of circuit activity. For example, research is showing that neural circuits fire in predictable repeating patterns. Using the Pocketscope, one can use a combination of photostimulation and calcium imaging to perturb firing patterns and monitor the response of the circuit. This compact design is therefore a useful tool towards the goal of imaging and optically manipulating neurons in neural circuits in 3D in a simultaneous fashion [101].

9 Future Work

This research created a live cell lithography platform capable of fabricating millimeter scale hydrogel scaffolds containing micron scale sub-structures of viable living cells. Patterns of C2C12 cells were shown to be viable over days and, with appropriate choice of hydrogel material, would begin the process of fusion and myotube formation. This work found that strategies must be employed to limit confinement of cells in hydrogel scaffolds such that cells can be supported by hydrogel, and feel the presence of hydrogel in 3D, but not limit the ability of the cells to differentiate. In order to provide the cells mobility, the next step is to consider MMP degradable hydrogels, which selectively degrade due to chemicals excreted by the entrapped cells. Two potential projects that could be explored after the problem of cell confinement is resolved are discussed in the sections to follow.

9.1 Hydrogel coatings for medical implants

Each year over 5 million Americans are implanted with medical devices ranging from hip replacements to pacemakers. While largely beneficial, implants continue to be plagued with problems of biocompatibility and biostability that can lead to implant failure and rejection. The body's natural response to a foreign object is an influx of inflammatory cells whose purpose is to isolate and eliminate the foreign object. If this cannot be accomplished and inflammation persists, the foreign object is encapsulated in fibrotic connective tissue [102]. This can lead to a range of problems for medical implants including insulating barriers around electrodes, scarring of heart valve sewing rings, and fibrous layers surrounding vascular grafts [103] that can result in complete loss of interaction between the implant and the surrounding tissue. The cost of rejected medical implants is extensive. Considering only four of the top 11 surgeries involving implanted medical devices, and taking the most conservative estimates of failure rates due to medical implant rejection, the annual cost is $1.87 billion [104].

This has led to significant research efforts aimed to improve the interface between host tissue and implanted medical devices. Most research is completed in animal models, making controlled repeatable studies with large sample sets challenging. Alternatively, the live cell lithography fabrication platform offers an improved methodology to study the effects of varying concentration of peptides and controlled duration of release of growth factors such that optimal biochemical cues can be defined to promote acceptance of medical implants. This will enable future researchers to more optimally incorporate growth factors and peptides into implant coatings without introducing unwanted adverse effects.

A variety of methods have been considered to improve biostability of medical implants. One approach is surface functionalization of implants with peptides such RGD. RGD is commonly used to promote cellular attachment and differentiation which, in the context of medical implants, leads to the formation of an extracellular matrix that is critical to acceptance of the implant. However, studies have found the effectiveness of surface functionalization varies depending on the material being functionalized. For example, RGD functionalized titanium entirely fails to promote cell adhesion [105].

Variability in effectiveness of surface functionalization led to interest in coating implants with thin hydrogel layers. The presence of a hydrogel layer has been shown to reduce background effects arising from non-specific protein adsorption. This is critical, as non-specific protein adsorption does not naturally occur in the normal wound healing process, and may be an instigator of the foreign body reaction which leads to rejection of medical implants. Further, hydrogel layers loaded with peptides have been shown in bone implants to enhance osteogenic cell adhesion, proliferation, and differentiation. [105]. Hydrogel coatings can also be designed to deliver a controlled release of one or more growth factors shown to enhance integration of the coated object into the surrounding tissue [106].

While preliminary results with hydrogels, growth factors, and peptides are promising for promoting implant acceptance, the critical task remains to determine the right combinations and concentration of peptides and growth factors, and the ideal duration of release of biochemical cues to most effectively promote growth without causing adverse side effects. This is a complex problem that varies depending on the type of the host tissue and the materials used in the implant.

In order to address this need, a controlled methodology must be developed to optimize hydrogel formulations for coatings of medical implants and to determine appropriate biochemical cues to incorporate into the implant when applicable. In order to contain the scope of the problem, one can start with the smaller problem of promoting cellular ingrowth in hydrogel coatings for repair of large scale bone defects, and/or in hydrogel based osteochondral implants.

Although a number of different methods are under study to repair large scale bone defects, to date most common procedures still rely on bone grafts [107]. Fresh bone grafts provide a source of osteoprogenitor cells, osteoinductive growth factors, and a structural scaffold for new bone formation. However, bone grafts results in loss of structure in donor area and can induce both local and systemic immune responses that can diminish or destroy the osteoinductive and conductive processes [108]. Thus, there is a need to improve medical implants for large scale bone defects such that they incorporates growth factors that mimic the biochemical cues that naturally occur in bone grafts.

Researchers have identified a range of growth factors that can be incorporated into bone implants to promote ingrowth [109]. Bone morphogenetic proteins (BMP), such as rhBMP-2 and rhBMP-7 (OP-1) are currently marketed for spinal fusion and long bone non-unions in tibiae, respectively [110]. While BMP growth factors are finding increased use, many studies have found the release rate and concentration are critical to avoiding unwanted side effects [111,112,113,114,115]. This has led researchers to consider degradable microspheres fabricated from PLGA, which can be designed to degrade at a consistent rate delivering growth factors over the span of a week to a month. This approach has been successfully used for regeneration of osteonecrotic bone [116]. However, current fabrication techniques for PLGA microspheres result in wide variability in the diameter of the microspheres, ranging from 4 to 400 µm within each batch [117]. The variability in diameter leads to a regionally highly variable duration of release which is less that optimal for promoting growth and can lead to side effects. To define optimal concentration of growth factors and peptides in hydrogel coatings, there is a need for a platform that can execute precisely controlled studies of cellular ingrowth as a function of growth factor type, growth factor infusion concentration, the duration of release, and the concentration of microspheres in the sample. This type of controlled study cannot be completed with any other currently available technology.

My solution is to use the live cell lithography fabrication platform to organize C2C12 cells, the position and distribution of PLGA microspheres infused with rhBMP-2, and the structure of the supporting hydrogel network. This solution brings a previously unattainable level of control to the study of hydrogel coatings, enabling precise repeatable studies of the influence of growth factors and peptides on cellular development and differentiation such that optimal coatings can be defined. Not only will this enable the ability to fabricate many samples with the same architecture such that studies of variability in cell development independent of changes in the structure of the scaffold can be completed. But this also allows for variables to be introduced by changing the number of microspheres encased in the hydrogel, the diameter of microspheres selected, and the distance of the microspheres from the cells.

The C2C12 cell line differentiates rapidly, and treatment of C2C12 cells with rhBMP-2 causes a shift in the differentiation pathway to osteoblastic. By allowing the ability to select the distribution and diameter of the rhBMP-2 infused PLGA microspheres patterned around the cells, one can control the concentration and duration of release of the growth factors, thus controlling differentiation, and sending biochemical cues to promote external cells to integrate into the scaffold.

PLGA microspheres infused with rhBMP-2 can be fabricated, and evaluated for growth factor release using previously established techniques [116]. Similar to processes presented in this thesis[12,13], cells and microspheres can be arranged using holographic optical tweezers, and solidified into a permanent structure of MMP degradable hydrogel using maskless projection photolithography.

Following patterning, samples can be thoroughly rinsed with phosphate buffer saline to remove residual liquid monomer, cells, and microspheres. The samples can be incubated in a solution of growth media and C2C12 cells suspended at a density of 1x10^5 cells/mL. Cellular ingrowth can be imaged and tracked every 1 to 2 days over the span of up to 10 days with brightfield microscopy. Additionally, samples can be fixed, stained with alizarin red, and imaged on the confocal microscope to test for production of alkaline phosphatase as an indicator of osteogenic differentiation. By quantitatively measuring alkaline phosphatase inside and outside the hydrogel coating as a function of the number and diameter of PLGA microspheres in the hydrogel it is possible to quantitatively define the ideal coating for promoting bone formation.

Consistent with research completed in this thesis, crosslinked polymers can be used as structural support for the evaluated coatings. In this application use of RGD modified MMP degradable hydrogel will be critical, as MMP degradability allows the hydrogel to selectively degrade in response to cellular ingrowth. This enables the coating to be readily permeable to the cells in the surrounding tissue.

By manipulating cellular concentrations, growth factor dose and duration of release, ideal conditions to promote cellular adhesion and differentiation will be identified. These cues will not only enhance cellular growth within the scaffold, but will also promote growth from the external environment into the scaffold as can be measured by confocal fluorescent imaging and tracking of cellular growth through brightfield microscopy. This future work could enable researchers to more optimally incorporate growth factors and peptides into implant coatings to promote integration of implants into the host tissue without adverse effects of overdosed growth factor release.

9.2 Living Neural Networks

An alternative future project could relate to patterning neurons in hydrogel to study neural circuit formation, enabling greater control in studies of the mechanisms of neural growth and communication. Using the live cell lithography platform 2D and 3D living neural networks

(LNNs) can be fabricated with precisely defined connectivity and structure. This will enable a range of research projects. For example, it is known that artificial LNNs are capable of sensing and transducing minute environmental perturbations. The ability to rapidly fabricate 2D and 3D neural networks has potential to improve diagnostics for drug and toxin screening, and chemical and biological sensing. Furthermore, LNNs can be used to study biocompatibility at the interface between a prosthetic device and human body. Similarly, research into the regeneration of nerve connections for spinal cord injuries could greatly benefit from a platform that would allow experiments to quickly determine what type of chemical or biological agents could stimulate the neural growth and re-establishing of neural connections.

In the last decade, many methods to fabricate LNNs have been investigated. 2D patterning of cells is commonly accomplished by lithographic deposition of polylysine is used to direct neuronal cell attachment and growth on planar electrode arrays [118,119,120]. Unfortunately, it has since been established that neurons constrained to a stiff 2D environment behave differently as compared to their *in vivo* environment [121]. As a result, a variety of methods to construct complex 3D tissue scaffolds are under study [122,123,124]. While these methods result in 3D structures that define scaffold shape, they provide no control over the internal distribution of cells within the scaffold. Such random-cell 3D printers are particularly inappropriate for neurobiology in which connectivity is of ultimate importance. Alternatively, the live cell lithography fabrication platform can be utilized to fabricate hydrogel structures precisely arranged living neurons, and true 3D structuring of cells.

The specific goals of this future project are two-fold. First, to demonstrate the feasibility of combining optical trapping with photopolymerization and multi-layer stereolithography to fabricate a 3D biocompatible living neural network for use in neuroscience and biomedical research, as well as in chemical and biological sensing applications. Second, demonstrate that the LNN fabrication platform can rapidly fabricate neural networks, and dynamically vary the placement of cells and the structure of the polymer scaffold supporting the neural network such that precise repeatable studies of neuronal growth and communication can be completed. In order to realize this goal, it is necessary to determine if the fabrication platform is capable of incorporating channels throughout the scaffold for guided neural growth. A known solution from the stereolithography research community incorporates a strong absorber to limit optical penetration and thus layer thickness approximately 20 µm. Absorbers, such as Tinuvin, have been used in recent tissue scaffold research [28] indicating possible biocompatibility. The largest difference between the proposed approach and traditional structural 3D printing is the low viscosity of the liquid monomers which, in this case, causes rapid out-diffusion of active oligomeric fragments. Over the course of repeated exposures, these can cause gelation in unexposed regions. If Tinuvin is found to be insufficient it is possible to fabricate MMP degradable multi-material structures, where one material is designed to degrade in a day, and the other is designed to degrade over the span of a year. Thus, then entire structure is initially polymerized, but elements of the structure rapidly dissipate enabling defined cellular outgrowth along the edges of the channels formed by materials that degrade slowly.

If this work were to be completed, viability studies completed in this thesis with C2C12 cells, would need to be repeated with neurons. It has been shown that neurons exposed to optical tweezers can retain viability [125]. To confirm this result, cells can be tweezed for varying amounts of times exposed to varying power per trap, and can be polymerized within

100 um voxels. A LIVE/DEAD assay can be used to quantify viability immediately after tweezing, and after multiple days. Alphanumeric patterned coverslips can be used to track cell exposure to the trapping source, and resulting viability.

Initial work would focus on the 2D problem, fabricating a simplistic 2D grid containing channels to direct neural outgrowth. Phase contrast imaging can be used to map neural growth. Furthermore, long term studies of interconnectivity of neural circuits can be probed non-invasively and in 3D using calcium imaging and photostimulation with the Pocketscope, as this eliminates the need for patch clamping or micro electro arrays within the scaffold to stimulate and record neural activity.

Following 2D patterning, a simplistic 3D grid of cells can be fabricated with channels to direct neural growth. Once the fabrication system has been optimized and verified for neurological research, the tool can be used to study neural circuit formation, and mechanisms for plasticity and repair. This can be accomplished by stimulating a firing pattern and measuring how the network responds as a function of the connectivity pattern that has been imposed.

This future research will bring live cell lithography to the neuroscience and broader tissue engineering community, and will provide scientific and clinical researchers with optical instruments of unprecedented flexibility and control. Within the neuroscience community this will provide a tool to understand neural circuit formation in a controlled 3D environment, resulting in a much needed intermediate level of complexity between cell cultures and living brains. Outside of neuroscience research this will allow greater control for basic biological studies of cellular communication and growth.

References Cited

---

[1] C. James, R. Davis, M. Meyer, A. Turner, S. Turner, G. Withers, L. Kam, G. Banker, H. Craighead, M. Isaacson, J. Turner, W. Shain "Aligned Microcontact Printing of Micrometer-Scale Poly-L-Lysine Structures for Controlled Growth of Cultured Neurons on Planar Microelectrode Arrays," *IEEE Transactions On Biomedical Engineering*, 47, 17-21 (2000).

[2] Sang Beom Jun, Matthew R. Hynd, Natalie Dowell-Mesfin, Karen L. Smith, James N. Turner, William Shain, Sung June Kim, "Low-Density Neuronal Networks Cultured using Patterned Poly-LLysine on Microelectrode Arrays," *J Neurosci Methods*, 160 317–326 (2007).

[3] D. Branch, B. Wheeler,G. Brewer, D. Leckband, "Long-Term Maintenance of Patterns of Hippocampal Pyramidal Cells on Substrates of Polyethylene Glycol and Microstamped Polylysine," *IEEE Transactions On Biomedical Engineering*, 47, 290-300, (2000)

[4] V.Tsang, S.Bhatia, "Three-dimensional tissue fabrication," *Advanced Drug Delivery Reviews*, 56, 1635– 1647 (2004).

[5] S. J. Hollister "Porous scaffold design for tissue engineering" *Nature Materials* 4, 518 - 524 (2005).

[6] V. Mironov, T. Boland, T. Trusk, G. Forgacs, R. R. Markwald "Organ printing: computer-aided jet-based 3D tissue engineering" *TRENDS in Biotechnology* 21(4) 157-161 (2003).

[7] P. Bajaj, B. Reddy Jr., L. Millet, C. Wei, P. Zorlutuna, Gang Bao, R. Bashir "Patterning the differentiation of C2C12 skeletal myoblasts" *Integr. Biol.* 3 897–909 (2011).

[8] S. L. Hume, S. M. Hoyt , J. S. Walker, B. V. Sridhar, J. F. Ashley, C. N. Bowman, S. J. Bryant "Alignment of multi-layered muscle cells within three-dimensional hydrogel Macrochannels" *Acta Biomaterialia* 8 2193–2202 (2012).

[9] V. Chan, J. H. Jeong, P. Bajaj, M. Collens, T. Saif, H. Kongb, R. Bashir "Multi-material bio-fabrication of hydrogel cantilevers and actuators with stereolithography" *Lab Chip* 12 88-98 (2012).

[10] H. Fujita, K. Shimizu, E. Nagamori "Novel Method for Measuring Active Tension Generation by C2C12 Myotube Using UV-Crosslinked Collagen Film" *Biotechnol. Bioeng.* 106 482–489 (2010).

[11] P. Zorlutuna , J. H. Jeong , H. Kong , R. Bashir "Stereolithography-Based Hydrogel Microenvironments to Examine Cellular Interactions" *Adv. Funct. Mater. 21* 3642–3651 (2011).

[12] A. Linnenberger, M. I. Bodine, C. Fiedler, J. J. Roberts, S. C. Skaalure, J. P. Quinn, S. J. Bryant, M. Cole, R. R. McLeod, "3D Live Cell Lithography" *Optics Express* 21(8) 10269-10277 (2013).

[13] A. Linnenberger, C. Fiedler, J. J. Roberts, S. C. Skaalure, S. J. Bryant, M. C. Cole, and R. R. McLeod, "Optical trapping for tissue scaffold fabrication." *SPIE NanoScience+ Engineering*. International Society for Optics and Photonics, 2013.

---

[14] Advisory Committee to the NIH Director, INTERIM REPORT Brain Research through Advancing Innovative Neurotechnologies (BRAIN) Working Group (2013).

[15] Alzheimer's Association "Alzheimer's Disease Facts and Figures" *Alzheimer's & Dementia,* 9 (2) 1-58 (2013).

[16] K. S. Cole "Dynamic electrical characteristics of the squid axon membrane" *Arch. Sci. Physiol.* 3, 253-258 (1949).

[17] A.L. Hodgkin, A.F. Huxley, B. Katz "Measurement of current-voltage relations in the membrane of the giant axon of Loligo" *J. Physiol., Lond.* 116, 424-448 (1952).

[18] S. A. Huettel, A. W. Song, G. McCarthy *Functional Magnetic Resonance Imaging* (2 ed.), Massachusetts: Sinauer (2009).

[19] L.A. Gunaydin, O. Yizhar, A. Berndt, V.S. Sohal, K. Deisseroth, P. Hegemann P. "Ultrafast optogenetic control" *Nat Neurosci.* 13(3) 387-92 (2010).

[20] V. Nikolenko, K. Poskanzer, R. Yuste "Two-photon photostimulation and imaging of neural circuits" *Nature Methods* 4 943 – 950 (2007).

[21] http://www.brimrose.com/pdfandwordfiles/aodefl.pdf

[22] http://www.physikinstrumente.com/en/products/prdetail.php?sortnr=200375

[23] V. Nikolenko, D. S Peterka R. Yuste "A portable laser photostimulation and imaging microscope" *J. Neural Eng.* 7(4) (2010)

[24] D. Preece, R. Bowman, A. Linnenberger, G. Gibson, S. Serati, M. Padgett "Increasing trap stiffness with position clamping in holographic optical tweezers," *Opt. Express* 17 22718-22725 (2009).

[25] A. Ashkin, J. M. Dziedzic, J. E. Bjorkholm, S. Chu, "Observation of a single-beam gradient force optical trap for dielectric particles," *Opt. Lett.* 11 288- 290 (1986).

[26] J. R. Moffitt, Y. R. Chemla, S. B. Smith, and C. Bustamante "Recent Advances in Optical Tweezers," *Annu. Rev. Biochem.* 77 205–28 (2008).

[27] K. Svoboda and S. M. Block, "Optical trapping," *Rev Sci Instrum*. 75(9) 2787–2809 (2004).

[28] http://arryx.com/bioryxFAQ.html#200traps

[29] A. Ashkin, "Forces of a single-beam gradient laser trap on a dielectric sphere in the ray optics regime," *Biophys. J.* 61 569-582 (1992).

[30] A. Rohrbach and E. H. K. Stelzer, "Trapping Forces, Force Constants, and Potential Depths for Dielectric Spheres in the Presence of Spherical Aberrations," *Appl. Opt.* 41 2494-2507 (2002).

[31] K. Svoboda and S. M. Block, "Optical trapping of metallic Rayleigh particles," *Opt. Lett.* 19 930-932 (1994).

---

[32] Y. Seol, A. E. Carpenter, and T. T. Perkins, "Gold nanoparticles: enhanced optical trapping and sensitivity coupled with significant heating," *Opt. Lett.* 31 2429-2431 (2006).

[33] J. Plewa, E. Tanner, D. Mueth, and D. Grier, "Processing carbon nanotubes with holographic optical tweezers," *Opt. Express* 12 1978-1981 (2004).

[34] P. Prentice, A. Cuschieri, K. Dholakia, M. Prausnitz and P. Campbell, "Membrane disruption by optically controlled microbubble cavitation", *Nature Physics* 1 107 - 110 (2005).

[35] M. Guillon, K. Dholakia, and D. McGloin, "Optical trapping and spectral analysis of aerosols with a supercontiuum laser source," *Opt. Express* 16 7655-7664 (2008).

[36] G. Sinclair, P. Jordan, J. Leach, M. J. Padgett, J. Cooper, J. "Defining the limits of holographic optical tweezers," *Mod.Opt*., 51 409–414 (2004).

[37] G. M. Gibson, R. W. Bowman, A. Linnenberger, M. Dienerowitz, D. B. Phillips, D. M. Carberry, M. J. Miles, and M. J. Padgett "A compact holographic optical tweezers instrument," *Rev. Sci. Instrum.* 83 113107-113107 (2012).

[38] J. Liesener, M. Reicherter, T. Haist, and H. J. Tiziani "Multi-functional optical tweezers using computer-generated holograms," *Opt. Commun.* 185(1) 77-82 (2000).

[39] G. Sinclair, J. Leach, P. Jordan, G. Gibson, E. Yao, Z. Laczik, M. Padgett, and J. Courtial "Interactive application in holographic optical tweezers of a multi-plane Gerchberg-Saxton algorithm for three-dimensional light shaping," *Opt. Express* 12 1665-1670 (2004).

[40] K. Castelino, S. Satyanarayana, M. Sitti, "Manufacturing of Two and Three-Dimensional Micro/Nanostructures by Integrating Optical Tweezers with Chemical Assembly", *Nanotechnology*, 1 59-56 (2003).

[41] L. Ikin, J. Grieve, D. Carberry, G. Gibson, M Padgett, M. Miles, "Assembly of 3D structures using holographic optical trapping", *Presented SPIE*, (2008).

[42] Ritesh Agarwal, Kosta Ladavac, Yael Roichman, Guihua Yu, Charles Lieber, and David Grier, "Manipulation and assembly of nanowires with holographic optical traps," *Opt. Express* 13, 8906-8912 (2005).

[43] U. Mirsaidov, J. Scrimgeour, W. Timp, K. Beck, M. Mir, P. Matsudaira, G. Timp. "Live cell lithography: using optical tweezers to create synthetic tissue." *Lab Chip* 8 (12) 2174-2181 (2008).

[44] C. Sun, N. Fang, D. M. Wu, and X. Zhang "Projection micro-stereolithography using digital micro-mirror dynamic mask," *Sensor Actuat. A-Phys* 121 113-120 (2005).

[45] T. Billiet, M. Vandenhaute, J. Schelfhout, S. V. Vlierberghe, P. Dubruel "A review of trends and limitations in hydrogel-rapid prototyping for tissue engineering," *Biomaterials* 33 6020-6041 (2012).

[46] R. Gauvin, Y. C. Chen, J.W. Lee, P. Soman, P. Zorlutuna, J. W. Nichol, H. Bae, S. Chen, and A. Khademhosseini "Microfabrication of complex porous tissue engineering scaffolds using 3D projection stereolithography," *Biomaterials* 33(15) 3824–3834 (2012).

---

[47] J. A. Burdick, K.S. Anseth “Photoencapsulation of osteoblasts in injectable RGD-modified PEG hydrogels for bone tissue engineering,” *Biomaterials* 23(22) 4315–4323 (2002).

[48] S. J. Bryant, K.S. Anseth “Controlling the spatial distribution of ECM components in degradable PEG hydrogels for tissue engineering cartilage” Journal of Biomedical Materials Research Part A 64(1) 70-79 (2003).

[49] S.J. Bryant, R.J. Bender, K.L. Durand, K.S. Anseth "Encapsulating chondrocytes in degrading PEG hydrogels with high modulus: engineering gel structural changes to facilitate cartilaginous tissue production." *Biotechnology and bioengineering* 86(7) 747-755 (2004).

[50] A. S. Sawhney, C. P. Pathak, and J. A. Hubbell. "Bioerodible hydrogels based on photopolymerized poly (ethylene glycol)-co-poly (. alpha.-hydroxy acid) diacrylate macromers," *Macromolecules* 26(4) 581-587 (1993).

[51] B. D. Fairbanks, M. P. Schwartz, C. N. Bowman, K. S. Anseth “Photoinitiated polymerization of PEGdiacrylate with lithium phenyl-2,4,6-trimethylbenzoylphosphinate: Polymerization rate and cytocompatibility,” *Biomaterials* 30 6702–6707 (2009).

[52] S. J. Bryant, C. R. Nuttelman, and K. S. Anseth "Cytocompatibility of UV and visible light photoinitiating systems on cultured NIH/3T3 fibroblasts in vitro," *J. Biomat. Sci.-Polym. E*. 11 439-457 (2000).

[53] C. G. Williams, A. N. Malik, T. K. Kim, P. N. Manson, and J. H. Elisseeff "Variable cytocompatibility of six cell lines with photoinitiators used for polymerizing hydrogels and cell encapsulation," *Biomaterials* 26 1211-1218 (2005).

[54] N. E. Fedorovich, M. H. Oudshoorn, D. van Geemen, W. E. Hennink, J. Alblas, and W. J. A. Dhert "The effect of photopolymerization on stem cells embedded in hydrogels," *Biomaterials* 30 344-353 (2009).

[55] A. C. Urness, M. C. Cole, K. K. Kamysiak, E. R. Moore, and R. R. McLeod “Liquid deposition photolithography for submicrometer resolution three-dimensional index structuring with large throughput,” *Light Sci. Appl.* 2(3) (2013).

[56] H. Liang, K. T. Vu, P. Krishnan, T. C. Trang, D. Shin, S. Kimel, and M. W. Berns "Wavelength dependence of cell cloning efficiency after optical trapping," *Biophysical journal* 70 1529-1533 (1996).

[57] April 10, 2013, email with Prof. Bryant

[58] E. Eriksson, J. Scrimgeour, A. Graneli, K. Ramser, R. Wellander, J. Enger, D. Hanstorp, and M. Goksör "Optical manipulation and microfluidics for studies of single cell dynamics," *J. Opt. A: Pure Appl. Opt.* 9(8) (2007).

[59] H. Liang, K. T. Vu, P. Krishnan, T. C. Trang, D. Shin, S. Kimel, and M. W. Berns "Wavelength dependence of cell cloning efficiency after optical trapping," *Biophysical journal* 70 1529-1533 (1996).

---

[60] B. K. Mann, A.S. Gobin, A.T. Tsai, R.H. Schmedlen, J.L West. “Smooth muscle growth in photopolymerized hydrogels with cell adhesive and proteolytically degradable domains: synthetic ECM analogs for tissue engineering” *Biomaterials* 22 (2001) 3045–51.

[61] J. J. Roberts, S. J. Bryant “Comparison of photopolymerizable thiol-ene PEG and acrylate-based PEG hydrogels for cartilage development,” *Biomaterials* 34(38) 9969–9979 (2013).

[62] C. Lin, A. Raza, H. Shih “PEG hydrogels formed by thiol-ene photo-click chemistry and their effect on the formation and recovery of insulin-secreting cell spheroids,” *Biomaterials* 32(36) 9685-9695 (2011).

[63] M. P. Schwartz, B. D. Fairbanks, R. E. Rogers, R. Rangarajan , M. H. Zaman, K. S. Anseth “A synthetic strategy for mimicking the extracellular matrix provides new insight about tumor cell migration,” *Integr. Biol.* 2 32–40 (2010).

[64] J. A. Benton, B. D. Fairbanks, K. S, Anseth “Characterization of valvular interstitial cell function in three dimensional matrix metalloproteinase degradable PEG hydrogels,” *Biomaterials* 30 6593– 6603 (2009).

[65] A. A. Aimetti, A. J. Machen, K. S. Anseth “Poly(ethylene glycol) hydrogels formed by thiol-ene photopolymerization for enzyme-responsive protein delivery,” *Biomaterials* 30 6048–6054 (2009).

[66] S. B. Anderson, C.C. Lin, D.V. Kuntzler, K. S, Anseth “The performance of human mesenchymal stem cells encapsulated in cell-degradable polymer-peptide hydrogels,” *Biomaterials* 32 3564– 3574(2011).

[67] A. Terella, P. Mariner, N. Brown, K. S. Anseth, S. O. Streubel “Repair of a calvarial defect with biofactor and stem cell-embedded polyethylene glycol scaffold,” *Arch. Facial Plast. Surg*. 12 166–171 (2010).

[68] B. D. Fairbanks, M. P. Schwartz, A. E. Halevi, C.R. Nuttelman, C. N. Bowman, K.S. Anseth “A versatile synthetic extracellular matrix mimic via thiol-norbornene photopolymerization,” *Adv. Mater.* 21 5005–5010 (2009).

[69] P. Soman, J. A. Kelber, J. W. Lee, T. N. Wright, K. S. Vecchio, R. L. Klemke, and S. Chen. "Cancer cell migration within 3D layer-by-layer microfabricated photocrosslinked PEG scaffolds with tunable stiffness." *Biomaterials* 33(29) 7064–7070 (2012).

[70] W. Denk, J.H. Strickler, W.W. Webb “Two-photon laser scanning fluorescence microscopy”, *Science* 248 73-76 (1990).

[71] C. Soeller, M.B. Cannell, “Two-photon microscopy: Imaging in scattering samples and three-dimensionally resolved flash photolysis” *Microscopy Research and Technique* 47 182-195 (1999).

[72] M.P. Lutolf, G.P. Raeber, A.H. Zisch, N. Tirelli, J.A. Hubbell JA “Cell-responsive synthetic hydrogels” *Adv Mat.* 15 888–92 (2003).

---

[73] Y. Park, M.P. Lutolf, J.A. Hubbell, E.B. Hunziker, M. Wong "Bovine primary chondrocyte culture in synthetic matrix metalloproteinase-sensitive poly(ethylene glycol)-based hydrogels as a scaffold for cartilage repair" *Tissue Eng.* 10 515–22 (2004).

[74] J. A. Benton, B.D. Fairbanks, K.S. Anseth "Characterization of valvular interstitial cell function in three dimensional matrix metalloproteinase degradable PEG hydrogels" Biomaterials 30 6593– 603 2009.

[75] A.A. Aimetti, A.J. Machen, K.S. Anseth "Poly(ethylene glycol) hydrogels formed by thiol-ene photopolymerization for enzyme-responsive protein delivery" *Biomaterials* 30 6048–6054 (2009).

[76] J. Patterson, J.A. Hubbell "Enhanced proteolytic degradation of molecuarly engineered peg hydrogels in response to mmp-1 and mmp-2" *Biomaterials* 31(30) 7836-7845 (2010).

[77] D. Oron, E. Papagiakoumou, F. Anselmi, V. Emiliani "Two Photon Optogenetics" *Progress in Brain Research* 196 119-143 (2012).

[78] A.M. Packer, D.S. Peterka, J.J. Hirtz, R. Prakash, K. Deisseroth, R. Yuste "Two-photon optogenetics of dendritic spines and neural circuits" *Nat Methods.* 9(12)1202-5 (2012).

[79] Tønnesen J, Sørensen AT, Deisseroth K, Lundberg C, Kokaia M. "Optogenetic control of epileptiform activity" *PNAS* 106(29) 12162-7 (2009).

[80] K.M. Tye, J.J. Mirzabekov, M.R. Warden, E.A. Ferenczi, H.C. Tsai, J. Finkelstein, S.Y. Kim, A. Adhikari, K.R. Thompson, A.S. Andalman, L.A. Gunaydin, I.B. Witten, K. Deisseroth "Dopamine neurons modulate neural encoding and expression of depression-related behavior" *Nature 493*(7433) 537-541 (2012).

[81] M.T. Stefanik, K. Moussawi, Y.M. Kupchik, K.C. Smith, R.L. Miller, M.L. Huff, K. Deisseroth, P.W. Kalivas, R.T. Lalumiere "Optogenetic inhibition of cocaine seeking in rats" *Addict Biol. 18*(1) 50-53 2012.

[82] A.V. Kravitz, B.S. Freeze, P.R. Parker, K. Kay, M.T. Thwin, K. Deisseroth, A.C. Kreitzer "Regulation of parkinsonian motor behaviours by optogenetic control of basal ganglia circuitry" *Nature* 466(7306) 622-6 (2010).

[83] http://www.stanford.edu/group/dlab/optogenetics/index.html

[84] K. Zalocusky, K. Deisseroth "Optogenetics in the behaving rat: integration of diverse new technologies in a vital animal model" *Optogenetics* 1 1-17 (2013).

[85] D. R. Sparta, A. M Stamatakis, J. L Phillips, N. Hovels, R. V. Zessen, G. D Stuber "Construction of implantable optical fibers for long-term optogenetic manipulation of neural circuits" *Nat. Protoc.* 7(1) 12-23 (2011).

[86] G. Silasi, J. D. Boyd, J.LeDue, T. H. Murphy "Improved methods for chronic light-based motor mapping in mice: automated movement tracking with accelerometers, and chronic EEG recording in a bilateral thin-skull preparation" *Front Neural Circuits*. 7(123) 1-10 (2013).

[87] http://www.ti.com/tool/dlpd4x00kit

---

[88] http://bnonlinear.com/products/xyslm/XYSeriesDS0909.pdf#page=9

[89] E.S. Boyden, F. Zhang, E. Bamberg, G. Nagel, K. Deisseroth. "Millisecond-timescale, genetically targeted optical control of neural activity." *Nature neuroscience* 8(9) 1263-1268 (2005).

[90] E. R. Dowski Jr., and W. T. Cathey, “Extended depth of field through wave-front coding,” Appl. Opt. 34(11), 1859 (1995).

[91] S. Quirin, D. S. Peterka, and R. Yuste "Instantaneous three-dimensional sensing using spatial light modulator illumination with extended depth of field imaging." Optics Express 21(13) 16007 (2013).

[92] T. Lindeberg, M.X. Li “Segmentation and Classification of Edges Using Minimum Description Length Approximation and Complementary Junction Cues” *Computer Vision and Image Understanding,* 67(1) 88-98 (1997).

[93] R. Di Leonardo, F. Ianni, and G. Ruocco “Computer generation of optimal holograms for optical trap arrays,” *Optics Express*, 15(4) 1913-1922 (2007).

[94] https://github.com/MartinPersson/HOTlab

[95] L. Mao, J.Q. Wang “Group I metabotropic glutamate receptormediated calcium signalling and immediate early gene expression in cultured rat striatal neurons. *Eur J Neurosci* 17 741–750 (2003).

[96] J.N. Kerr, D. Greenberg, F. Helmchen “Imaging input and output of neocortical networks in vivo.” *Proc Natl Acad Sci* 102 14063–14068 (2005).

[97] E. Yaksi, R.W. Friedrich “ Reconstruction of firing rate changes across neuronal populations by temporally deconvolved Ca2+ imaging.” *Nat Methods* 3 344–346 (2006)

[98] T.F. Holekamp, D. Turaga, T.E. Holy “ Fast three-dimensional fluorescence imaging of activity in neural populations by objectivecoupled planar illumination microscopy.” *Neuron* 57 661–672 (2008).

[99] J.T. Vogelstein, A. Packer, T.M. Machado, T. Sippy, B. Babadi, R. Yuste, L. Paninski “Fast non-negative deconvolution for spike train inference from population calcium imaging.” *J Neurophysiol* 104 3691–3704 (2010).

[100] R. Yuste, J. MacLean, J. Vogelstein, and L. Paninski. "Imaging action potentials with calcium indicators." *Cold Spring Harbor Protocols* 8 985-989 (2011).

[101] A.P. Alivisatos, M. Chun, G.M. Church, R.J. Greenspan, M.L. Roukes, and R.Yuste. "The brain activity map project and the challenge of functional connectomics." Neuron 74(6) 970 (2012).

[102] J. M. Anderson, A. Rodriguez, D.T. Chang. “Foreign body reaction to biomaterials” *Seminars in Immunology* 20 (2008) 86–100.

[103] B.D. Ratner, S. J. Bryant “BIOMATERIALS:Where We Have Been and Where We Are Going” *Annu. Rev. Biomed. Eng.* 6 41–75 (2004).

---

[104] http://247wallst.com/healthcare-economy/2011/07/18/the-eleven-most-implanted-medical-devices-in-america/2/

[105] A.J. García, C.D. Reyes. “Bio-adhesive Surfaces to Promote Osteoblast Differentiation and Bone Formation” *J. of Dental Research* 84(5) (2005) 407-413.

[106] C.A. Simmons, E. Alsberg, S. Hsiong,W.J. Kim, D. J. Mooney. “Dual growth factor delivery and controlled scaffold degradation enhance in vivo bone formation by transplanted bone marrow stromal cells” *Bone* 35 (2004) 562– 569.

[107] V.M. Goldberg, S. Stevenson. “The biology of bone grafts” *Semin. Arthroplasty* 4(2) 1993 58-63.

[108] R. R. Betz “Limitations of autograft and allograft: New synthetic solutions” *Orthopedics* 25 (2002) s561-70.

[109] V. Luginbuehl, L.Meinel, H. P. Merkle, B. Gander. “Localized delivery of growth factors for bone repair European Journal of Pharmaceutics and Biopharmaceutics” *J. of Periodontology* 58 (2004) 197–208.

[110] P.C. Bessa, M. Casal, R.L. Reis. “Bone morphogenetic proteins in tissue engineering: the road from the laboratory to the clinic, part I (basic concepts)” *J. Tissue Eng. Regen. Med.* 2 (1) (2008) 1–13.

[111] K. Shahlaie, K.D. Kim. “Occipitocervical fusion using recombinant human bone morphogenetic protein-2: adverse effects due to tissue swelling and seroma” *Spine* 33 (21) (2008) 2361–2366.

[112] D. Benglis, M.Y. Wang, A.D. Levi. “A comprehensive review of the safety profile of bone morphogenetic protein in spine surgery” *Neurosurgery* 62 (5 Suppl 2) (2008) ONS423–ONS431.

[113] M. Boakye, P. Mummaneni, V.M. Garrett, G. Rodts, R. Haid. “Anterior cervical discectomy and fusion involving a polyetheretherketone spacer and bone morphogenetic protein” *J. Neurosurg. Spine* 2(5) (2005) 521–525.

[114] R.S. Brower, N.M. Vickroy. “A case of psoas ossification from the use of BMP-2 for posterolateral fusion at L4-L5” *Spine* 33(18) (2008) E653–E655.

[115] L.M. Tumialan, J. Pan, G.E. Rodts, P.V. Mummaneni. “The safety and efficacy of anterior cervical discectomy and fusion with polyetheretherketone spacer and recombinant human bone morphogenetic protein-2: a review of 200 patients” *J. Neurosurg. Spine* 8(6) (2008) 529–535.

[116] C.K. Wang, M.L. Ho, G.J. Wang, J.K. Chang, C.H. Chen, Y.C. Fu, H. H Fu. “Controlled-release of rhBMP-2 carriers in the regeneration of osteonecrotic bone” *Biomaterials* 30 (2009) 4178–4186.

---

[117] A. Lochmann, H. Nitzsche, S. Einem, E. Schwarz, K. Mäder. “The influence of covalently linked and free polyethylene glycol on the structural and release properties of rhBMP-2 loaded microspheres” *Journal of Controlled Release* 147 (2010) 92–100.

[118] C. James, R. Davis, M. Meyer, A. Turner, S. Turner, G. Withers, L. Kam, G. Banker, H. Craighead, M. Isaacson, J. Turner, W. Shain “Aligned Microcontact Printing of Micrometer-Scale Poly-L-Lysine Structures for Controlled Growth of Cultured Neurons on Planar Microelectrode Arrays,” *IEEE Transactions On Biomedical Engineering* 47 17-21 (2000).

[119] Sang Beom Jun, Matthew R. Hynd, Natalie Dowell-Mesfin, Karen L. Smith, James N. Turner, William Shain, Sung June Kim, “Low-Density Neuronal Networks Cultured using Patterned Poly-LLysine on Microelectrode Arrays,” *J Neurosci Methods* 160 317–326 (2007).

[120] D. Branch, B. Wheeler,G. Brewer, D. Leckband, “Long-Term Maintenance of Patterns of Hippocampal Pyramidal Cells on Substrates of Polyethylene Glycol and Microstamped Polylysine,” *IEEE Transactions On Biomedical Engineering* 47 290-300, (2000)

[121] J. Wang, L. Ren, L. Li, W. Liu, J. Zhou, W. Yu, D. Tong, and S. Chen. "Microfluidics: A new cosset for neurobiology." *Lab Chip* 9(5) 644-652 (2008).

[122] V.Tsang, S.Bhatia, “Three-dimensional tissue fabrication,” *Advanced Drug Delivery Reviews*, 56, 1635– 1647 (2004).

[123] T. Xu, C. A. Gregory, P. Molnar, X. Cui, S. Jalota, S. B. Bhaduri, and T. Boland. "Viability and electrophysiology of neural cell structures generated by the inkjet printing method." *Biomaterials* 27(19) 3580-3588 (2006).

[124] M. Nakamura, S. Iwanaga, C. Henmi, K. Arai, and Y. Nishiyama. "Biomatrices and biomaterials for future developments of bioprinting and biofabrication." *Biofabrication* 2 014110 (2010).

[125] E. Townes-Anderson, R. S. St Jules, D. M. Sherry, J. Lichtenberger, and M. Hassanain. "Micromanipulation of retinal neurons by optical tweezers." *Mol. Vis* 4(12) 1998.